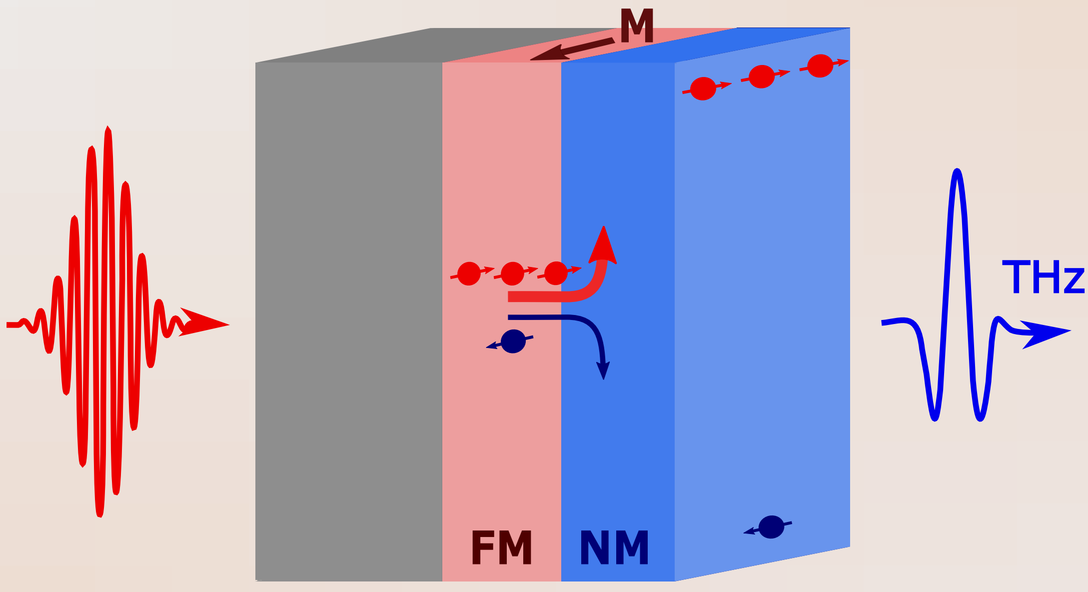

Investigation of spin current generated THz transients in materials with high spin-orbit coupling

Sarah Heidtfeld

Schlüsseltechnologien / Key Technologies
Band / Volume 304
ISBN 978-3-95806-893-3

Mitglied der Helmholtz-Gemeinschaft

JÜLICH
Forschungszentrum

Schriften des Forschungszentrums Jülich
Reihe Schlüsseltechnologien / Key Technologies Band / Volume 304

Forschungszentrum Jülich GmbH
Peter Grünberg Institut (PGI)
Elektronische Eigenschaften (PGI-6)

Investigation of spin current generated THz transients in materials with high spin-orbit coupling

Sarah Heidtfeld

Schriften des Forschungszentrums Jülich
Reihe Schlüsseltechnologien / Key Technologies Band / Volume 304

ISSN 1866-1807 ISBN 978-3-95806-893-3

Bibliografische Information der Deutschen Nationalbibliothek.
Die Deutsche Nationalbibliothek verzeichnet diese Publikation in der Deutschen Nationalbibliografie; detaillierte Bibliografische Daten sind im Internet über http://dnb.d-nb.de abrufbar.

Herausgeber und Vertrieb:	Forschungszentrum Jülich GmbH Zentralbibliothek, Verlag 52425 Jülich Tel.: +49 2461 61-5368 Fax: +49 2461 61-6103 zb-publikation@fz-juelich.de www.fz-juelich.de/zb
Umschlaggestaltung:	Grafische Medien, Forschungszentrum Jülich GmbH
Druck:	Grafische Medien, Forschungszentrum Jülich GmbH

Schriften des Forschungszentrums Jülich
Reihe Schlüsseltechnologien / Key Technologies, Band / Volume 304

D 464 (Diss. Duisburg-Essen, Univ., 2025)

ISSN 1866-1807
ISBN 978-3-95806-893-3

Vollständig frei verfügbar über das Publikationsportal des Forschungszentrums Jülich (JuSER) unter www.fz-juelich.de/zb/openaccess.

Zusammenfassung

Spinbasierte Phänomene bilden das zentrale Konzept im Bereich der Spintronik, wo effiziente Spinstromerzeugung, Spin-Ladungsstrom-Umwandlung sowie Spintransport die Schlüsselkonzepte für die Entwicklung elektronischer Geräte der nächsten Generation darstellen. Mit der umfassenden Verfügbarkeit von Femtosekundenlasern eröffnete sich ein neues Forschungsfeld der ultraschnellen Spintronik, das darauf abzielt, den Spintransport auf ultrakurzen Zeitskalen zu verstehen. Eine Möglichkeit, transiente Pikosekunden-Spinstrompulse zu erzeugen, ist die Beleuchtung von Ferromagnet (FM)/Schwermetall (HM) Heterostrukturen durch Femtosekunden-Laserpulse. Über den inversen Spin-Hall-Effekt (ISHE) werden diese transienten Spinströme in transiente Ladungsströme umgewandelt, die mittels Terahertz (THz)-Strahlung detektierbar sind.

In dieser Arbeit haben wir den Nachweis von THz-Strahlung als nicht-invasives Mittel zur Untersuchung der Spinstromerzeugung in einer Vielzahl von dünnen Schichten und Heterostrukturen eingesetzt. Frühere Arbeiten zeigten, dass die Spin-Bahn-Kopplung (SOC) eine entscheidende Rolle für die Effizienz der Spin-Ladungsstrom-Umwandlung spielt und wir haben für unsere Studie Materialien mit hoher SOC gewählt.

Zunächst untersuchten wir $Ni_{80}Fe_{20}$/HM-Heterostrukturen, wobei das HM-Material entweder Pt oder Pd war. Im zweiten Teil haben wir eine Heusler-Legierung $Co_2Fe_{0.4}Mn_{0.6}Si$ (CFMS) untersucht, die mit Pt, Ta, Al oder Cr beschichtet war. Wir konnten den inversen Spin-Hall-Effekt als dominanten Mechanismus der THz-Erzeugung in diesen Heterostrukturen identifizieren und bestätigten die Rolle der Spin-Bahn-Kopplung als Schlüsselfaktor für die Effizienz der Spin-Ladungsstrom-Umwandlung. Darüber hinaus untersuchten wir die Abhängigkeit vom Magnetisierungszustand und stellten fest, dass die THz-Amplitude der Magnetisierung der Probe folgt. Zusätzlich beobachteten wir, dass die Oxidation der HM-Schicht die Effizienz der Spin-Ladungsstrom-Umwandlung verringern kann, während eine Diffusion an der Grenzfläche von CFMS/Al vorteilhaft ist.

In einer separaten Studie an keilförmigen topologischen Isolator Bi_2Se_3 Proben zeigte die dickeabhängige THz-Untersuchung eine starke Variation der THz-Amplitude mit der Schichtdicke. Wir führen diese Variation auf Änderungen der strukturellen Eigenschaften des Bi_2Se_3 zurück. Zudem konnten wir einen starken Anstieg der transienten THz-Amplitude in Bi_2Se_3, beschichtet mit 3 nm Al feststellen, was darauf hindeutet,

dass die Entstehung an der Oberfläche von Bi_2Se_3 stattfindet. Unsere Studie trägt zum Verständnis der THz-Erzeugung in Heusler-Legierungen und topologischen Isolatoren bei.

Abstract

Spin-based phenomena are the central concept in the field of spintronics, where efficient spin current generation, spin-to-charge conversion, and spin transport are the key concepts for the development of next-generation electronic devices. With the extensive availability of femtosecond lasers a new research field of ultrafast spintronics has opened up, aiming to understand spin-transport on the ultrafast time scales. One way to generate picosecond transient spin current pulses is the illumination of ferromagnet (FM)/heavy metal (HM) heterostructures by femtosecond laser pulses. Via the inverse spin-Hall effect (ISHE), these transient spin currents are converted into transient charge currents, detectable via Terahertz (THz) radiation.

In this thesis, we employed the detection of THz radiation as a non-invasive means to investigate spin-current generation in a variety of thin films and hetero-structures. It was shown earlier that the spin-orbit coupling plays a decisive role in spin-to-charge conversion efficiency and we have chosen materials with high SOC in our study.

We first studied $Ni_{80}Fe_{20}$/HM hetero-structures, where the HM material was either Pt or Pd. In the second part we have investigated a Heusler alloy $Co_2Fe_{0.4}Mn_{0.6}Si$ (CFMS), capped with a thin film of either Pt, Ta, Al or Cr. We have found the inverse spin-Hall effect to be the dominating mechanism of THz generation in these hetero-structures and confirmed the role of spin-orbit coupling as a key factor for spin-to-charge conversion efficiency. Moreover we have investigated the dependency on magnetization and found that the amplitude of THz follows the sample's magnetization. Additionally, we have found that the oxidation of the HM layer can reduce spin-to-charge conversion efficiency, whereas interdiffusion at the interface of CFMS/Al was found to be beneficial.

In a seperate study on wedged topological insulator Bi_2Se_3 samples the thickness dependent THz-investigation revealed a strong variation of THz amplitude with the Bi_2Se_3 thickness. We ascribe these variations to a change in structural properties of the Bi_2Se_3. We have found a strong increase in the THz transient amplitude in Bi_2Se_3 capped with 3 nm of Al indicating that the generation mechanism is occurring at the surface of Bi_2Se_3.

Our study contributes to the understanding of THz generation in Heusler alloys and topological insulators.

Contents

1 Introduction **1**

1.1 Spintronics at the ultrafast scale 1

1.2 This thesis 3

2 Theoretical background **5**

2.1 Ferromagnetism in 3d-transition metals 5

2.1.1 Spin-orbit coupling 7

2.2 Spin currents 9

2.3 Generation of spin currents 11

2.3.1 Spin pumping 11

2.3.2 Optical excitation with fs-laser pulses 12

2.4 Spin-to-charge conversion 15

2.4.1 History of Hall effects 15

2.4.2 Spin-Hall effect: phenomenology 17

2.4.3 Intrinisic contribution - anomalous velocity 18

2.4.4 Extrinsic contributions 19

2.5 Spin-to-charge conversion in 2D 21

2.5.1 Semiconductor interfaces 21

2.5.2 Rashba-Edelstein effect 23

3 Experimental **25**

3.1 Optical THz emission setup 25

3.2 Detection of terahertz radiation 26

3.3 Ferromagnetic resonance 27

3.4 MPMS-SQUID 29

4 THz generation in metallic heterostructures **31**

5 THz generation in Heusler alloy/heavy metal bilayers **35**

5.1 Heusler alloy $Co_2Fe_{0.4}Mn_{0.6}Si$ 35

5.2 THz transients from $Co_2Fe_{0.4}Mn_{0.6}Si$/NM bilayers 37

5.2.1 Magnetic field dependence 40

5.2.2 Temperature dependence 42
5.3 Ferromagnetic resonance 43
5.4 Discussion 46

6 THz generation in topological insulator Bi_2Se_3 49
6.1 Introduction to topological insulators 49
6.1.1 Topological concepts and the quantum Hall state 49
6.1.2 Quantum spin Hall state and $_2$ invariant 51
6.1.3 3D topological insulator Bi_2Se_3 53
6.2 Sample set 55
6.3 Thickness dependent THz emission in Bi_2Se_3 58
6.3.1 Excitation with circularly polarized light (<35 nm) 62
6.3.2 Circularly polarized excitation (>20 nm) 64
6.3.3 Azimuthal angle dependence 66
6.3.4 THz component E_y & out-of-plane contributions 68
6.4 Discussion 71

7 Conclusion and outlook 81

Appendices 85

A THz Generation in Heusler alloy/heavy metal bilayers 87
A.1 Ferromagnetic resonance in CFMS/NM bilayers 87
A.2 XRR of CFMS/NM bilayers 89

B THz generation in topological insulator Bi_2Se_3 91
B.1 Thickness dependent THz transients Bi_2Se_3 91
B.2 Circularly polarized excitation Bi_2Se_3 93
B.3 Grain size of Bi_2Se_3 from AFM measurements 94
B.4 Refractive index and extinction coefficient in Bi_2Se_3 94
B.5 Temperature rise under fs-excitation in Bi_2Se_3 95

Bibliography 97

Publications and conference contributions i

Acknowledgements iii

Curriculum vitae v

Chapter 1

Introduction

1.1 Spintronics at the ultrafast scale

Conventional electronic devices, in which the electron charge is used to transport and store information, have been a cornerstone of modern technology. However, as these devices have become smaller and more complex, they have faced numerous challenges, such as increased power consumption, and reached their limits in terms of heat dissipation, processing speeds, and scalability [1, 2]. This has led to an increased interest in another intrinsic electron property, which has been neglected in applied electronics for a long time: the electron spin. With the discovery of giant magnetoresistance (GMR) in 1988 by Peter Grünberg and Albert Fert, a new research field of spin-based electronics (spintronics) emerged, seeking to exploit the electron spin for a new type of electronic devices [3, 4]. Spintronics has the potential to overcome many of the limitations of conventional electronics and to meet the ever-growing demand for increased processing speeds and data storage [5]. One of the most significant breakthroughs in the field of spintronics was the invention of magnetic random access memory (MRAM), which utilizes the magnetic orientation of electron spins to store data and has the advantage of preserving the data even without any power applied [6]. The key requirement for spintronic devices is to efficiently manipulate the electronic spin state and the ability to transport and read out spin information. The spin transport, the transfer of angular momentum, can occur in two ways: spin-polarized currents and spin waves. While spin waves involve propagation of collective spin excitations and, therefore, eliminate heat dissipation due to Ohmic losses, spin currents describe the flow of electrons with a preferential spin orientation [7]. There are two crucial parameters to determine the spin transport efficiency in spintronic devices: spin polarization and spin diffusion length. The spin polarization refers to the degree to which the electron spins are aligned in a material, and the spin diffusion length describes the length scale over which the spin information is maintained [2]. The MRAM technology is based on the functionality of spin valve structures using spin-transfer-torques (STT), which allow the switching of magnetic layers via spin injection using spin-polarized currents. Since 2016, devices including STT-MRAM by Everspin, have been available on the market [8]. However, at the same time, the switching via spin-orbit-torques (SOT) was proposed to be a promising route to faster switching at lower current densities [9, 10]. Efficient generation and detection of spin-polarized currents led to investigations of the conversion effects between charge and spin currents such as the spin Hall effect (SHE) or the Rashba-Edelstein effect (REE) [11, 12, 13, 14]. In addition to advancing our understanding of these processes, the search for new materials with desirable properties for spin currents has become an increasingly active area of research [15]. These attributes include a strong spin-orbit coupling (SOC), allowing for efficient spin-to-charge conversion, as well as a high spin polarization, which can be achieved in half-metallic materials, for example [16]. Two material classes that have gained extensive interest are the classes of two-dimensional (2D) materials and topological insulators (TI). The 2D materials offer the possibility of atomically thin interfaces, and especially graphene was shown to bear spin filtering effects and long spin diffusion lengths [17, 5]. The TIs with their conducting surface state exhibit strong SOC, and large spin-orbit torques were demonstrated in heterostructures containing TIs [18, 19]. Despite the progress of recent years, researchers are trying continuously to improve the implementation of SOT devices by a better understanding of fundamental processes and new materials to increase SOT efficiency. Especially the demand for processing higher volumes of data at a faster rate is growing as the telecommunication sector is able to transmit data at higher and higher rates, reaching up to several hundreds of Tb/s [20]. This shows the demand to create SOT devices that are able to write and read information at high speeds. With the invention of femtosecond lasers a new research field of ultrafast phenomena, including ultrafast magnetism [21] emerged. Even though progress has been made in understanding the effects on the ultrafast timescale, researchers are challenged until today to disentangle the mechanisms involved in processes like ultrafast demagnetization in ferromagnetic materials. As the operation speed of electronic circuits is limited to the GHz regime, all-optical approaches employing ultrafast laser pulses are needed for investigations of physical processes on the ultrashort timescale ($<100\,\mathrm{ps}$) [22]. The generation of THz radiation by picosecond pulsed currents is used as a means to investigate the various spin-dependent phenomena in a non-invasive way and was shown to reveal ultrafast dynamics, for example of the spin Seebeck effect [23, 24]. THz radiation, defined as the frequency range between 0.1 and 30 THz, offers a powerful tool itself, as many fundamental modes coincide with this frequency window. For a long time, this spectral regime was labeled as the so-called THz gap due to a lack of emitters covering these frequencies [25]. The spintronic emitters show bandwidths of up to 30 THz, exceeding the few THz bandwidths of their semiconductor counterparts, which are currently used in various spectroscopy applications in the medical or security sector [26, 27].

The observation of THz radiation from spintronic emitters consequently paved the way for new low-cost and broadband THz emitters. This shows that the search for new materials offering advantages in new spintronic technologies is closely entangled with the advances in spintronic THz sources.

1.2 This thesis

This work is motivated by the desire to gain insights into the generation of picosecond transient spin currents and the understanding of the spin-to-charge and charge-to-spin current conversion on the ultrafast timescale. For this, we built an experimental setup, which allows the generation and detection of THz radiation. In order to improve the spin-to-charge conversion efficiency, characterized by the spin Hall angle, different materials were investigated. It has been shown earlier that thin film multilayer structures consisting of a ferromagnetic material and a nonmagnetic material with a high spin-orbit coupling emit THz radiation with a high efficiency of spin-to-charge conversion [23, 26].
Half-metals show a very interesting characteristic for highly polarized spin currents in their band structure. At the Fermi level, the density of states exhibits a gap in one spin state, which theoretically leads to a 100% spin polarization at the Fermi level. The ferromagnetic Heusler alloy $Co_2Fe_{0.4}Mn_{0.6}Si$ was shown to be a half-metal and promising for interfacial spin transport [28, 29]. Consequently, the THz generation mechanisms in heterostructures with the ferromagnetic material consisting of $Co_2Fe_{0.4}Mn_{0.6}Si$ and different nonmagnetic layer materials are investigated.
As mentioned above, spin-orbit coupling was shown to play a major role in spin-to-charge conversion phenomena, and it is consequently a promising route to choose materials with a high SOC. In topological insulators, the high spin-orbit coupling gives rise to interesting and peculiar characteristics in their topologically protected surface states. The spin-momentum locking, describing the spin orientation aligned with the wave vector, is able to create spin-polarized surface currents [30, 19]. We investigate THz generation from heterostructures based on the role model topological insulator Bi_2Se_3, aiming to understand the influence of topology on the THz generation mechanism.

This thesis consists of the following parts:

Chapter 2 reviews fundamental concepts of ferromagnetism in solids and aims to give an overview of the generation of spin-polarized currents with the spin-pumping mechanism or the excitation of heterostructures with a femtosecond laser pulse. Additionally, spin-to-charge conversion effects like the spin-Hall effect and Rashba-Edelstein effect are discussed.

Chapter 3 gives an overview of the experimental techniques. The THz time-domain spectroscopy setup is explained, as well as additional techniques used to characterize the sample properties, including measurement of magnetic properties using the superconducting quantum interference device (SQUID) and ferromagnetic resonance spin pumping experiment.

Chapter 4 covers THz generation results from ferromagnet/normal metal (FM/NM) heterostructures and gives an overview of the experimental characteristics of the THz generation process via the inverse spin-Hall effect.

Chapter 5 summarizes the results obtained from CFMS Heusler alloy/NM bilayers. The chapter starts with an overview of Heusler alloys and their promising properties for THz generation and spintronic devices. It is followed by the results obtained with the time-domain spectroscopy setup and is complemented with results from ferromagnetic resonance experiments.

Chapter 6 is the last experimental chapter and starts with an introduction to topological insulators, the sample system investigated in this chapter. It summarizes the THz generation investigations of Bi_2Se_3 wedge heterostructures with different thicknesses and elemental compositions.

Chapter 7 compiles the conclusions of the preceding experimental chapters and gives an outlook on possibilities for further studies.

Chapter 2

Theoretical background

2.1 Ferromagnetism in 3d-transition metals

Ferromagnetism falls under the category of collective magnetism. It describes the phenomenon that dipolar magnetic moments m_i in a solid with the volume V show a long-range parallel alignment, even in the absence of an external magnetic field. The parallel alignment leads to a spontaneous macroscopic magnetization M [31, 32]:

$$M = \frac{1}{V} \sum_i m_i \tag{2.1}$$

It occurs only below a certain critical temperature $\mathrm{T_C}$, the Curie temperature, which is a material-specific property. Above $\mathrm{T_C}$ thermal fluctuations destroy the parallel alignment of the magnetic moments, and the material becomes paramagnetic. At room temperature, the only elements showing long-range ferromagnetism are Fe, Co, and Ni. The orientation of the magnetic moments can be aligned along an externally applied magnetic field, and with increasing field strength more and more moments are aligning along the external field direction until a saturation magnetization M_s is reached. Ferromagnetic materials are usually classified in the categories of itinerant and localized ferromagnets, even though the assignment is rather difficult as ferromagnets usually show aspects of both categories [33]. In a solid material, the electron wave functions are hybridized and form the band structure. The degree of hybridization for the d- and f- wavefunctions determines whether a localized or band picture is needed to describe the magnetic state [34]. In the localized case, the electrons can be viewed as fixed at the atomic lattice locations, whereas the delocalized, itinerant electrons can move nearly freely through the solid. The magnetic behavior of the 3d transition metals Ni, Fe, and Co is due to the delocalized 3d electrons and can be described by the Stoner model. The ferromagnetic behavior caused by the localized electrons is expressed by the Heisenberg model and is valid for rare earth materials, like Gd, Tb or Dy, with localized 4f- and 5f-electrons [31].

Magnetism in solids originates from the exchange interaction between the electrons in the solid. The magnetic moment of each atom is determined by the orbital l and spin s magnetic moment of each electron:

$$\vec{\mu_l} = -\frac{e\mu_0}{2m_e}\vec{l} \tag{2.2}$$

$$\vec{\mu_s} = -\frac{e\mu_0}{m_e}\vec{s}\,. \tag{2.3}$$

Here e is the electron charge, μ_0 is the vacuum permeability, and m_e is the mass of the electron. This yields the overall electron magnetic moment:

$$\vec{\mu_\mathrm{e}} = \vec{\mu_\mathrm{l}} + \vec{\mu_\mathrm{s}} = -\frac{\mu_0\mu_\mathrm{B}}{}(2\vec{s} + \vec{l}) \ , \tag{2.4}$$

as a multiple of the Bohr magneton $\mu_\mathrm{B} = \frac{\mathrm{e}}{2m_e}$. The exchange interaction arises from the quantum mechanical exchange of two electrons by Coulomb interaction and obeying the Pauli principle. One can use the Heisenberg model to describe the coupling of spins S_i and S_j in the localized case with the Hamiltonian

$$H = -2\sum_{i<j} J_{ij} S_i \cdot S_j \ . \tag{2.5}$$

The exchange integral J_{ij} can be either positive, in the ferromagnetic case, or negative if the coupling is antiferromagnetic [35]. As mentioned above, the Heisenberg picture cannot be applied to the 3d transition metals, and one must consider the spin-resolved density of states (DOS). Figure 2.1(a) shows a density of states $D(E)$ for a

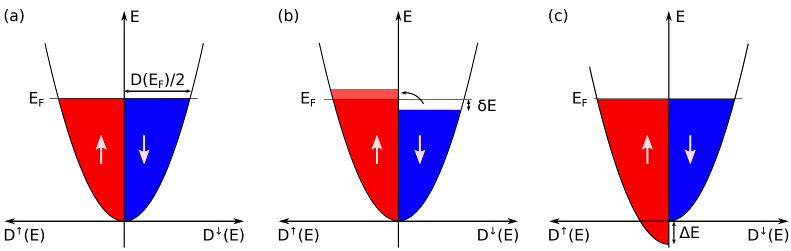

Fig. 2.1: (a) Spin-dependent density of states for a nonmagnetic material, with equally filled states for both spin states up to the Fermi level E_F. (b) Spin-dependent DOS with spin-down states redistributed to the spin-up states. (c) Spin-dependent DOS is in equilibrium with an equalized Fermi level.

nonmagnetic material, where the states are filled up to the Fermi level E_F. Defining a quantization axis, one can describe the spins to be aligned either parallel (spin-up) to the quantization axis or anti-parallel (spin-down). In the nonmagnetic case the densities of spin-up and spin-down electrons are equal $M = \mu_\mathrm{B}(n^\uparrow - n^\downarrow) = 0$. In order to have a ferromagnetic system, an imbalance between the density of spin-up $n^{\uparrow}$ and spin-down $n^{\downarrow}$ electrons needs to be present. Assuming that all spin-down electrons with an energy between $E_{\mathrm{F}}-\delta E$ and E_{F} flip their spin and populate the unoccupied spin-up states, so that each electron gains an energy δE, the total gain in the kinetic energy equals

$$\Delta E_{\mathrm{kin}} = \frac{1}{2V} D(E_{\mathrm{F}})(\delta E)^2 \ , \tag{2.6}$$

because the number of the redistributed electrons can be defined by $\delta N = \frac{1}{2}D(E_{\mathrm{F}})(\delta E)$, see Fig. 2.1(b). Now an imbalance between the spin-up and spin-down states leads to a magnetization $M = -\mu_{\mathrm{B}}(n^{\uparrow} - n^{\downarrow}) = -\mu_{\mathrm{B}}\frac{D(E_{\mathrm{F}})\delta E}{V}$. For this to be a favorable condition, the exchange interaction needs to be considered. Parallel spin alignment leads to a gain in exchange energy and $D(E)$ is shifted by $\pm\frac{1}{2}\Delta E$ for spin-up and spin-down electrons, respectively, see Fig. 2.1(c). This shift is called the exchange splitting of the density of states of a ferromagnetic system and it leads to a gain in the Coulomb energy

$$\Delta E_{\mathrm{C}} = -\frac{2I}{V} D(E_{\mathrm{F}})^2 \delta E^2 \ , \tag{2.7}$$

where I is the Stoner parameter and the total energy change in the system is therefore

$$\begin{aligned} \Delta E &= \Delta E_{\mathrm{kin}} + \Delta E_{\mathrm{C}} && (2.8)\\ &= \frac{1}{2V} D(E_{\mathrm{F}})(\delta E)^2 - \frac{1}{2V} I(D(E_{\mathrm{F}}) \cdot \delta E)^2 && (2.9)\\ &= \frac{1}{2V} D(E_{\mathrm{F}})(\delta E)^2(1 - I \cdot D(E_{\mathrm{F}})) && (2.10) \end{aligned}$$

For ferromagnetism to occur, the total change in energy must be $\Delta E < 0$, which yields the so-called Stoner criterion

$$I \cdot D(E_{\mathrm{F}}) \geq 1 \ . \tag{2.11}$$

Figure 2.2 (a) shows the DOS at the Fermi level for elements with an atomic number up to 50. In (b) the Stoner criterion for these elements is shown with Fe, Co and Ni highlighted in green, as the Stoner criterion is met and they show ferromagnetism. Elements like Pd and Pt can be easily polarized in the vicinity of a ferromagnet since the Stoner criterion for these elements is very close to 1 [36].

2.1.1 Spin-orbit coupling

The spin-orbit interaction is a relativistic quantum mechanical effect that couples the electron spin with the orbital momentum. An electron moving around the nucleus with a velocity $\vec{v}$ experiences an electric field $\vec{E}$ due to the nucleus. In the electron

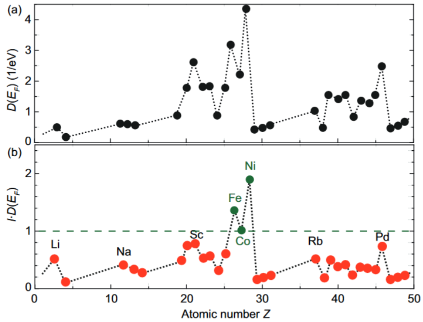

Fig. 2.2: (a) DOS at the Fermi level for elements with an atomic number Z up to 50 and (b) the Stoner criterion for these elements, being fulfilled for Fe, Co and Ni (highlighted in green). Figure taken from reference [36]

rest frame, it will experience this electric field as a magnetic field due to the Lorentz transformation $B = 1/c(v \times E)$, which will couple to the electron spin. In the quantum mechanical description, the spin-orbit coupling is embodied in the Dirac equation, and using $\vec{E}(r,t) = -\vec{\nabla}V(r)$, with the electrostatic central potential $V(r)$, the Hamiltonian can be written as

$$H = -\frac{e\ \ {}^2}{2m_e^2c^2}\frac{1}{r}\frac{dV(r)}{dr}\vec{s}\cdot\vec{l} = \xi_{nl}(r)\vec{s}\cdot\vec{l} \tag{2.12}$$

with the spin-orbit coupling parameter $\xi_{nl}(r)$, the reduced Planck constant and the speed of light c. Taking the electrostatic potential as the Coulomb potential from the nucleus $V(r) = Ze/(4\pi\epsilon_0 r)$, with the vacuum permittivity ϵ_0, the spin-orbit coupling parameter in an atom takes the form

$$\xi_{nl}(r) = \frac{Ze^2\ \ {}^2}{8\pi\epsilon_0 m_e^2 c^2 r^3}\ . \tag{2.13}$$

The spin-orbit coupling depends on the distance from the nucleus r and is directly proportional to the atomic number Z. For a hydrogen-like atom, the wave function can be split into a radial and angular part. We consider only the radial part of the wave function and retrieve the expectation value of $\langle 1/r^3 \rangle$ as Z^3. With this approximation, the spin-orbit coupling is consequently proportional to Z^4 [36, 31]. An additional impact is exerted by the specific properties of the electronic orbitals. Due to the dependence on the atomic number, the 4d transition metals are expected to show a larger SOC than the 3d transition metals. However, the node in the radial wave function of the 4d orbitals leads to a reduction of the SOC. Figure 2.3, from reference [37], shows the SOC for single atoms versus their atomic number Z. The graph shows the expected Z^4-scaling by the upper dashed line and calculated SOC values for each atoms by the colored lines. Especially for high Z values, the SOC for the 3d and

4d series can be well represented by the Z^4-scaling. If only the outermost electrons are considered for the SOC, represented by the dots in the highlighted area, the Z^2-scaling (indicated by the lower dashed line) results in values much closer to the SOC values shown for the different shells. [37]. Due to the crystal fields of the neighboring atoms, the situation in solids is different from isolated atoms, and transition metals with unfilled d-orbitals show a smaller SOC than in the atomic case [34]. Even though it is usually 10-100 times smaller (10-100 meV) than the exchange interaction, SOC impacts the electronic band structure and gives rise to magnetocrystalline anisotropy [31].

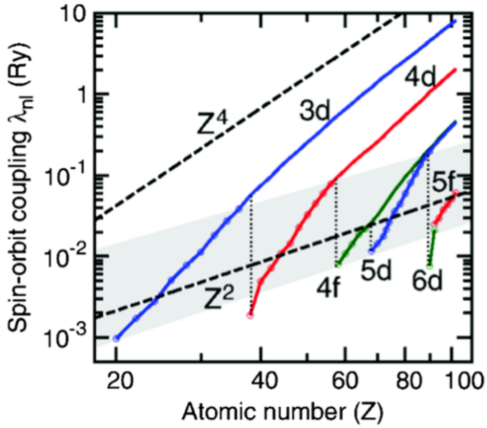

Fig. 2.3: Spin-orbit coupling parameter of atoms versus the atomic number Z in a logarithmic plot, from calculations in [38], shown by the colored lines. Additionally, the Z^4, and Z^2 dependence are shown by the dashed lines. The dots represent the SOC for the outermost electrons. From Reference [37].

2.2 Spin currents

The main concept in the field of spintronics is the use of the electron spin for the storage, readout, and processing of information. Spin-based electronic devices have several advantages over conventional ones, where the electronic property of spin is completely neglected. For a non-magnetic material, the amount of spin-up and spin-down electrons contributing to the transport is equal. The occupation probability of the energy levels $f_0(\epsilon(\vec{k}))$ in the single particle state with an energy $\epsilon(\vec{k})$ at thermal equilibrium can be described by the Fermi-Dirac distribution

$$f_0(\epsilon(\vec{k})) = \frac{1}{1 + \exp[(\epsilon(\vec{k}) - \epsilon_\mathrm{F})/k_\mathrm{B}T]} , \tag{2.14}$$

with the Boltzmann constant k_B, the temperature T and the energy at the Fermi level ϵ_F. The electron transport is governed by the electrons in the states close to the Fermi level. It is initiated by electric or magnetic fields, spatial gradients in the electron density, or scattering processes, as described by the Boltzmann equation. The current density is defined by Ohm's law $\vec{J} = \hat{\sigma} \cdot \vec{E}$, where $\hat{\sigma}$ is the conductivity tensor, resulting from integration over the Fermi surface

$$\hat{\sigma} = \frac{e^2}{4\pi^3} \int_{FS} \frac{\tau(\vec{k})\vec{v}(\vec{k}) \cdot \vec{v}(\vec{k})}{v(\vec{k})} d\vec{S} \ , \tag{2.15}$$

where τ describes the relaxation due to scattering processes and $v(\vec{k})$ is the electron velocity. For the case of an isotropic or cubic system the tensor becomes a scalar that takes the form $\sigma = \frac{ne^2\tau}{m_\mathrm{eff}}$, with carrier density n and the effective mass $m_\mathrm{eff} = {}^2(\partial^2\epsilon/\partial k^2)^{-1}$ [36]. In this description of the current density, the spin alignment of the electrons plays no role. However, to describe the transport in ferromagnetic systems Mott introduced in 1935 a two-channel model, where spin-up $\sigma^\uparrow$ and spin-down $\sigma^\downarrow$ electrons contribute differently to the conductivity $\sigma = \sigma^\uparrow + \sigma^\downarrow$, with $\sigma^\uparrow + \sigma^\downarrow$ [39]. It can be seen from Fig. 2.1 (c) that the effective mass m_eff, which is related to the band curvature, and the DOS at the Fermi level are different for spin up and spin down electrons. This in turn leads to a difference in the number of final states available after scattering processes. Similarly, SOC can lead to a difference in the scattering times τ for the two different channels so the main parameters influencing the conductivity are different for spin-up and spin-down electrons. A polarization of the current can be defined as

$$P \quad \frac{N^\mathrm{maj} - N^\mathrm{min}}{N^\mathrm{maj} + N^\mathrm{min}} \ , \tag{2.16}$$

where N^maj and N^min describe the DOS at the Fermi level for the majority and minority spin channels. It is important to remember that a spin current is a non-conserved quantity, and spin-flip scattering can lead to an exchange between the two spin channels. The spin-flip scattering due to magnetic impurities, electron-electron scattering, or SOC is usually small in the 3d transition metals but can be much larger when taking into account, e.g. heavy metals [40]. If a paramagnetic layer is connected to a ferromagnet, it is possible to create a spin accumulation in the paramagnetic material and induce a magnetic moment in the paramagnetic layer. The gradient in the spin density across the interface can result in a spin current counteracting the spin imbalance. If spin diffusion length λ_sf describes the decay of the spin accumulation in the layer along the direction perpendicular to the FM/NM interface, then:

$$P(x) = P_0 \exp\left(-\frac{x}{\lambda_\mathrm{sf}}\right) \ , \tag{2.17}$$

where P_0 describes the initial spin accumulation induced in the layer. Taking into account also spin conserving scattering processes, which occur 3 orders of magnitude more often over the mean free path l, the spin diffusion length takes the form

$$\lambda_{\mathrm{sf}} = \sqrt{\frac{l v_{\mathrm{F}} \tau_{\mathrm{sf}}}{3}} \, . \tag{2.18}$$

The spin diffusion length depends on the crystal structure and the purity of the material, which both influence on the spin-flip processes [36]. Typically, Cu is known for its long spin diffusion length exceeding 100 nm and is often used as an interlayer in heterostructures, where spin currents are flowing. On the other hand, heavy metals, like Pd or Pt, show only very small spin diffusion length in the range of a few nm due to the high SOC. Because the spin diffusion length depends on many material and structural characteristics, spin diffusion lengths usually show a range of values and differ depending on how the spin diffusion length is measured [41]. Besides describing the flow of electric charge with a defined spin orientation, spin currents can describe also the pure transport of spin angular momentum without any charge flow. These spin waves are collective excitations of coherent magnetization dynamics excited, e.g. via spin pumping, and are promising for spintronic devices as they minimize ohmic losses and allow spin injection to nonmagnetic materials via ferromagnetic insulators [42, 43].

2.3 Generation of spin currents

2.3.1 Spin pumping

Landau-Lifshitz-Gilbert equation

The spin pumping effect is used for the spin current generation between FM/NM hetero structures with the help of magnetization dynamics. A precessional motion of the magnetization M is initiated via ferromagnetic resonance (FMR) by a microwave field h_{rf}, which is applied to the heterostructure. The flow of angular momentum across the interface is initiated by the precession of the localized 3d-electron spins, which can be described by the magnetization M inside the ferromagnetic layer. They are coupled to the conduction electrons via the exchange interaction J_{ex}, which leads to a non equilibrium spin accumulation $\delta m(t)$ and results in a diffusion of spins along x, as shown in Figure 2.4. A phenomenological description of the precessional motion is given by the Landau-Lifshitz-Gilbert (LLG) equation [44]:

$$\frac{\mathrm{d}M(t)}{\mathrm{d}t} = -\gamma M(t) \times H_{\mathrm{eff}} + \frac{\alpha}{M_{\mathrm{s}}} M(t) \times \frac{\mathrm{d}M(t)}{\mathrm{d}t} \tag{2.19}$$

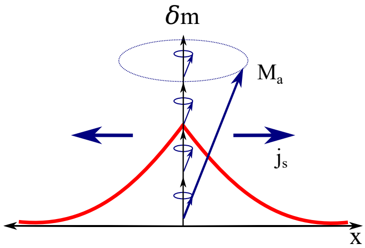

Fig. 2.4: Schematic description of spin pumping from a ferromagnetic sheet at x=0 in a electron gas of normal metal.

The first term on the right side describes the precessional motion of magnetization caused by the field h_{rf}, which is included in the effective field $H_{\mathrm{eff}} = H_{\mathrm{ext}} + h_{\mathrm{rf}}$. This term can be derived from quantum mechanical descriptions [44]. The second term is a phenomenological term describing the damping of the magnetization dynamics via the Gilbert damping α. M_{s} stands for the saturation magnetization of the ferromagnet and γ is the gyromagnetic ratio, describing the ratio between the magnetic moment and the angular momentum [42]. The correlation between resonance frequencies f_{res} and the external applied magnetic field H is described by the Kittel Formula

$$f_{\mathrm{res}} = \frac{\gamma}{2\pi}\sqrt{(H_{\mathrm{K}} + H)(H_{\mathrm{K}} + H + 4\pi M_{\mathrm{eff}})} \tag{2.20}$$

for an in-plane magnetized film sample [45]. Here γ is the gyromagnetic ratio, H_{K} is the anisotropy field and $4\pi M_{\mathrm{eff}}$ is the effective magnetization of the sample.

2.3.2 Optical excitation with fs-laser pulses

The investigation of processes following the excitation of a ferromagnetic material by a fs laser pulse was the focus of many research groups since the first observation of the ultrafast magnetization quenching in a Nickel thin film by Beaurepaire et al. in 1996 [21]. Different physical mechanisms have been suggested, which can be categorized into spin-flip scattering- [46, 47, 48, 49] and spin-transport phenomena [50, 51]. The authors in Malinkowski et al. [52] were the first to observe a spin current triggered by optical excitation and its effect on ultrafast demagnetization. This phenomenon was initially observed in a Co/Pt system and has since been demonstrated in other heterostructures as well [53].

The illumination of the sample with a 1.55 eV fs laser pulse leads to the excitation of hot electrons and excites them into free states above the Fermi level E_{F}. The spin dependent density of states (DOS) of a ferromagnetic system is shown in Fig. 2.5 (a), where the arrows indicate the transitions for electrons excited by the laser pulse. Spin majority electrons are mainly excited into sp-like states, with a high velocity, whereas

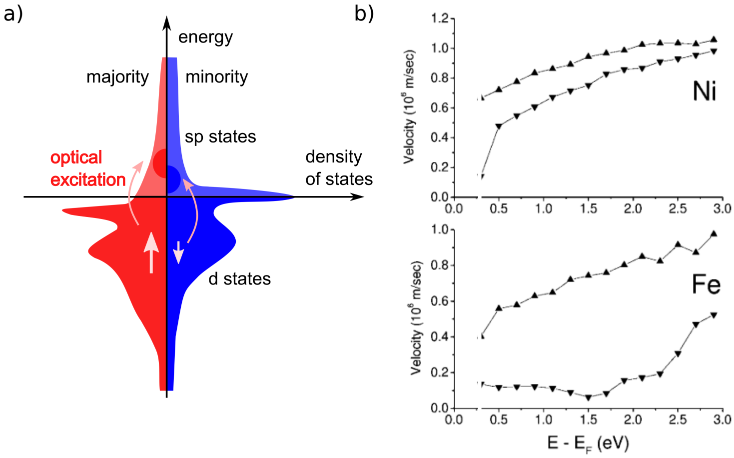

Fig. 2.5: (a) Spin-dependent density of states in a ferromagnetic system. Arrows indicate the excitation of d-like states into sp like states under optical excitation for the majority electrons and the excitation into d-like states for the minority electrons. (b) Spin dependent DOS for Ni (top) and Fe (bottom) taken from Ref. [54]. The triangles pointing upwards represent the spin-majority electrons and the triangles pointing downwards the spin-minority electrons.

spin minority electrons are excited mainly into d-like states with a lower velocity. This is especially true for Fe comparing the velocities of majority and minority electrons around 1.55 eV above E_F shown in Fig. 2.5 (b), taken from Ref. [54]. After the excitation the electrons will isotropically move in all possible directions, because of a small linear momentum carried by the absorbed photon [50]. To describe the flow of electrons inside the ferromagnetic layer and even across the FM/NM interface Battiato et al. derived the model of superdiffusive spin currents resulting in the equation

$$\frac{\partial n^{\mathrm{tot}}}{\partial t} + \frac{n^{\mathrm{tot}}}{\tau} = \left(-\frac{\partial}{\partial z}\hat{\Phi} + \hat{I}\right)\left(\hat{S}n^{\mathrm{tot}} + S^{\mathrm{ext}}\right) , \tag{2.21}$$

describing the change in the total electron density n^{tot}, $\hat{I}$ is the identity operator and τ is the electron lifetime. S describes the electron source term, with S^{ext} standing for the source term initiated by the fs laser pulse. The electrons are divided into multiple generations depending on the number of scattering events and the operator $\hat{S}$ acts on $n^{[x]}$ and gives the new source term $\hat{S}n^{[x]} = S^{[x+1]}$. The operator $\hat{\Phi}$ acts on the source term and gives the electron flux $\hat{\Phi}S^{\mathrm{ext}} = \Phi$ [50]. The difference to a normal diffusion via Brownian motion, which is characterized by a linear time dependence of the mean square displacement $\langle x^2(t)\rangle = K_\alpha t^\alpha$ with $\alpha = 1$, lies in the coefficient α, which is 2 for a ballistic transport and $\alpha > 1$ for the superdiffusive regime [55]. To understand the different transport properties for spin majority and spin minority electrons the authors in [54] calculated the inelastic mean free path (IMFP) separately for both spin states using GW+T calculations and the results are shown in Fig. 2.6. They show that the asymmetry in the IMFP in Fe is dominated by the difference in velocity compared to the case of Ni, where the asymmetry is dominated by a spin dependent difference in the lifetime of the electrons. Using a pump beam with 1.55 eV the asymmetry in the IMFP between spin majority and spin minority electrons is around 7 for the case of Ni [54].

We want to understand now what is driving the electrons. Fognini et al. [56] derived a thermodynamical model describing the driving force of the spin current by a gradient in the spin dependent chemical potential $\mu_{\uparrow,\downarrow}$. By absorbing the laser pulse a temperature gradient ∇T is induced in the ferromagnet because the surface can be heated to around 1000 K and is therefore hundreds of degrees higher compared to the FM/NM interface. The increased temperature leads to a spin dependent shift of the chemical potentials. The difference in the temperatures leads to a spin dependent gradient in the chemical potentials, which initiates the electron transport. They start with an equation for an isotropic single domain ferromagnet from Ref. [57]

$$\begin{pmatrix} \vec{j}_{\mathrm{c}} \\ \vec{j}_{\mathrm{s}} \\ \vec{Q} \end{pmatrix} = \sigma \begin{pmatrix} 1 & P & ST \\ P & 1 & P'ST \\ ST & P'ST & \kappa T/\sigma \end{pmatrix} \begin{pmatrix} \nabla\mu_{\mathrm{c}}/q \\ \nabla\mu_{\mathrm{s}}/2q \\ -\nabla T/T \end{pmatrix} , \tag{2.22}$$

where $\vec{j}_{\mathrm{c,s}}$ and Q describe the charge-, spin- and heat currents, q is the electron charge, P is the polarization of the conductivity and is described by $P = \frac{\sigma^{(\uparrow)} - \sigma^{(\downarrow)}}{\sigma}$ and $P' = \frac{\partial(P\sigma)}{\partial\epsilon}|_{\epsilon_{\mathrm{F}}}$. Furthermore S describes the Seebeck coefficient and κ the thermal conductivity. The Seebeck coefficient can be described via $S = \frac{\sigma^{(\uparrow)}S^{(\uparrow)} + \sigma^{(\downarrow)}S^{(\downarrow)}}{\sigma^{(\uparrow)} + \sigma^{(\downarrow)}}$ and the charge conductance is defined by the spin dependent conductivities $\sigma = \sigma^{(\uparrow)} + \sigma^{(\downarrow)}$. Finally the charge electrochemical potential is defined as $\mu_{\mathrm{c}} = \frac{\mu^{(\uparrow)} + \mu^{(\downarrow)}}{2}$ and the spin accumulation, caused by different conductivities for majority and minority spin electrons, as $\mu_{\mathrm{s}} = \mu^{(\uparrow)} - \mu^{(\downarrow)}$. In the case of a pure spin current $\vec{j}_{\mathrm{c}} = 0$ and the spin current density takes the form:

$$\vec{j}_{\mathrm{s}} = \sigma \left(\frac{\nabla\mu_{\mathrm{s}}}{2q}(1 - P^2) + S\nabla T(P - P') \right) , \tag{2.23}$$

where the first term describes the spin current driven by the difference in the chemical potential and the second term the spin current driven by the Seebeck effect. A comparison shows that for conditions with high temperatures reached during the laser excitation the Seebeck term becomes negligible so that

$$\vec{j}_{\mathrm{s}} = \sigma \left(\frac{\nabla\mu_{\mathrm{s}}}{2q}(1 - P^2) \right) . \tag{2.24}$$

is driven by the gradient in the spin dependent chemical potential $\nabla\mu_{\mathrm{s}}$.

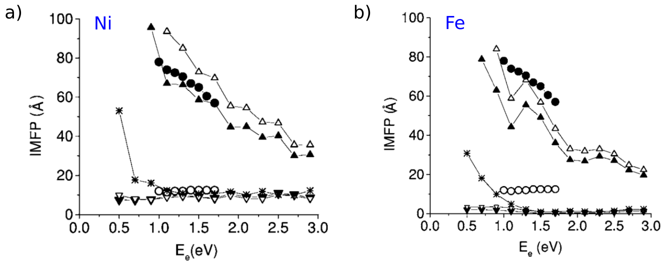

Fig. 2.6: (a) Calculated inelastic mean free path (IMFP) for Ni and (b) for Fe. Open and closed triangles, as well as the stars, represent calculated values for the IMFP (using different approximations, further information can be found in [54]), whereas the circles show experimental results for $Ni_{80}Fe_{20}$. Upward pointing triangles and closed circles mark the spin majority IMFP and the downward pointing triangles and open circles the spin minority electron IMFP.

2.4 Spin-to-charge conversion

2.4.1 History of Hall effects

The birth of the research field of investigating Hall effects dates back to 1879 when Edwin H. Hall discovered that, due to the Lorentz force, a current flowing through a conductor generates a transverse voltage in the present of a magnetic field [58]. Only a few years later Hall observed, that the effect is much stronger in ferromagnets [59]. This effect is known today as the anomalous Hall effect. In addition to the contribution from the Lorentz force an additional temperature dependent contribution is present due to the magnetic moments in the ferromagnet. However, the effect is not limited to ferromagnetic materials, but also arises in paramagnetic and antiferromagnetic materials, where localized magnetic moments are present. The direction of the generated transverse voltage is correlated with the spin orientation and therefore leads to an additional contribution in materials with localized magnetic moments, because of asymmetric scattering processes for spin-up and spin-down electrons. The current density in a ferromagnetic material is composed of three different contributions containing the normal electrical conductivity σ_0, the ordinary Hall conductivity $\sigma_{\mathrm{H}}^{(0)} = \sigma_{\alpha\beta}^{(0)}$ and the anomalous Hall conductivity $\sigma_{\mathrm{H}}^{(1)}$

$$J_\alpha = \sigma_{0,\alpha\beta} E_\beta + \sigma_{\alpha\beta}^{(0)} E_\beta B_\gamma + \sigma_{\alpha\beta\gamma}^{(1)} E_\beta M_\gamma \ , \tag{2.25}$$

with $\sigma_{\alpha\beta\gamma}^{(1)} = \sigma_{\mathrm{H}}^{(1)} \epsilon_{\alpha\beta\gamma}$, using the antisymmetric tensor ϵ, and α, β and γ stand for the spatial directions [60]. In the process of understanding the underlying physical mechanisms leading to the transverse voltage Karplus and Luttinger found in 1954 that an intrinsic contribution is due to the spin orbit coupling of the material, which generates a transverse velocity between the scattering events [61]. Extrinsic contributions were found by Smit and Berger, who suggested the skew scattering and the side jump mechanisms to contribute to the transverse velocity during the scattering events [62, 63, 12]. In 1971 a theoretical description of a phenomenon known as the spin Hall effect was made by Dyakonov and Perel [64, 65] and the principle is schematically shown in Fig. 2.7 (a). They describe the accumulation of spin polarized electrons at the side of a conductor, the creation of a so called transverse spin voltage, when a current is flowing through the conductor. It took around 30 years to experimentally observe the spin accumulation via the optical Kerr-effect by Kato et al. in 2004 [66]

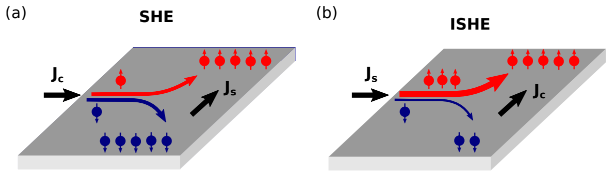

Fig. 2.7: Schematic representation of the (a) spin Hall effect (SHE), where a charge current J_c generates a transverse spin current J_s and (b) the inverse spin Hall effect (ISHE), where the process is inverted and a transverse charge current is generated by the flow of a spin current.

and Wunderlich et al. in 2005 [67] at the edges of a conductor. Until this experimental realization of measuring the spin accumulation, the spin voltage was translated back into an electrical voltage using also the inverse process, the inverse spin Hall effect, which is schematically shown in Fig. 2.7 (b). This was achieved using Hall bar structures, schematically shown in fig. 2.8. A charge current is applied along the contacts 1 and 2, which is converted into a spin current via the SHE. The spin current is flowing in the horizontal direction and in the following converted back to a charge current via the inverse SHE and measured at the contacts 3 and 4 [12].

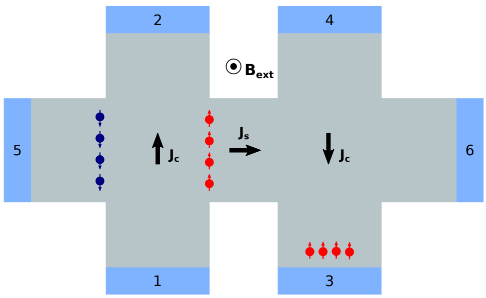

Fig. 2.8: Illustration of the double Hall-bar structure. A charge current is applied between the contact 1 and 2, which generates a spin current due to the SHE flowing in the horizontal direction. This spin current is then converted back to a charge current via the ISHE and can be measured at the contacts 3 and 4.

2.4.2 Spin-Hall effect: phenomenology

The phenomenological description developed by Dyakonov describes the interconnection of spin and charge currents starting from the conventional equations for the drift diffusion of electrons [68]. The spin current is described by a tensor q_{ij}, where j describes the spin orientation direction and i defines the flow direction of the electrons. In the absence of spin-orbit coupling the charge current $q^{(0)}$ and spin current $q_{ij}^{(0)}$ can be described in the following way:

$$q^{(0)} = -\mu n E - D\Delta n \tag{2.26}$$

$$q_{ij}^{(0)} = -\mu E_i P_j - D\frac{\partial P_j}{\partial x_i} \ , \tag{2.27}$$

with the electron mobility μ, the electron concentration n, diffusion coefficient D and the spin polarization density P. A coupling of these two currents is achieved in the presence of SOC and one obtains

$$q_i = q_i^{(0)} + \Theta_{\mathrm{SH}}\epsilon_{ijk}q_{jk}^{(0)} \tag{2.28}$$

$$q_{ij} = q_{jk}^{(0)} - \Theta_{\mathrm{SH}}\epsilon_{ijk}q_k^{(0)} \ , \tag{2.29}$$

where ϵ_{ijk} is the Levi-Civita tensor and Θ_{SH} is a dimensionless factor accounting for the coupling strength by the SOC, which is assumed as $\Theta_{\mathrm{SH}} \ll 1$. Because the spin and charge currents can be described via the Onsager reciprocal relations, a difference of the plus and minus sign is present in these two coupling relations. Using these equations one can get the following equations for the spin q_{ij} and charge currents j

$$j/E = \mu n E + D\nabla n + \beta E \times P + \delta \boldsymbol{\nabla} \times P \tag{2.30}$$

$$q_{ij} = -\mu_i E_i P_j - D\frac{\partial P_j}{\partial x_i} + \epsilon_{ijk}\left(\beta n E_k + \beta\frac{\partial n}{\partial x_k}\right) \ , \tag{2.31}$$

with $\beta = \Theta_{\mathrm{SH}}\mu$ and $\delta = \Theta_{\mathrm{SH}}D$. The term $\beta E \times P$ in equation 2.30 describes the anomalous Hall effect when a spin polarization P is present and the term $\delta\boldsymbol{\nabla} \times P$ accounts for the inverse spin Hall effect, where an electrical current is generated by a non-uniform spin density. Similarly the third term in equation 2.31 $\epsilon_{ijk}\beta n E_k$ can be related with the spin Hall effect, where a transverse spin current is generated in the presence of an electric field [68]. The parameter Θ_{SH} is also called the spin Hall angle describing the efficiency of the spin to charge conversion, and using the charge conductivity $\sigma_{xx}^c = ne\mu$ and the spin Hall conductivity $\sigma_{xy}^s = n \ \mu\Theta_{\mathrm{SH}}$ one can see that

$$\Theta_{\mathrm{SH}} = \frac{\sigma_{xy}^s}{\sigma_{xx}^c}\frac{e}{-} \ . \tag{2.32}$$

Elements with a large spin Hall angle are mainly materials with a large SOC, for example Pt, Pd or Ta [12].

2.4.3 Intrinisic contribution - anomalous velocity

As already mentioned in the beginning of this section the importance of the SOC to the AHE was first recognized by Karplus and Luttinger in 1954 [61]. It was observed that in a ferromagnetic crystal under the perturbation of an electric field, electrons will develop a velocity which is transverse to the electric field direction and the spin polarization of the electrons. This is schematically shown in Fig. 2.9 (b). This transverse velocity is labeled as an anomalous velocity and only much later was related to the Berry phase.

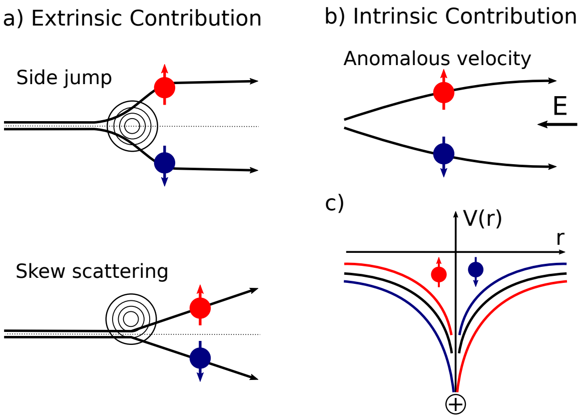

Fig. 2.9: (a) Extrinsic contributions to the SHE: the side jump effect and the skew scattering taking place under the scattering event. (b) Intrinsic contribution to the SHE from the anomalous velocity taking place in between the scattering events. (c) Couloumb scattering potential altered dependeng on the spin alignment of the scattered electron during the skew scattering process. Adapted from [69]

The anomalous velocity is proportional to the magnetization and arises due to effects of the SOC on the electronic band structure. It hence follows that the effect is not taking place during the scattering events but in between the scatterings. Considering the case of a weak electric field E and keeping the translational symmetry by using the vector potential $A(t)$ and the Hamiltonian in the q-space representation, the velocity operator is defined via $\upsilon = \partial\mathcal{H}(q,t)/\partial(\ q)$ and one can see that the velocity acquires an additional term, which is due to the Berry phase

$$\upsilon_n(k) = \frac{\partial\epsilon_n(k)}{\partial k} - \frac{e}{}E \times \Omega_n(k) \ , \tag{2.33}$$

where $\Omega_n(k)$ is the Berry curvature as described previously

$$\Omega_n(k) = i \langle \nabla_k u_n(k)| \times |\nabla_k u_k(k)\rangle \ . \tag{2.34}$$

Here ϵ_n are the eigenenergies and u_n are the eigenfunctions, with a gauge invariant crystal momentum $k = q + \frac{e}{}A(t)$. From the Kubo formula one can get the Hall conductivity as

$$\sigma_{xy} = e^2 \sum_{n\neq m} \int_{BZ} \frac{d^3k}{(2\pi)^3} f_n(k) \mathfrak{Im} \frac{\langle u_m| v_x |u_n\rangle \langle u_n| v_y |u_m\rangle}{(\epsilon_n - \epsilon_m)^2} \tag{2.35}$$

$$= e^2 \sum_{n\neq m} \int_{BZ} \frac{d^3k}{(2\pi)^3} f_n(k) \Omega_{k_x k_y} \ , \tag{2.36}$$

where $f_n(k)$ is the Fermi-Dirac distribution [70, 69, 71, 72, 12]. A full description can be found in reference [70]. The intrinisc contribution to the spin Hall conductivity is proportional to the spin-orbit polarization at the Fermi level, as was seen in [73], which leads to the fact that the spin Hall conductivity in transition metals is positive for a more than half filled d-shell and negative for a less than half filled d-shell

$$\sigma_{xy}^{s_z} \approx \frac{e}{4a} \frac{\langle l \cdot s\rangle_{FS}}{2} \ , \tag{2.37}$$

with the lattice constant a, see Fig. 2.10 a) [12, 73]. In Reference [74] first principle calculations for the intrinsic spin Hall effect in Pt were made and the authors see that the spin Hall conductivity is dominated by points in the band structure were the SOC splits up degenerated bands, because the Berry curvature is taking non-zero values exactly at these points. The Berry curvature shows opposite values for the two sides of the gap and the two contributions are uncompensated if the Fermi level is lying in the gap, see Fig. 2.10 b).

2.4.4 Extrinsic contributions

The extrinsic contributions to the spin Hall effect are the spin-dependent scattering effects, the skew scattering and side jump effects, which similarly have their origin in the SOC and are schematically shown in Fig. 2.9 (a). The spin skew scattering is also known as Mott scattering described in [75] and the Sherman function can help to evaluate the probability of spin up and spin down electrons to be scattered to the left or right in a certain experimental configuration cite [76]. The skew scattering was first proposed by Smit as a contributing factor for the AHE [62]. One can consider a collision between an electron and a nucleus in the rest frame of the electron, which is governed by the Coulomb interaction. The electron experiences a magnetic field gradient due to the SOC, which leads to a correction of the Coulomb scattering potential,

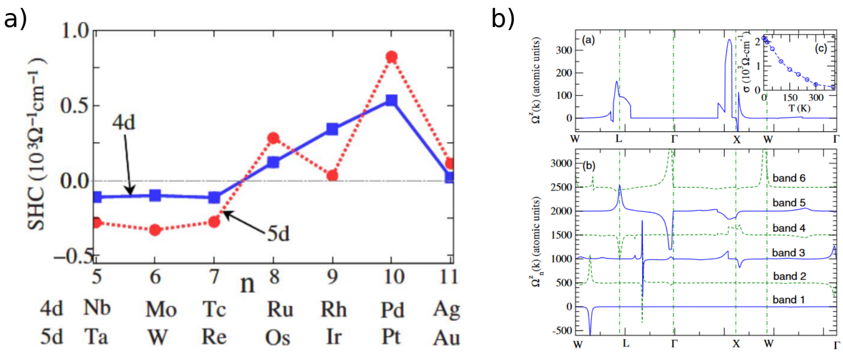

Fig. 2.10: (a) Spin Hall conductivity calculated for 4d and 5d elements showing negative values for a less than half filled d-shell and positive values for a more than half filled d-shell, taken from [73] (b) Berry curvature calculated for each band in Pt, showing non-zero values at positions in where degenerate bands are split up due to the SOC, which in Pt is the case for the X and L point, taken from [74].

see Fig. 2.9 (c),

$$V_{SO} = \vec{\mu}_s \cdot \vec{B} = -g_s \mu_{\mathrm{B}} \frac{\vec{S}}{\ } \tag{2.38}$$

This correction is spin dependent and will lead to a deflection of the electrons in opposite directions for the case of an opposite spin alignment. It was found that the skew scattering can be a dominant contribution to the SHE in the case of a high purity sample and low temperatures. In the case of impurity atoms, for example in interface regions, the magnitude of the skew scattering is determined by the ratio of the SOC of both atoms. The magnitude and also the sign of the skew scattering can vary depending on the configuration and could be different for the case of light impurity in a heavy host material or vice versa [12, 77, 78].

On the contrary the side jump effect describes a sideways displacement Δy for the center of mass of an electron wave packet in the presence of spin orbit coupling. It was described by Berger in 1970 [63] and is usually a small contribution compared to intrinsic or skew scattering one. However, the effect is proportional to the impurity concentration and can therefore become important for a high impurity concentration. Berger found that the center of mass shows a time dependent displacement which is due to the intrinsic contribution to the SHE, but also shows a time independent component, which is the side jump effect and can be of the order of 10^{-16} m [12, 63].

2.5 Spin-to-charge conversion in 2D

2.5.1 Semiconductor interfaces

Bringing a semiconductor in contact with a metal, band bending can be observed at the interface, as shown in Fig. 2.11. The important parameter defining the band bending is the work function Φ of the metal and the semiconductor. Bringing the two in contact leads to a transfer of electrons to compensate for the mismatch of the Fermi level. If the metal has a higher work function compared to the semiconductor $\Phi_m > \Phi_s$ as shown on the left side of Fig. 2.11 the bands of the semiconductor are bending upwards and form a depletion layer at the interface region. On the contrary, if $\Phi_m < \Phi_s$ the bands at the interface are bending downwards and an accumulation layer is formed. The degree of the band bending is described by the difference of the work function of the two layers:

$$V_{\text{bending}} = |\Phi_m - \Phi_s| \ . \tag{2.39}$$

As a result of the band bending, a so-called Schottky barrier can be formed, which blocks the electron flow from the metal to the semiconductor [79]. An interesting case occurs in the presence of a strong downward bending of the semiconductor bands at the interface. The conduction band of the semiconductor is bend below the Fermi level of the metal and confines the electrons in this potential well, as shown in Fig. 2.12 for a AlGaN/GaN junction. This situation is called a two dimensional electron gas (2DEG), where the electrons are confined to move within a thin layer or sheet of a semiconductor surface or heterojunction. The electrons are free to move in two dimensions, but are confined in the third dimension due to the potential barrier created by the semiconductor materials.

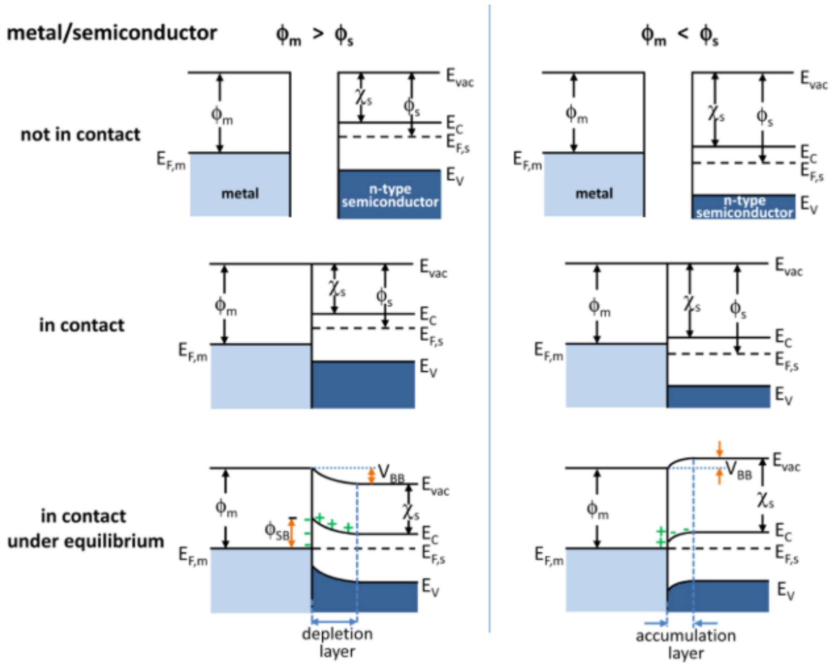

Fig. 2.11: Occurrence of the band bending when bringing a metal and a semiconductor into contact. The left side shows the case for a higher work function in the metal $\Phi_m > \Phi_s$ and the resulting upward bending. On the right side the downward band bending due to the higher work function of the semiconductor $\Phi_m > \Phi_s$ is shown. The image is taken from [79].

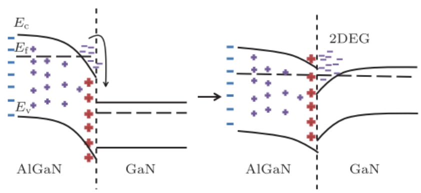

Fig. 2.12: Creation of a 2 dimensional electron gas (2DEG) in the case of a contact between AlGaN and GaN. The image is taken from [80].

2.5.2 Rashba-Edelstein effect

The spin-to-charge conversion process in a two dimensional electron gas is described by the Rashba-Edelstein effect: a spin accumulation of conduction electrons is converted to a charge current or vice versa [81]. The underlying effect is the Rashba effect,

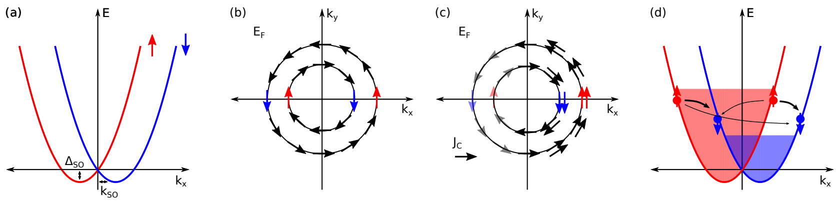

Fig. 2.13: a) Rashba split energy dispersion for systems with a broken inversion symmetry. b) shows a cut of the energy bands in a) at the Fermi energy. c) In the presence of a charge current J_c a spin accumulation with an orientation perpendicular to the current flow is generated. d) The other way around a spin accumulation is generating a charge current along k_x. The scattering probability is proportional to Δk_x of the initial and final state and is represented by the arrow thickness. Figures adapted from [36, 82].

which describes the k-dependent spin splitting of the energy bands, first observed by Emmanuel Rashba in 1959 for three dimensional systems and in 1984 by Yurii A. Bychkov for the two dimensional case [83]. The origin of the Rashba effect is the spin-orbit coupling in crystals with a broken inversion symmetry. In the 2D case the electrons feel an electric field $\nabla\Phi \approx -E_z\hat{z}$ originating from the potential gradient normal to the 2D plane. This leads to a Hamiltonian of the form [36]

$$H = \frac{{}^{2}}{2m_\mathrm{e}}k_\parallel^2 + \alpha_\mathrm{BR}\vec{\sigma}\cdot(\vec{k}_\parallel \times \hat{z}) \ , \tag{2.40}$$

where the first term is the kinetic energy and second term is the spin-orbit term with the Rashba-Bychkov parameter $\alpha_\mathrm{BR} \approx {}^{2}\partial_z\Phi/4m^2c^2$. For an electron moving in the 2D plane with $\vec{k}_\parallel = (k_x, k_y, 0) = k_\parallel(\cos\phi, \sin\phi, 0)$ the eigenfunctions become:

$$\Psi_{\pm\vec{k}_\parallel}(\vec{r}_\parallel) = \frac{e^{i\vec{k}_\parallel\cdot\vec{r}_\parallel}}{2\pi}\frac{1}{\sqrt{2}}\begin{pmatrix} ie^{-i\phi/2} \\ \pm e^{i\phi/2} \end{pmatrix} \tag{2.41}$$

with the eigenstates

$$\epsilon_\pm(k_\parallel) = \frac{k_\parallel^2}{2m_\mathrm{e}} \pm \alpha_\mathrm{BR}|k_\parallel| = \frac{{}^{2}}{2m_\mathrm{e}}(k_\parallel \pm k_\mathrm{SO})^2 - \Delta_\mathrm{SO} \ . \tag{2.42}$$

This shows the characteristic of the energy bands in the presence of a Rashba SOC, schematically shown in Fig. 2.13 a): the energy bands are spin split with a splitting linear in $k_{\|}$

$$\epsilon_{+}(\vec{k}_{\|}) - \epsilon_{-}(\vec{k}_{\|}) = 2\alpha_{\mathrm{BR}}k_{\|} \ . \tag{2.43}$$

Additionally the spin split bands are shifted by a factor $k_{\mathrm{SO}} = m_{\mathrm{e}}\alpha_{\mathrm{BR}}k_{\|}$ and lowered in energy by $\Delta_{\mathrm{SO}} = m_{\mathrm{e}}\alpha_{\mathrm{BR}}^2/(2\quad{}^2)$. Cutting through the energy dispersion at the Fermi energy results in the chiral spin alignment shown in Fig. 2.13. The possibilty for spin-to-charge conversion was pointed out by Edelstein and is visualized in Figure 2.13 c) and d). In the presence of a charge current J_{c} the electrons are redistributed along k and result into a spin accumulation due to an asymmetry in the density of states for spin up and spin down electrons. On the contrary, an injected spin polarization results in a charge current along k_{x}. The spin-flip scattering probability depends on the difference between the initial and final k-vector, visualized by the arrow thickness in Figure 2.13 (d). The difference in the scattering probability with respect to the direction in k_{x} leads to an effective current flow [84, 36].

Chapter 3

Experimental

3.1 Optical THz emission setup

The setup used for the generation of THz radiaton from the different sample systems is illustrated in Fig. 3.1. The laser oscillator employed in the optical setup is a diode pumped MaiTai Ti:sapphire oscillator from Spectra-Physics. The MaiTai laser head consists of two chambers, where one contains the diode pumped continuous wave (CW) 'Millenia'-type Nd:YVO_4 pump laser with a wavelength of 1064 nm. The pump light of the diodes, located in the laser power supply, are coupled via optical fibers into both ends of the Nd:YVO_4 crystal. Using a temperature-controlled lithium triborate (LBO) nonlinear crystal with non-critical type two phase-matching the wavelength is frequency doubled and generates a beam with 5 W of output power and a wavelength of 532 nm. In the Ti:sapphire crystal the 532 nm CW beam is frequency doubled and pulsing is achieved via Kerr-lense mode-locking in the Ti:sa crystal. The output power of the MaiTai oscillator is approximately 800 mW and is split into two branches with a 10:90 intensity ratio. The low intensity branch is guided to the photoconductive antenna (PCA) and used for gating the PCA. The beam is focused on the PCA, which consists of low temperature grown GaAs, and generates free carriers. Once a THz pulse is hitting the PCA, the carriers feel the electric field of the THz pulse and are accelerated between the two antenna notches so that the THz electric field can be measured. The higher intensity beam is first guided over a delay stage, which ensures the control of the time delay between the pulses in the two branches. After passing the delay stage, the high intensity beam is focused on the sample by a lens with a focal length of 60 mm and initiates the process of THz generation in the sample structures. A magnetic field with a maximum of 270 mT (215 kA/m) is applied in the plane of the sample. The generated THz radiation is first collimated by a teflon lens with a focal length of 50 mm and afterwards focused onto the PCA with a Si focal length. Figure 3.1 (a) shows the setup in a transmission geometry, where the pump beam illuminates the THz emitter from one side and the THz radiation is detected on the other side.

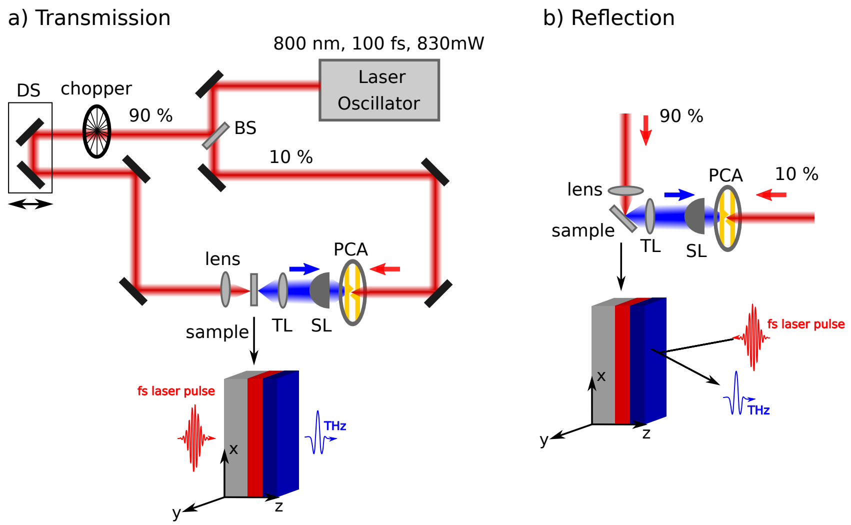

Fig. 3.1: Optical setup for the generation of THz transients from the sample systems shown in (a) for the configuration in transmission and in (b) for the configuration in reflection.

In the reflection configuration shown in Fig. 3.1 (b) the sample is hit by the pump beam under 45° incidence angle and the THz radiation is detected from the same side under 45°. The signal measured at the PCA is first preamplified and measured with a lock-in amplifier. A chopper is placed in the high intensity arm, with a frequency of 520 Hz.

3.2 Detection of terahertz radiation

For the detection of the terahertz radiation a photoconductive antenna (PCA) from Teravil was used. The antenna consists of low-temperature grown GaAs photoconductive material, which was found to have advantages compared to a PCA consisting of GaAs. The LT-grown GaAs shows a high carrier mobility of around 200 $cm^2/(V{\cdot}s)$, a short carrier lifetime below 0.5 ps, a high electrical resistivity of 10 $M\Omega{\cdot}cm$ and higher crystallinity after the annealing process [85, 86]. The antenna tips have a distance of 6 μm and are arranged a little off-centered, as can be seen in Fig. 3.2. Photoconductive antennas can be used for both, the detection as well as the generation of THz radiation. In the case of detection of THz generation a low-power 800 nm beam is used to excite the antenna from one side (low intensity branch in Fig. 3.1). Free carriers are generated and the detector is set to an "open" state for detection. If a THz electric field is incident on the PCA from the other side of the antenna the generated free electrons are accelerated by the electric field of the electromagnetic radiation and oscillate between the antenna apices. Using a signal preamplifier and a lock-in amplifier one can measure the voltage between the antenna tips and hence the electric field of the THz radiation. For the measurement of s-polarized THz pulses the antenna is placed with the apices in the vertical direction, configuration in Fig. 3.1 and Fig. 3.2 a). In this alignment configuration the electric field in E_x direction is detected. If the antenna is rotated by 90° and the antenna notches are pointing in the horizontal direction the antenna is sensitive of the p-polarized E_y component of the emitted THz radiation as shown in Fig. 3.2 b).

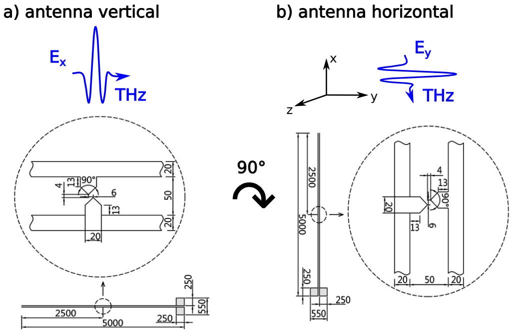

Fig. 3.2: Two different antenna alignments to measure the THz radiation polarized in the a) vertical direction E_x and b) the horizontal direction E_y. The numbers show distances, dimensions and angles of the antenna in μm.

3.3 Ferromagnetic resonance

For the generation of a spin current via spin pumping the samples were placed on a coplanar waveguide (CPW) transmission line. The CPW transmission line, shown in Fig. 3.3 a), consists of a Rogers RO4003C board, with a thickness of 0.508 mm and a 35 µm thick copper layer on top, capped with a 0.05 µm zinc layer. The CPW impedance is 51.31 Ω. A radio frequency signal was applied perpendicular to the transmission line and the changes of the RF signal passing through the transmission, the S_{12} parameter, were detected by a vector network analyzer (VNA). The VNA allows the measurement of S_{12} as the ratio of the transmitted signal and the incident signal. The external magnetic field is applied in the plane of the sample and parallel to the transmission line. The RF field h_{rf} is perpendicular to the transmission line. For the measurement, the frequency of the RF signal is sweeped from 50 MHz up to 20 GHz at a set of constant magnetic fields ranging from 0 up to 160 kA/m. A typical frequency sweep is shown in Fig. 3.3 b). The resonance peak occurs when the Larmor freuqency Ω_L is met such that the absorption of the RF signal inside the sample is

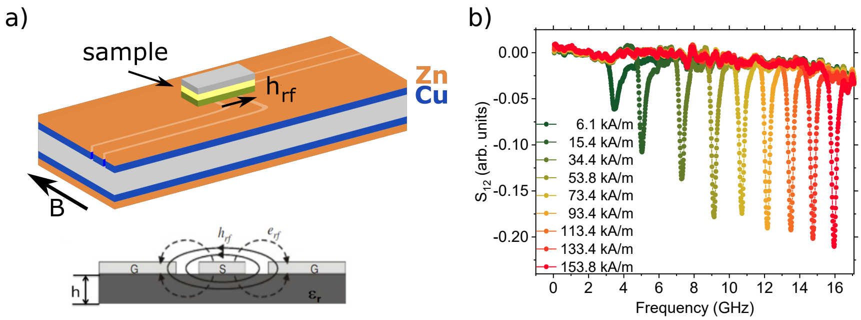

Fig. 3.3: (a) Schematic illustration of FMR measurement using the CPW transmission line. The sample is placed on top of the transmission line and the magnetic field and RF signal are applied perpendicular to the transmission line. The bottom image shows a side cut of the transmission line, where G and S stand for ground and source, respectively, and the field lines of the RF field around the transmission line. Bottom image taken from [87] (b) shows typical absorption curves, when the frequency is swept at different constant magnetic field values. The shift of the resonance peak is in accordance with the Larmor frequency in equation 3.1.

maximal

$$\Omega_{\mathrm{L}} = g\mu_{\mathrm{B}} \cdot H \ , \tag{3.1}$$

with the Landé factor g, the Bohr Magneton μ_{B} and the magnetic field H [87].

3.4 MPMS-SQUID

To characterize the in-plane magnetic properties of the samples a MPMS (Magnetic Property Measurement System)-XL SQUID (Superconducting Quantum Interference Device) magnetometer from Quantum Design was used. The system allows the measurement of RSO (reciprocating sample option) with a high sensitivity of 10^{-8} emu. The high sensitivity is determined by the Josephson effect allowing to measure very

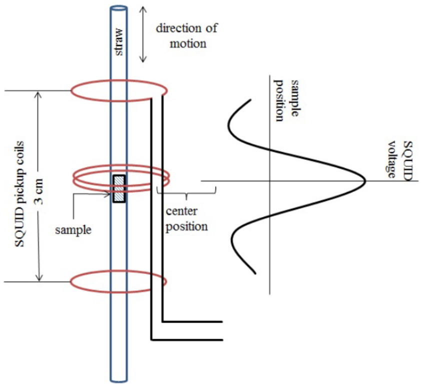

Fig. 3.4: Schematic layout of the MPMS SQUID. The sample is placed inside a plastic straw between the SQUID pick up coils and the maximum SQUID voltage is found by centering the sample inside the coils. The sample is then forced to oscillate vertically inside the pick up coils so that the magnetic flux is changed. Taken from reference [88]

small changes in the magnetic flux. For the measurement the sample is placed inside a superconducting ring where it oscillates with a frequency of 2 Hz and hence induces a magnetic flux, see Fig. 3.4. According to Faraday's law of induction it will lead to the generation of a screening current flowing inside the ring. An applied bias current is keeping the superconductive ring above its critical current level, so that it is not superconducting. Due to the flux quantization for a superconductive ring, if the flux is changed by one flux quantum $\Phi_0 = \quad /2e = 2.068 \cdot 10^{-15}$ (T·m^2) the measured voltage is oscillating where the period of oscillations is proportional to the period of the magnetic flux and consequently gives information about the induced magnetic flux. The measurement technique is used to determine the magnetic properties of the samples down to 10 K [88, 89, 90].

Chapter 4

THz generation in metallic heterostructures

This chapter reviews the main characteristics of THz radiation obtained from THz spintronic emitters based on FM/NM heterostructures via the inverse spin Hall effect. The typical tested heterostructure has the following structure: MgO(0.5 mm)//FM/HM. In such a spintronic THz emitter, the main generation mechanism for THz radiation is the inverse spin Hall effect, which describes the conversion of a spin current $\vec{J}_\mathrm{s}$ into a charge current $\vec{J}_\mathrm{c}$ via

$$\vec{J}_\mathrm{c} \propto D_\mathrm{ISHE} \vec{J}_\mathrm{s} \times \vec{\sigma} \ , \tag{4.1}$$

where the direction of the spin polarization of $\vec{J}_\mathrm{s}$ is defined via the Pauli matrices $\vec{\sigma}$ [23]. The coefficient D_ISHE is the spin Hall angle, describing the efficiency of the spin-to-charge conversion process. The generated charge current density $\vec{J}_\mathrm{c}$ is perpendicular to the spin polarization direction $\vec{\sigma}$ (defined by the external magnetic field direction) as well as to the direction of the spin current $\vec{J}_\mathrm{s}$. Figure 4.1 a) shows THz transients generated from the MgO(0.5 mm)//Ta(2 nm)/$Ni_{80}Fe_{20}$(2 nm)/Pt(2 nm) bilayer in a transmission configuration shown in Fig. 3.1 a), where the pump beam was incident either from the substrate side (offset curves at y= 1500) or from the metal side (curves without offset). At each illumination condition, two curves with the external magnetic field pointing in opposite directions were measured. Comparing the THz transients obtained under illumination from the two different sample sides, one observes a flip of the THz polarity when the magnetic field direction is kept constant. The origin of the opposite polarities becomes clear looking at Fig. 4.2, which shows the direction of the spin current under the 180° rotation of the sample. The direction of the spin current $\vec{J}_\mathrm{s}$ is flipped when the sample is turned, such that the direction of the charge current $\vec{J}_\mathrm{c}$ flips according to equation 4.1. In the case of illumination from the substrate side, the laser pulse first passes through the MgO substrate with a thickness of 0.5 mm,

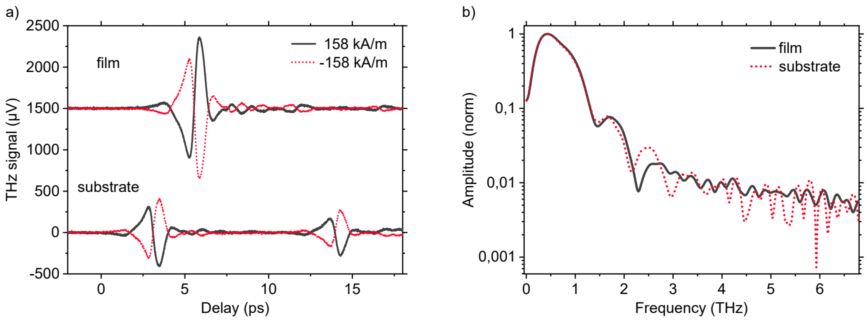

Fig. 4.1: a) THz transients for $Ni_{80}Fe_{20}$/Pt bilayers illuminated from the metal film side (top) and the substrate side (bottom) curves. At each illumination direction two curves are measured with the in-plane magnetic field of 158 kA/m pointing in opposite directions. b) FFT power spectra from the transients on the left for the illumination from both the substrate and the film side, respectively. The maximum amplitude is at 0.43 THz with a 3dB-cutoff extending up to 0.93 THz.

which leads to the fact that part of the laser pulse is absorbed and the resulting THz amplitude is lower with respect to the case of illumination from the metal side, where the laser pulse travels through only 2 nm of Pt before exciting the FM layer. Because of the different refractive index of MgO at 800 nm with respect to air ($n_{\mathrm{MgO}} = 1.7$ at 800 nm) [91]) the THz pulse is slightly delayed when the illumination occurs from the substrate side. Another feature occurring in the transients under illumination

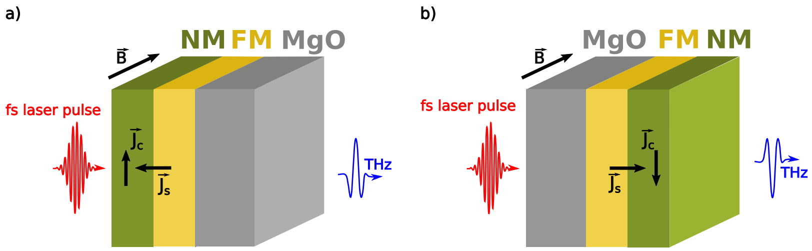

Fig. 4.2: a) Configuration for THz emission via the inverse spin Hall effect under the illumination from the metal side versus b) the configuration and current directions in the case of illumination from the substrate side.

from the substrate side is the appearance of a second THz peak, which is a copy of the first peak but with a lower intensity. This peak is a reflection of the THz transient at the MgO/air interface, which first travels in the opposite direction and gets detected only after the reflection, see Fig. 4.3. Extracting the temporal distance $\Delta t = 11.4$ ps between the peaks and using the refractive index of $n_{\mathrm{MgO},\lambda=1\,\mathrm{THz}} \approx 3$ the distance the pulse travels inside the sample corresponds to twice the thickness of the substrate, indicating that it is indeed a back reflection from the substrate/air interface $s = (c_0/n) \cdot t = 1.1\,\mathrm{mm}$. The power dependence of the THz peak amplitude

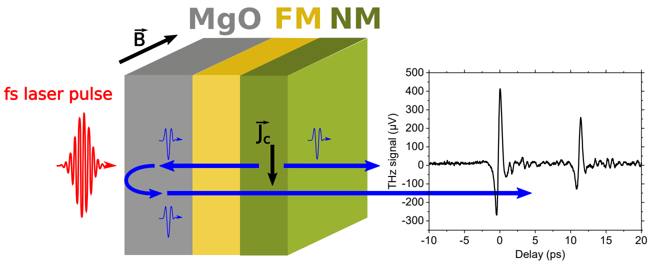

Fig. 4.3: Under the illumination from the substrate the measured THz signal shows two peaks. The peak that arrives directly at the detector and a second one, which is emitted into the opposite direction and is detected after undergoing a reflection at the substrate/air interface.

in the $Ni_{80}Fe_{20}$/Pt bilayers is shown in Fig. 4.4 a). The THz peak amplitude shows a linear behavior versus the power of the pump beam incident on the sample. Another

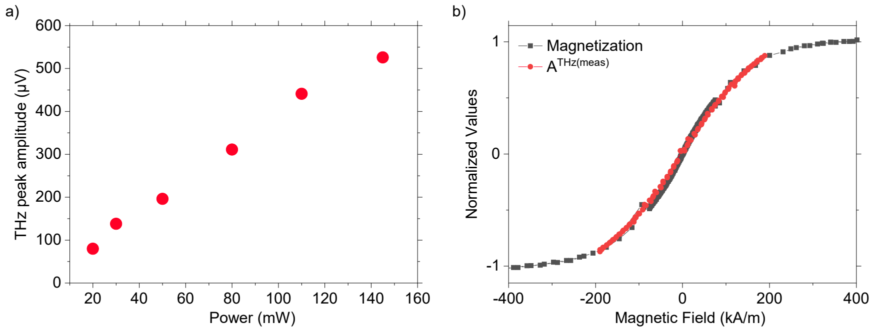

Fig. 4.4: a) Power dependence of the THz peak amplitude in $Ni_{80}Fe_{20}$/Pt bilayers, where the THz generation mechanism is the inverse Spin Hall effect. b) Comparison of the THz transient amplitude measured at different external magnetic field values between -400 kA/m and +400 kA/m and the magnetization inside the sample measured with a VSM-SQUID.

important property of the THz signal generated by the inverse spin Hall effect is the dependence on the magnetic field. From equation 4.1 we have seen that the direction of $\vec{J_c}$ is perpendicular to $\vec{J_s}$, as well as to the direction of the spin polarization inside the FM layer. This means that similarly to the polarity flip under the 180° rotation of the sample one expects the THz polarity to flip under the the reversal of the magnetic field direction. Figure 4.1 a) shows the THz signal in $Ni_{80}Fe_{20}$/Pt bilayers with a magnetic field applied in the in-plane y-direction of the sample, first in the positive direction (grey curve), and with a reversed field direction pointing in the negative y-direction (red, dotted curve). The expected flip of the THz polarity is clearly visible and confirms the origin of the THz generation to be the inverse spin Hall effect. In the next step the magnetic field was varied in smaller steps and the THz transients were measured at intermediate field values between -200 kA/m and +200 kA/m. The extracted THz transient amplitudes A^{THz} are shown in Fig. 4.4 b) (red) together with the magnetization values measured with the VSM-SQUID (grey). All values are normalized to the saturation magnetization which was not reachable with the magnetic coils used in the THz experiment. The values were hence scaled according to the value at the same magnetic field in the SQUID measurement. The values of A^{THz} follow the same dependency as the magnetization values obtained by the SQUID and the THz radiation hence closely follows the magnetization of the FM in the FM/NM heterostructure. One of the main mechanisms responsible for

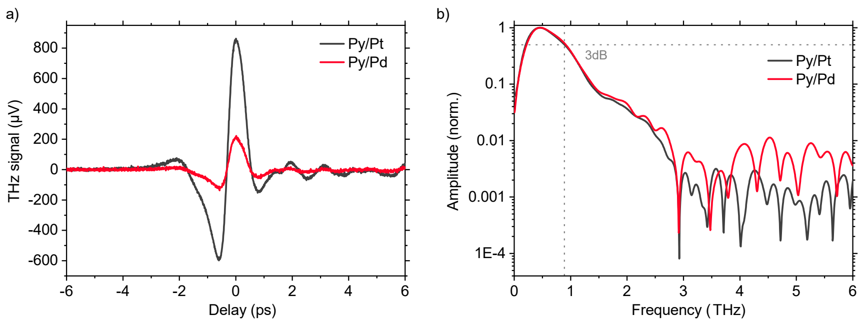

Fig. 4.5: a) THz transients generated from $Ni_{80}Fe_{20}/Pt$ (grey line curve) and $Ni_{80}Fe_{20}/Pd$ (red, dotted curve) showing different transient amplitudes. b) Normalized power spectra of the transients shown in a), showing a maximal amplitude at 0.46 THz and the 3 dB cut-off at 0.89 THz for Py/Pt and 0.91 THz for Py/Pd.

the spin dependent scattering mechanisms inside the normal metal layer is the spin orbit coupling (SOC), which scales with the atomic number Z of the material as Z^4. Comparing the THz generation for $Ni_{80}Fe_{20}/Pt$ with a second sample $Ni_{80}Fe_{20}/Pd$ a difference in the amplitude is observed, see Fig. 4.5 a). The THz transient amplitude for $Ni_{80}Fe_{20}/Pt$ is larger compared to the amplitude for $Ni_{80}Fe_{20}/Pd$ by a factor of 4. In Fig. 4.5 the normalized FFT spectra are shown and one observed that the maximal spectral amplitude is 0.46 THz for both heterostructures and the cut-off frequency is 0.89 THz for Py/Pt and 0.91 THz for Py/Pd. This observation of varying amplitudes for different NM materials is in agreement with previous findings for the ISHE [12, 26]. In a study of THz emission from $Co_{20}Fe_{60}B_{20}$ capped with different NM layers, the ratio between Pd and Pt was found to be approximately a factor of 3 [26].

Chapter 5

THz generation in Heusler alloy/heavy metal bilayers

This chapter comprises the results of THz generation from bilayers that are formed of the Heusler-alloy $Co_2Fe_{0.4}Mn_{0.6}Si$ (in the following called CFMS) and non-magnetic metal cappings Pt, Ta, Cr or Al. This chapter will start with an introduction to the Heusler alloys and explain the characteristics of CFMS, followed by the results and analysis.

5.1 Heusler alloy $Co_2Fe_{0.4}Mn_{0.6}Si$

The development of new devices for spintronic applications requires materials that carry highly polarized spin currents. The class of Heusler alloys offers the possibility of tuning the electronic structure in a way that makes it possible to create materials that show various characteristics ranging from half-metallic ferromagnets [92, 93] over-compensated ferrimagnets [94] to superconductors [95]. This broad spectrum of material characteristics makes the Heusler alloys a promising candidate for many applications in the field of spintronics. Especially the Co-based Heusler alloys have received strong attention for device application, for example, as electrodes in magnetic tunnel junctions (MTJ) or giant magnetoresistance (GMR) devices, because of their high Curie temperature [96, 97] as well as ferromagnetism and half metallicity, particularly in the case of Co_2-based alloys [98, 99, 100, 101, 102]. The Heusler alloys can be divided into the class of full Heusler alloys and the half Heusler alloys, the former showing a structure of A_2BC, where A and B stand for transition metals and C stands for an element from the III to V group of elements in the periodic table, shown in Fig. 5.1 c) and the latter with an ABC structure, shown in fig. 5.1 b). The first Heusler alloy observed was Cu_2MnAl, which surprisingly shows ferromagnetism, although none of the constituents themselves show ferromagnetic properties. The fundamental crystal structure is a ZnS-type structure shown in Fig. 5.1 a), where the

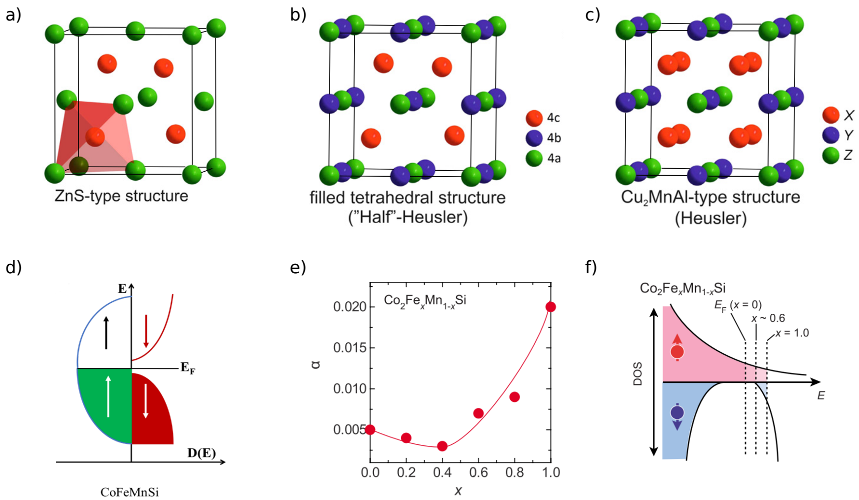

Fig. 5.1: a) ZnS-type crystal structure forming the basis of the Heusler alloy crystal structure. b) Filling the octahedral sites of the ZnS-structure in a) leads to the structure for the half Heusler alloys. c) Cu_2MnAl-type structure of the full Heusler alloy. (a)-c) taken from reference [103] d) Half-metallic band structure for CoFeMnSi, with one spin channel shown a gap in the density of states at the Fermi level. (Taken from reference [104]) e) Damping constant α with varying content of Fe and Mn in $Co_2Fe_xMn_{1-x}Si$, showing a minimum at $x = 0.4$. f) The Fermi level position for $Co_2Fe_xMn_{1-x}Si$ depends on x and can lead to the vanishing of the half-metallic character in CFMS. (e) and f) from reference [93])

occupancy of lattice sites changes depending on the elemental configuration, yielding the structures shown in b) and c). The $Co_2Fe_{0.4}Mn_{0.6}Si$ belongs to the full Heusler alloys and has a half-metallic band structure, shown in Fig. 5.1 d). The metallic characteristic of the DOS is preserved for only one spin channel, while the DOS for the other spin channel vanishes around the Fermi level. This leads to a spin polarization P at the Fermi level

$$P = \frac{D_\uparrow(E_\mathrm{F}) - D_\downarrow(E_\mathrm{F})}{D_\uparrow(E_\mathrm{F}) + D_\downarrow(E_\mathrm{F})} , \tag{5.1}$$

which, in the ideal case, is 100% for half metals and is expected to result in substantial enhancement of the spin current polarization. However, under experimental conditions, structural disorder in the $L2_1$-structure was found to be responsible for a lower spin polarization at the Fermi level [105]. The magnetic moment in Co_2 Heusler alloys can be evaluated using the Slater-Pauling rule, which draws a relation between the number of valence electrons N_v and the magnetic moment m of the compound

$$m = N_\mathrm{v} - 24 . \tag{5.2}$$

In the case of $Co_2Fe_{0.4}Mn_{0.6}Si$, this leads to a magnetic moment of $m = 5.4\mu_B$ [28]. Furthermore, $Co_2Fe_{0.4}Mn_{0.6}Si$ shows a low magnetic damping constant α [93], which is a crucial parameter for many spintronic devices [106]. Tuning the electronic structure of $Co_2Fe_xMn_{1-x}Si$ by changing the amount of Fe and Mn, the damping can be tuned and takes a minimum value at $x = 0.4$, see Fig. 5.1 e). The composition tuning also showed that the half-metallic character can vanish under certain conditions (see Fig. 5.1 f)) that lower the half-metallic energy gap or shift the Fermi level, e.g., through strain or imperfect $L2_1$-ordering [93]. With the help of the inverse spin Hall effect and spin pumping, it was previously shown that $Co_2Fe_{0.4}Mn_{0.6}Si$/Pt double layers show a large interface transparency of 84 % [107], which makes it an interesting material for interfacial spin current applications.
The following section will show results obtained from $Co_2Fe_{0.4}Mn_{0.6}Si$ Heusler alloy/NM heterostructures with either a Pt, Ta, Al, or Cr NM layer. All the samples have the same layout
MgO//$Co_2Fe_{0.4}Mn_{0.6}Si$(20 nm)/NM(2 nm) and were prepared in the group of Koki Takahashi (Institute for Materials Research, Tohoku University, Sendai, Japan). The preparation was done in an ultra-high-vacuum magnetron sputtering system with a base pressure of about 2×10^{-7} Pa on a MgO(001) substrate. The MgO substrates are single crystals, which were heated to 700°C before the deposition of $Co_2Fe_{0.4}Mn_{0.6}Si$ to clean the surface of the substrate. The deposition of $Co_2Fe_{0.4}Mn_{0.6}Si$ and the NM layer was performed at a constant temperature of 500°C.

5.2 THz transients from $Co_2Fe_{0.4}Mn_{0.6}Si$/NM bilayers

Figure 5.2 compiles the time- (a) and frequency-resolved (b) THz transients from the four different CFMS/NM bilayers. Similarly to the THz transients in section 4, we observe different THz transient amplitudes for the four distinct materials contained in the bilayers. The highest THz transient amplitude is observed for CFMS/Pt, described by the left (red) scale in Fig. 5.2 (a). It is followed by the CFMS/Ta, CFMS/Cr, and CFMS/Al bilayers, represented by the scale on the right side (black). The in-plane magnetic field applied to the bilayers as shown in Fig. 4.2 a) was 16 kA/m, and the laser fluence incident on the sample was 6 μJ/cm^2 with a spot diameter of 150 μm. The spectra in Fig. 5.2 (b) show the maximum intensity for all four bilayers at 0.69 THz with a -3 dB cut-off extending above 1 THz with 1.07 THz for Pt, 1.00 THz for Ta, 1.04 THz for Cr and 1.14 THz for Al. To figure out the origin of the generated THz radiation, we measured the magnetic field dependence. Reversing the direction of the magnetic field shows an inverted THz transient polarity from the CFMS/NM bilayers; see fig. 5.3 (a). The flip of the THz transient is an indication that the signal is produced via the inverse Spin Hall effect. As can be seen from equation 4.1 in chapter 4, a reversed direction of the magnetic field leads to a change of the direction

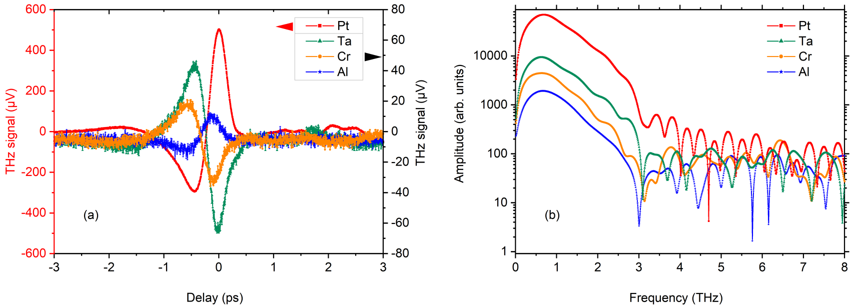

Fig. 5.2: (a) Measured THz transients for CFMS/Pt (left scale) and CFMS/Ta, CFMS/Cr, and CFMS/Al (right scale). (b) Power spectra of the THz transients shown in (a) calculated by fast Fourier transformation (FFT).

of the generated spin current, which becomes evident by a flip of the polarity of the generated THz transient. Varying the laser fluence at the sample position, it can be observed that the THz transient intensity is proportional to the laser fluence. The results are shown for CFMS/Pt in Fig. 5.3 (b). These characteristics of the THz generation are in agreement with the previous results shown for $Ni_{80}Fe_{20}$/NM bilayers in section 4 and indicate that the origin of the THz transients from the CFMS/NM bilayers is the inverse spin Hall effect. The spin Hall effect, and also its inverse process,

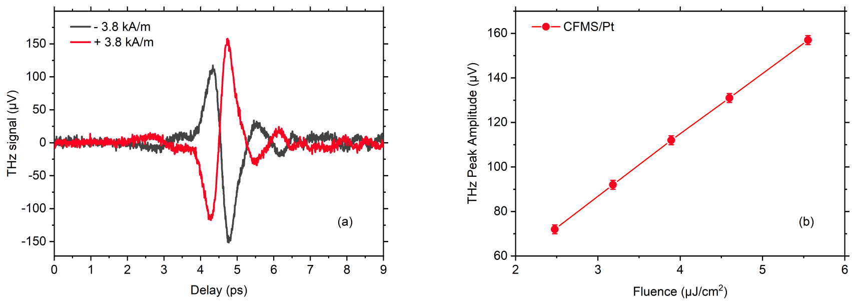

Fig. 5.3: (a) THz transients for CFMS/Pt with opposite in-plane field directions, leading to a reversed THz polarity. (b) Fluence dependence of THz transient peak amplitude for CFMS/Pt. The beam diameter impinging on the sample was 300 μm.

is characterized by the spin Hall angle D_{ISHE} (see equation 4.1), a material-specific coefficient, characterizing the spin-to-charge conversion efficiency. The THz transients in fig. 5.2 a) show different amplitudes depending on the NM material and an inverted signal for Cr and Ta, compared to Pt and Al. The different THz transient amplitudes are in agreement with the spin Hall angles that were observed previously, see e.g. [12, 108], where an opposite sign is observed for the spin Hall angle in Ta and Cr. It was

NM	S [mm^2]	$A^{\mathrm{THz(meas)}}$ (μV)	$A^{\mathrm{THz(norm)}}$	$Z^{4\mathrm{(norm)}}$
Pt	12.2	501 $\pm$ 2	1	1
Ta	22.3	63 $\pm$ 2	0.108	0.77
Cr	33.4	33 $\pm$ 2	0.052	0.009
Al	25.2	10 $\pm$ 2	0.035	7.72 $\times 10^{-4}$

Table 5.1: First row shows the size of the measured sample pieces S in mm^2. The second and third rows contain the measured THz amplitudes $A^{\mathrm{THz(meas)}}$ and the normalized amplitudes $A^{\mathrm{THz(norm)}}$ to the THz transient amplitude for platinum A^{Pt}. The fourth row shows the normalized Z^4 values for the different NM materials normalized to the Pt value.

shown in an extensive study by Wang et al. that the spin Hall angle is correlated with the spin-orbit coupling of the NM material, which scales with the atomic number Z as Z^4 [109]. Consequently, a substantially higher THz transient amplitude is expected for Pt compared to Al. This is indeed observed, as we show in Fig. 5.2 a). The inverted THz amplitude of Cr and Ta compared to Pt was also observed by Seifert et al. [26] and is related to the spin polarization at the Fermi level, see equation 2.37. Depending on the filling of the 3d shell, the spin Hall conductivity changes its sign, as can be seen in Fig. 2.10 a) for the 4d and 5d transition metals. The normalized THz transient amplitudes $A^{\mathrm{THz(norm)}}$ and normalized $Z^{4\mathrm{(norm)}}$ values, proportional to the spin-orbit coupling, (both are normalized to the Pt value) are plotted in Fig. 5.4 and show a close agreement for the Cr and Al amplitudes. However, for the Ta capping, a substantially lower THz transient amplitude is observed than is expected based on the Z^4-scaling. The Z^4 dependence suggests the THz transient amplitude for $Co_2Fe_{0.4}Mn_{0.6}Si$/Ta to be approximately 80% of the CFMS/Pt value. However, the observed value is approximately 10% when considering exclusively the spin-orbit coupling as a decisive factor for the spin-to-charge conversion efficiency. The next chapters will investigate the substantial difference in the THz transient amplitude for CFMS/Ta and examine the effects impacting the efficiency of the spin to charge conversion process.

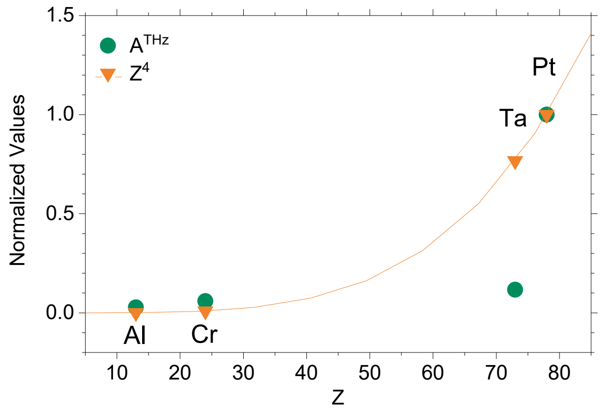

Fig. 5.4: Comparison of the measured THz transient amplitudes (green) and the Z^4 values (yellow) for the SOC for Pt, Ta, Al, and Cr, all normalized to the Pt value.

5.2.1 Magnetic field dependence

In the next step, the dependence of the THz transient amplitudes on the magnetic field was investigated. As seen in Fig. 5.3 (a), reversing the magnetic field leads to a flip of the THz transient polarity. To figure out how the amplitude reverses its polarity, THz transients were measured at various intermediate field steps. The extracted THz peak amplitudes A^{THz} (color lines and points) of the transients for all CFMS/NM bilayers are shown in Fig. 5.5. Comparing the magnetic field dependent THz transient amplitudes with the magnetization of the full sample piece, measured with a VSM-SQUID device, it becomes clear that the THz transient amplitude follows the magnetization of the sample, showing almost exactly the same hysteretic behavior. This is valid for all investigated NM materials. Taking a look at the transition region of the hysteresis one notes a sharper transition between two opposite THz polarities as compared to the reversal between the two antiparallel magnetization orientations measured by the VSM. We attribute the behavior to the geometry and difference of the probed sample volume in the two techniques. The size of the sample pieces investigated with the VSM-SQUID technique are listed in Table 5.1 and lie in the range of 12-25 mm^2, hence two orders of magnitude larger than the size of the illuminated area during the THz measurements, where the 1/e^2 beam waist was about 300 μm. During the VSM measurements, the magnetization is measured over the full sample piece and hence, averaged over all domains and domain walls, as well as all inhomogeneities of the microstructure including, e.g. crystal or magnetic defects and the roughness of the film surface. Of particular importance are the sample edges since the domain walls can be pinned there and consequently lead to a smoothing of the magnetization reversal.

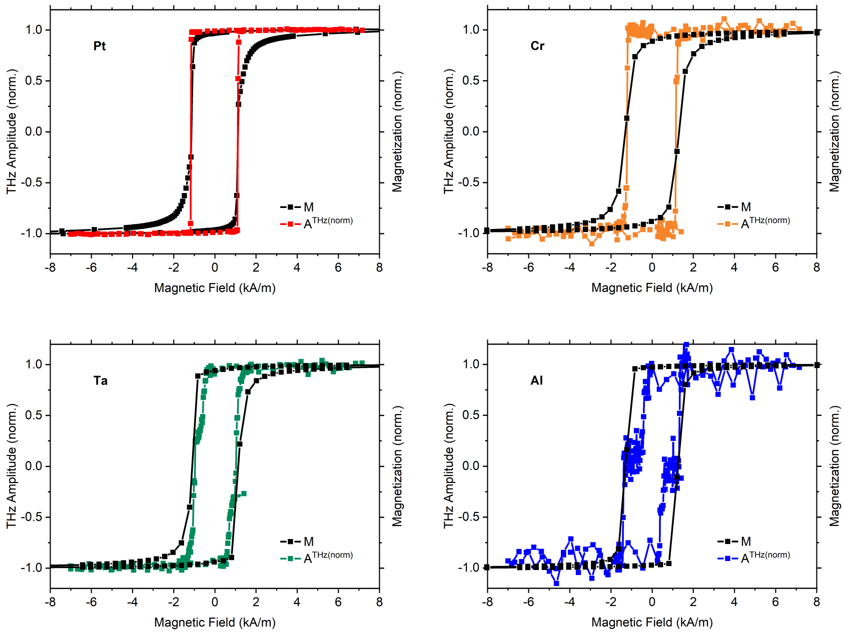

Fig. 5.5: Normalized peak amplitudes of the THz transients under varying in-plane magnetic field from -8 kA/m to 8 kA/m compared with the normalized magnetization of the full sample pieces measured via MPMS-SQUID.

The laser beam was positioned approximately in the middle of the sample such that the THz measurements do not include the edges of the samples, but rather probe a locally small sample volume. This leads to the fact that the effect of pinning centers and defects will be less pronounced and result in a sharper transition of the THz amplitude from one to the other polarity compared to the magnetization reversal in the SQUID measurement, as seen in Fig. 5.5. One can employ the effect to investigate the effects of magnetic in-plane anisotropy, as can be seen in Fig. 5.6. We measured the magnetization with a VSM technique (Fig. 5.6 (b)) at 0° and rotated by 45°, as well as the THz transient peak amplitudes at 0° and 45° for varying magnetic field (Fig. 5.6(a)) and observe in both cases an easy-axis loop at 0° and the behavior of an intermediate hard axis loop at 45°.

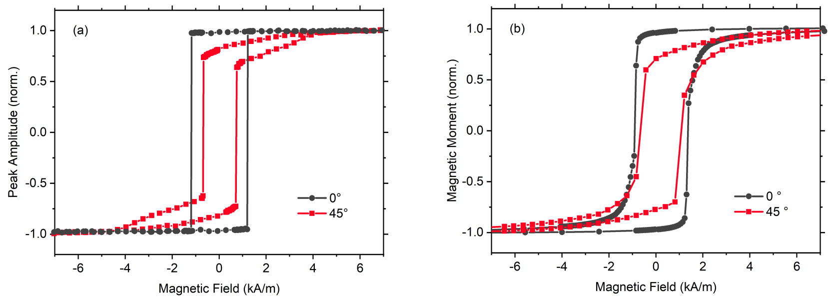

Fig. 5.6: (a) Normalized THz peak amplitude versus the in-plane magnetic field for 0° and 45°. (b) Normalized magnetization of the sample measured by VSM at an angle of 0° and 45°.

5.2.2 Temperature dependence

Additionally, we measured THz transients from CFMS/Pt Heusler alloy at temperatures ranging from 300 K down to 100 K. The sample was placed inside a flow cryostat so that the samples could be cooled down to around 100 K. Below 80 K condensation on the cryostat windows was observed, and the THz radiation was mostly absorbed, leading to a much lower THz signal. Down to 100 K no such effect was observed. During this measurement, the waiting time for each temperature to stabilize was 30 minutes to ensure that the sample was at the targeted temperature. The measured THz transients starting from 300 K and ending up at 100 K are compiled in Fig. 5.7 a) and the extracted peak amplitudes versus the temperature are shown as the inset. An

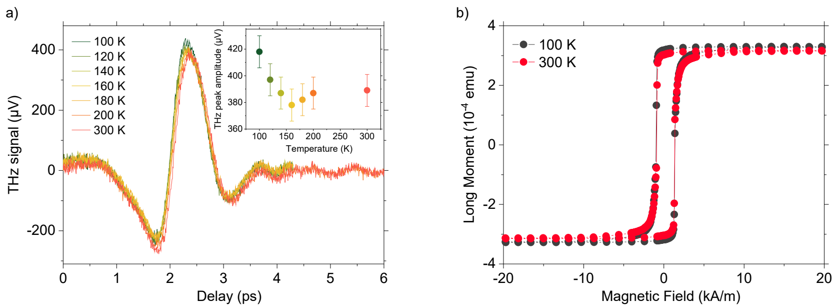

Fig. 5.7: a) Temperature-dependent THz transients for CFMS/Pt from 300 K down to 100 K. The inset shows extracted THz peak amplitude of the measured THz transients. b) shows the hysteresis curves measured by the VSM at 300 K (red) and at 100 K (grey).

increase of the THz transient amplitude of (7.5±4.4)% is observed when lowering the temperature. This is in agreement with the increase of magnetization of (4.1±0.1)% measured from VSM measurements, as can be seen in Fig. 5.7 b) comparing the saturation magnetization at 300 K and at 100 K. Figure 5.8 shows the comparison of the hysteresis measured by the VSM and the THz setup at 300 K in b) and at 100 K in a). The THz radiation is following the sample magnetization at 100 K in the same way as in the case of 300 K.

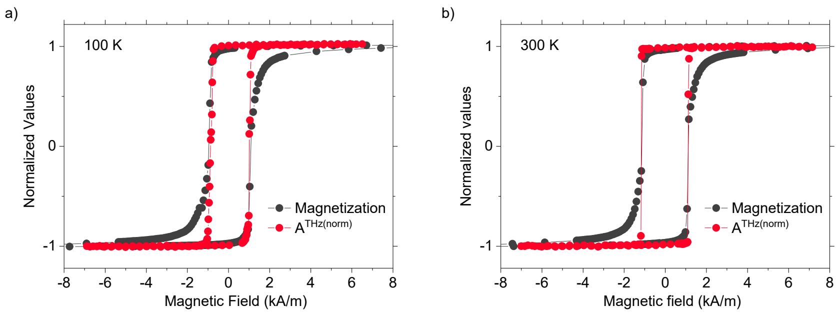

Fig. 5.8: Comparison of the normalized THz amplitude $A^{\mathrm{THz(norm)}}$ versus the in-plane magnetic field with the magnetization of the sample measured by the SQUID at (a) 100 K and (b) 300 K.

5.3 Ferromagnetic resonance

Besides optical excitation with fs-laser pulses, the generation of a spin current between FM/NM heterostructures can be achieved using a ferromagnetic resonance (FMR)-spin pumping experiment. This technique allows us to investigate the interface transparency for the spin current between the two layers, which is affected by a range of effects influencing the interface quality. These effects include, e.g., mismatch in the electronic structure, the roughness and material interdiffusion, which is having an impact on the sharpness of the interface. The interface transparency can be described by the ratio of spin-polarized electrons passing the FM/NM interface to the amount of all the electrons reaching the interface. The interface transparency for CFMS/Pt was previously investigated by Singh et al. and found to be 84%, resulting in a high spin mixing conductance $g^{\uparrow\downarrow}$ [29], which characterizes the efficiency of the interfacial spin transport. For the investigation of the interface properties of the different sample systems, the sample is placed on top of the coplanar waveguide as described in section 3.3 and schematically shown in Figure 3.3. The precessional motion of the 3d electrons caused by the applied rf field leads to a continuous pumping of spin angular momentum across the interface. A vector network analyzer then measures the change of the rf signal passing along the transmission line, S_{12}. For this, the frequency of the rf field is swept from 0.5 to 20 GHz at various static magnetic fields. At the resonance frequency, the absorption of the rf signal in the sample is maximal, leading to an absorption peak in the S_{12} parameter. Figure 5.9 compiles the frequency sweeps for CFMS/Pt at dif-

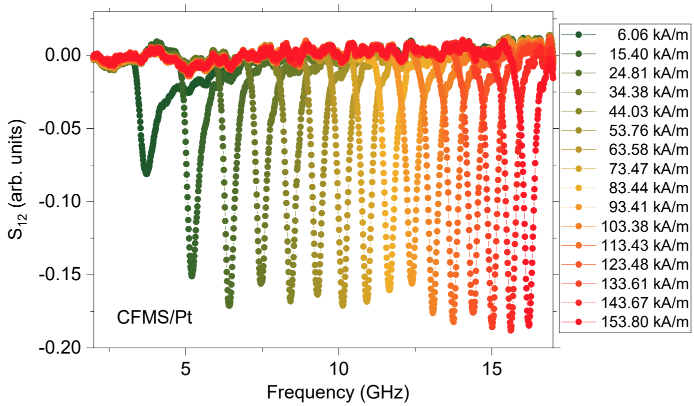

Fig. 5.9: Frequency sweeps up to 17 GHz of the absorption of the rf signal after transmission of the CPW waveguide, characterized by the S_{12} parameter, at various static magnetic field steps ranging from 6 kA/m to 150 kA/m.

ferent static magnetic fields ranging from 6 kA/m to 150 kA/m. At every magnetic field, an absorption dip is clearly visible, and the resonance frequency is increasing for an increasing magnetic field intensity. Additional graphs for all CFMS/NM samples can be found in the appendix A.1. The increase of the resonance frequency f_{res} with the in-plane static magnetic field H is described by

$$f_{\mathrm{res}} = \frac{\gamma}{2\pi}\sqrt{(H_{\mathrm{K}}+H)(H_{\mathrm{K}}+H+4\pi M_{\mathrm{eff}})} \tag{5.3}$$

for an in-plane magnetized thin film sample, where γ is the gyromagnetic ratio, H_{K} is the anisotropy field and $4\pi M_{\mathrm{eff}}$ is the effective magnetization of the sample [45]. Extracting the resonance frequencies versus the magnetic field, one can use equation 5.3 for a fitting of the experimental data, which are shown in the inset of Fig. 5.10. This allows us to extract also the effective magnetization $4\pi M_{\mathrm{eff}}$ of the sample systems, which are compiled in table 5.2. Furthermore one can extract the frequency linewidths Δf of the resonance peaks and use the derivative $\partial f_{\mathrm{res}}/\partial H$ to convert them into field linewidths ΔH, following the procedure in reference [110].

$$\Delta H = \left(\frac{\partial f_{\mathrm{res}}(H)}{\partial H}\right)^{-1}\cdot \Delta f \; . \tag{5.4}$$

The field linewidths show a linear increase in the resonance frequency, which is expressed by the equation

$$\Delta H = \Delta H_0 + \frac{4\pi\alpha_{\mathrm{eff}} f_{\mathrm{res}}}{\gamma} \; , \tag{5.5}$$

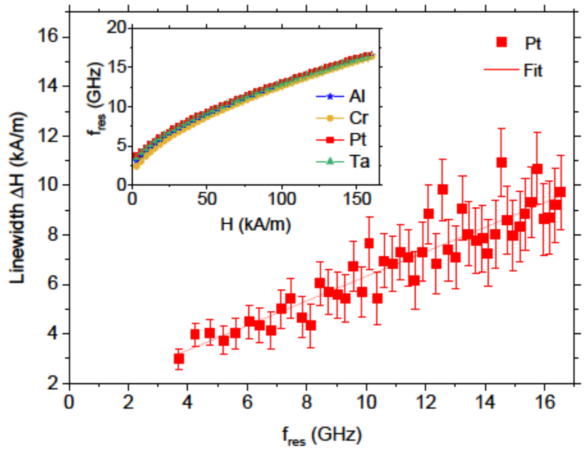

Fig. 5.10: Field linewidths converted via equation 5.4 versus the resonance frequency $f_{\rm res}$ and linear fit for CFMS/Pt. The inset shows the resonance frequencies versus the magnetic field, which is described by equation 5.3 for all four CFMS/NM heterostructures. Additional linewidth fits can be found in the appendix A.2.

with the inhomogeneous broadening ΔH_0 and the effective damping constant $\alpha_{\rm eff}$ [29, 110]. The inhomogeneous broadening ΔH_0 is related to the degree of magnetic and structural inhomogeneity of the sample, and the damping constant $\alpha_{\rm eff}$ can be extracted from the fitting with equation 5.5. In the case of a bare CFMS film, the damping constant is the intrinsic damping constant α_0. However, in the presence of an adjacent nonmagnetic layer, the intrinsic damping constant is enhanced by an additional damping component $\Delta\alpha$, which arises due to the spin pumping $\alpha_{\rm eff} = \alpha_0 + \Delta\alpha$. The extracted damping values are compiled in table 5.2. With the help of the damping term originating from the spin pumping, we are able to extract the effective spin mixing conductance $g_{\rm eff}^{\uparrow\downarrow}$ using

$$g_{\rm eff}^{\uparrow\downarrow} = \frac{4\pi M_s t_{\rm CFMS}}{g\mu_{\rm B}}\Delta\alpha \ , \tag{5.6}$$

where $t_{\rm CFMS}$ is the thickness of the CFMS layer. The values for the intrinsic damping constant α_0 were taken from reference [111], where CFMS samples were grown by co-sputtering of CoMnSi and CoFeSi targets and investigated by members of the group providing the samples for this thesis, assuming very similar intrinsic damping in both cases. It is important to note that the effective spin mixing conductance calculated from the FMR-spin pumping experiments includes a variety of effects that can lower the efficiency of interfacial transport e.g. spin-flip processes at the interface, as well as backflow of spins, due to reflection at the NM/air interface and hence depends on the specific sample properties. We included the extracted values for the $g_{\rm eff}^{\uparrow\downarrow}$ in table

NM	$4\pi M_S$ (kA/m)	α_{eff}	$g_{eff}^{\uparrow\downarrow}$ (10^{18}m^{-2})	λ_{sf} (nm)	$t_{FM/NM}$ (nm)
Al	1180± 2	0.0051 ± 0.0005	2.8 ± 0.5	490 [112]	0.3
Cr	1182 ± 3	0.0059 ± 0.0003	3.7 ± 0.5	13.3 [113]	-
Ta	1166 ± 1	0.0065 ± 0.0004	3.9 ± 0.5	1.9 [109]	1.2
Pt	1191± 1	0.0071 ± 0.0004	5.2 ± 0.7	7.3 [109]	2.2

Table 5.2: Effective saturation magnetization values $4\pi M_S$ extracted from FMR measurements, the calculated effective damping constants α_{eff}, effective spin mixing conductances $g_{eff}^{\uparrow\downarrow}$ and the spin diffusion lengths of the NM material taken from the included references.

5.2.

5.4 Discussion

Figure 5.4 shows the THz transient amplitudes $A^{THz(meas)}$ and the Z^4 dependence for the spin-orbit coupling, normalized to the Pt values. We observed that even though the results show an agreement in the case of CFMS/Al and CFMS/Cr, a substantial discrepancy is observed in the case of the THz transient amplitude from the CFMS/Ta emitter. The measured amplitude $A^{THz(meas,Ta)}$ is approximately 12% of the $A^{THz(meas,Pt)}$ despite an expectation of $\approx$ 80% of $A^{THz(meas,Pt)}$. In addition to the THz transient amplitudes and the Z^4 dependence, Fig. 5.11 illustrates also the $g_{eff}^{\uparrow\downarrow}$ values (blue diamonds) extracted from the FMR measurements in the previous section. The CFMS/Ta sample not only shows a large Z^4 value but a large spin mixing conductance $g_{eff}^{\uparrow\downarrow}$ as well. To break down this discrepancy we took the spin diffusion lengths λ_{sf} of the NM materials and the thicknesses of the bilayers $t_{FM/NM}$ into account. The values for λ_{sf} were taken from literature and are summarized in table 5.2. Comparing the values for λ_{sf} we note that the spin diffusion length in Ta in the shortest of the sample systems and even smaller than the nominal thickness of the Ta layer. For the thickness of the bilayers it was taken into account that the effective thickness, where the ISHE is taking place, is reduced due to partly oxidized NM layers. X-ray reflectivity (XRR) measurements on the samples were performed in the group of Koki Takanashi (Institute for Materials Research, Tohoku University, Sendai, Japan) and reveal that especially for Ta and Al, the effective thickness is substantially reduced by around 2/3, see table 5.11. The XRR-measurements are shown in A.3 in the appendix. The Cr layer of the CFMS/Cr is also likely to be oxidized, however, no oscillation could be observed in the XRR trace. Previous investigations of the thickness dependence of the ISHE have shown that the ISHE shows a maximum efficiency around 2.7 nm in Ta, and sharply drops for smaller thicknesses [114, 115]. The 2.7 nm thickness equals the spin diffusion length in these references and it reveals that the thickness of the NM layer is an essential parameter to take into account. Consequently, three parameters were identified, influencing the efficiency of THz radiation from the CFMS/NM bilayers: the effective spin mixing conductance $g_{\mathrm{eff}}^{\uparrow\downarrow}$, taking into account the spin transmission efficiency of the FM/NM interface, the spin diffusion lengths λ_{sf} of the NM layer and the effective thickness of the full (non-oxidized) bilayer $t_{\mathrm{FM/NM}}$. Taking this into account the Z^4 values were weighted by

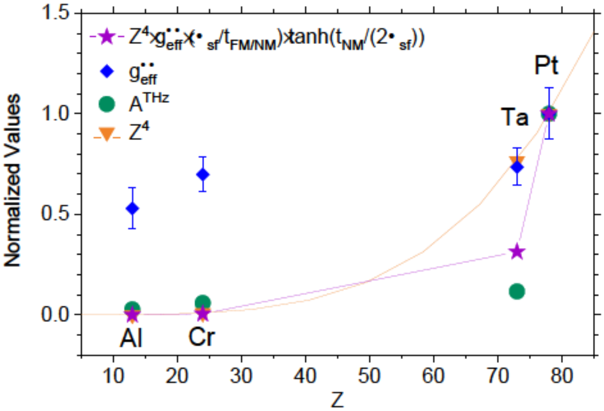

Fig. 5.11: Comparison of THz transient amplitudes normalized to the Pt value (green) and the Z^4 values (yellow) for the SOC, also normalized to the Pt value.

a factor $g_{\mathrm{eff}}^{\uparrow\downarrow} \cdot (\lambda_{\mathrm{sf}}/t_{\mathrm{FM/NM}})\tanh[t_{\mathrm{FM/NM}}/(2\lambda_{\mathrm{sf}})]$, see reference [116]. The results are shown in Fig. 5.11. As in Fig. 5.4, the THz transient amplitudes A^{THz} and the Z^4 scaling are shown. In addition the effective spin mixing conductance and the weighted Z^4 dependence are displayed. All values shown in the figure are normalized to the Pt value. It is apparent that the weighted Z^4-value for Ta is in much closer agreement with the experimentally observed THz transient amplitude than the pure Z^4 dependence. However, a small discrepancy is remaining and it suggests the influence of additional effects and parameters influencing the efficiency of THz generation from FM/NM bilayers.

Another interesting observation was made for the CFMS/Al bilayer. The SOC value for Al points out a value of 0.077% compared to the Pt value, see fourth row of table 5.1, however $\mathrm{A}^{\mathrm{THz(Al)}}$, shown in the second row, is $\approx$ 3%, which is two orders of magnitude larger than expected from the Z^4 scaling. Using x-ray absorption near-edge structure (XANES) and x-ray circular magnetic dichroism (XMCD) the magnetic and structural properties of the interfaces were studied to investigate the remarkably larger THz transient amplitude of the CFMS/Al bilayer. The measurements were performed by Carolin Schmitz-Antoniak at BESSY II [117, 118], in the experimental "ALICE" chamber of the PM3 beamline [119, 120] and are shown in Fig. 5.12. The XANES spectrum taken at the Mn absorption edge shows several side

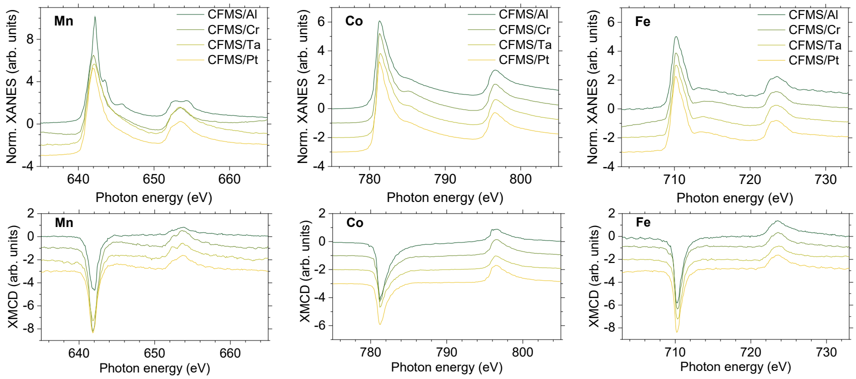

Fig. 5.12: Element-selective investigations of $Co_2Fe_{0.4}Mn_{0.6}Si$/NM bilayers with NM standing for Al, Cr, Ta and Pt (dark to light color line) using XANES (shown in top row) and XMCD (spectra shown in the bottom row).

peaks in the case of CFMS/Al bilayer. The side peaks are not present for the other three bilayers and point to a more localized condition of the Mn *3d* electrons in the $Co_2Fe_{0.4}Mn_{0.6}Si$ caused by interdiffusion of Al atoms into the CFMS interface region. The influence of interdiffusion in FM/NM interface regions on the efficiency of THz radiation was investigated previously in references [78, 121]. It was shown that the influence of interfacial effects on the spin to charge conversion in NM elements is up to 20% of the spin to charge conversion by the ISHE in the bulk of reference samples containing Pt. The origin of the interfacial contribution can be ascribed to skew scattering of the spin polarized electrons traversing the interface at impurities present in the interface region. This is confirmed by the influence of the growth direction, or rather the assignment of host and impurity atom, as a different sign for the host being the FM and the impurity the NM material and vice versa is observed. Even though the overall spin current density entering the Al layer is reduced and hence lowers the bulk ISHE, the THz amplitude is two orders of magnitude higher than expected due to the interfacial skew scattering.

Chapter 6

THz generation in topological insulator Bi_2Se_3

This chapter compiles the investigations of heterostructures consisting of topological insulator Bi_2Se_3
wedge layers. The chapter starts with an introduction to the general characteristics of topological insulators and is followed by the THz generation investigations.

6.1 Introduction to topological insulators

Topological insulators (TIs) are a fascinating class of materials that possess a unique combination of conducting and insulating properties, which fundamentally distinguishes them from topologically trivial materials. In the bulk, TIs behave as conventional insulators. The surface states, however, are conductive and insensitive to backscattering because they are protected by time-reversal symmetry (TRS). The spin texture of the surface states shows spin momentum locking, which makes TIs interesting materials for spintronic applications [122, 123].

6.1.1 Topological concepts and the quantum Hall state

The mathematical concept of topology is often described by the example of a coffee mug being equal to a doughnut, but different from a sphere. The reason for the coffee mug being topologically equal to the doughnut is a smooth transformation, which can deform one into the other, since both obtain the same number of holes. This property is described by a topological invariant genus g, which can only take integer values, and describes the number of holes in the geometrical shape. Using this definition it becomes obvious that a doughnut is topologically distinct from a sphere, as the topological invariant would need to change from 1 to 0 [124].
The mathematical concept of topology described by a topological invariant can be transferred to the electronic band theory of solids in order to distinguish topologically

trivial and non-trivial materials. A topological invariant n for the electronic bandstructure was found by Thouless, Kohmoto, Nightingale and den Nijs (TKNN) and is called the Chern number [125]. In band theory an insulating material is characterized by a bandgap between the conduction and valence band. Similarly, also semiconductors exhibit an energy gap, but of smaller size. The two can be invariant if the Hamiltonian can be continuously altered to transfer between the two states without closing the energy gap [126].

Figure 6.1 top row shows the state of a trivial insulator, where the electrons occupy localized orbitals and do not feel the impact of the sample boundary as stated by Kohn [127]. Contrary to the state of a classic insulator, von Klitzing discovered in

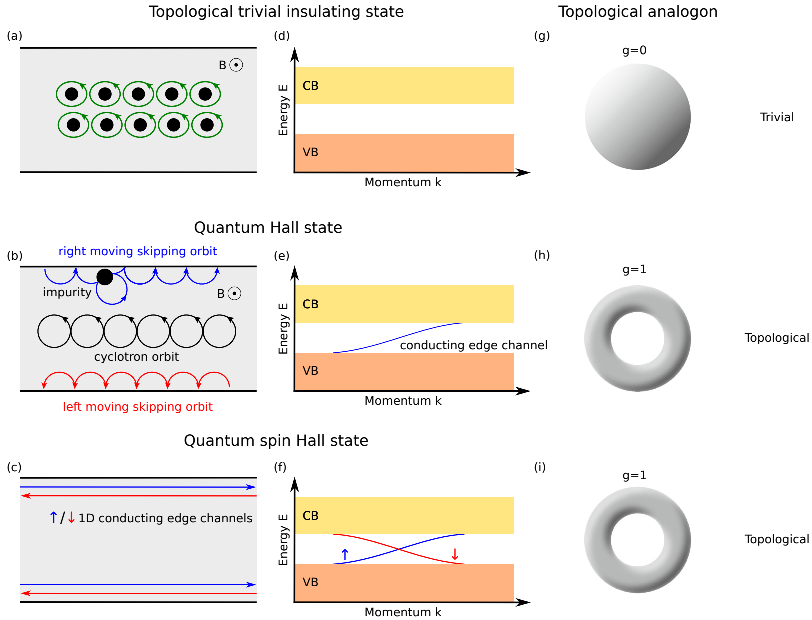

Fig. 6.1: Difference between a trivial insulator (top row), the quantum Hall state (middle row) and the quantum spin Hall state (bottom row) shown in real space in (a)-(c), the band structure (d)-(e) and with the mathematical respective topological analogon (g)-(i). Partly adapted from [128, 124]

1980 a new quantum state in which the properties of the bulk and the surface are sensitive to each other, resulting in the integer quantum Hall effect [129], see Figure 6.1 (middle row). In this case a two dimensional electron gas at low temperatures is exposed to a strong magnetic field, which forces the electrons to follow quantized circular orbits with a cycloton frequency $\omega_c = eB/m$. The energy of the electrons is quantized in degenerate Landau levels (LL) with $E_m = \ \omega_c(m+1/2)$ and the number of filled states of the Landau level is given by $N_{\mathrm{L}} = eB/h$. The LL can be considered very closely resembling the bandstructure of an insulator, taking into account that N Landau levels are filled and the energy gap is separating the highest occupied and the lowest empty LL. Applying an electric field leads to a drift of the LL, resulting in a Hall current and a Hall conductance

$$\sigma_{\mathrm{xy}} = Ne^2/h \ , \tag{6.1}$$

taking only integer values N of e^2/h, whereas the longitudinal conductance σ_{xx} vanishes. The quantized nature can be understood with the help of Laughlin's argument, where changing the flux in the center of a disk by a Hall flux quantum Φ_0 leads to an integer number of charges crossing the edges [130], described also in [124]. The motion of the bulk electrons is taking place on localized orbits, similar to the classical insulator picture, however, at the boundary 1D conducting edge channels are formed as can be seen in Figure 6.1 (b). These edge channels are unidirectional and dissipationsless [131] and usually referred to as chiral edge states. In a magnetic field, electrons located on classical circular trajectories very close to the sample boundary are bounced back due to a confining electrostatic potential. The strong magnetic field forces the electrons back onto their trajectories, resulting in movement on so-called skipping orbits along the boundary. The electrons moving in the skipping orbits at the upper boundary of the sample move in a different direction than the electrons at the lower boundary, with the moving direction defined by the direction of the magnetic field [132, 124]. Similarly the lack of backscattering for the helical edge states can be understood in the picture of skipping orbits. If the edge states encounters an impurity the electron will move around the impurity as shown in Figure 6.1 (b) [133]. The existence of the chiral edge states is strongly rooted in the properties of the bulk material, which is expressed by the *bulk boundary correspondence*. Without the topological nature of the quantum Hall state in the bulk, the edge states would not show their specific properties. At the sample boundary or at the interface the topological invariant is changing e.g. from $n = 1$ (topologically non-trivial) to $n = 0$ (topologically trivial). At these points, where the topological nature is changing, the band gap needs to close and open up again. This in turn, leads to the existence of low energy states in the bulk gap, close to the point of the Fermi level crossing [126]. The connection between the gap closing, when the topological character is changing will be explained in the upcoming paragraphs.

6.1.2 Quantum spin Hall state and $_2$ invariant

The presence of the quantum spin Hall state (QSHS) was theoretically proposed first in graphene by Kane and Mele in 2005 [134]. In this system the spin-orbit coupling plays an important role to generate the topological state [126], however, the SOC in graphene is rather small, and therefore further predictions for a CdTe/HgTe/CdTe quantum well were made by Bernevig, Hughes and Zhang [135] and realized by König et al. in 2007 [136]. Compared to the QH state the QSH state does not need an external magnetic field and thus preserves TRS. The QSH state can be viewed as two copies of the QH state, where the two edge states form a Kramers pair that is protected by TRS and spin up and spin down electrons in the helical edge states are moving in opposite directions, see Figure 6.1 (c). The preserved TRS protects the helical edge states from backscattering, due to a destructive interference of all possible paths taken by the backscattered electrons. When encountering an impurity an electron can move in the clockwise or counterclockwise direction around it. However, moving in the backward direction the spin of the electron needs to flip by π or $-\pi$. The paths exhibit a difference of 2π and the wavefunction changes sign leading to destructive interference [124].

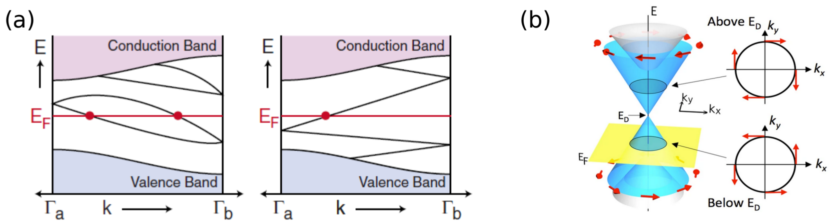

Fig. 6.2: (a) Electronic band structure of a topological trivial system (left) and a topological non-trivial system (right), which are distinguished by the dispersion of the conducting edge states between the Kramers degenerate points. In the trivial case the points are connected pairwise and the conducting surface states cross the Fermi level an even number of times. In the case of the non trivial system the number of crossings is odd and the edge states are connected with the following one. From [126]. (b) Spin texture in the Dirac cone of the surface state in a topological insulator, showing the spin-momentum locking of the electrons occupying the surface state bands. From [137].

The systems obeying TRS require the assignment of a new topological invariant, the $_2$ invariant because the Chern number fails to distinguish between the QSH state and a trivial insulator. The $_2$ invariant relates the change from a topologically trivial to a non-trivial system $\Delta\nu$ with the number of Kramers pairs N_K crossing the Fermi level [126]:

$$N_K = \Delta\nu \bmod 2\ . \tag{6.2}$$

Figure 6.2 a) shows the electronic band structure of a topologically trivial and non-trivial system between $k_x = 0$ and $k_x = \pi/a$. The band structure in the other half of the Brillouin zone is equivalent due to the TRS. The Kramers theorem determines that the states at 0 and π/a need to be 2-fold degenerate and the degeneracy is lifted at all other points. In the trivial case, shown in the left image of Figure 6.2 a), the edge states are connected pairwise and cross the Fermi energy an even number of times,

whereas, in the right image, the edge states cross the Fermi level an odd number of times. This makes the system topologically non-trivial, because the edge states cannot be pushed out of the gap without breaking time reversal symmetry [126].
The Hamiltonian to describe a 2D quantum spin Hall insulator is given by the Bernevig-Hughes-Zhang (BHZ) model

$$H_{\mathrm{BHZ}}(k) = \begin{pmatrix} h(k) & 0 \\ 0 & h^*(k) \end{pmatrix} , \tag{6.3}$$

with $h(k) = \epsilon(k) + d(k)\sigma$, with the vector of the Pauli matrices σ and

$$\epsilon(k) = C - D(k_{\mathrm{x}}^2 + k_{\mathrm{y}}^2) \tag{6.4}$$

$$d = [Ak_{\mathrm{x}}, -Ak_{\mathrm{y}}, M(k)] \tag{6.5}$$

$$M(k) = M - B(k_{\mathrm{x}}^2 + k_{\mathrm{y}}^2) \tag{6.6}$$

describing two copies of a massive Dirac Hamiltonian. The parameters A, B, C, D and M are material parameters that depend of the geometry of the quantum well. The gap in the Hamiltonian is given by the momentum-dependent effective mass $M(k)$ and changing the sign of M the gap is closed at $k = 0$, which turns a trivial insulator into a topological non-trivial quantum spin Hall insulator [133].

6.1.3 3D topological insulator Bi_2Se_3

The descriptions for 2D topological systems were extended into the 3 dimensional systems by different groups in 2006 [138, 139, 140] and a first experimental observation was made by Hsieh et al. in 2008 for $Bi_{1-x}Sb_x$ [141]. Later on, in 2009 Bi_2Se_3 was theoretically and experimentally confirmed via angle-resolved photoemission (ARPES) as a 3D topological insulator with a single Dirac cone at the surface, making it a model TI system [122, 142, 143]. The single Dirac cone at the surface of Bi_2Se_3 gives the impression to violate the *Fermion doubling theorem*, which determines the existence of an even number of Dirac cones in a system obeying TRS. A single Dirac cone can exist only as an edge state of a topologically non-trivial structure, where the partner Dirac cone is sitting on the opposite surface.
Bi_2Se_3 consists of a layered structure, stacked along z, with 5 layers forming one so-called quintuple layer (QL), with a height of approximately 1 nm, shown by the red box in Figure 6.3 a) and c). The bonding within one quintuple layer is strong, whereas the bonding between the quintuple layers is a weak van-der-Waals type. Bi_2Se_3 shows a rhombohedral crystal structure with space group $D_{3d}^5(R\bar{3}m)$. The lattice constants are $a = b = 4.140\,\text{Å}$ and $c = 28.636\,\text{Å}$ and each unit cell spans over 3 QL [144]. The single atomic layers form a triangular lattice, as shown in b), and are stacked ABCABC. The Se1 (Bi1) and Se1' (Bi1') refer to the same Se atoms and Se1 and Se2

refer to the different chemical states of the Se anions [145]. The crystal structure of Bi_2Se_3 possesses the following symmetries:

- three-fold rotation symmetry around the z-axis
- a two-fold rotation symmetry around the x-axis
- inversion symmetry, with the Se2 site as the inversion center
- and time reversal symmetry.

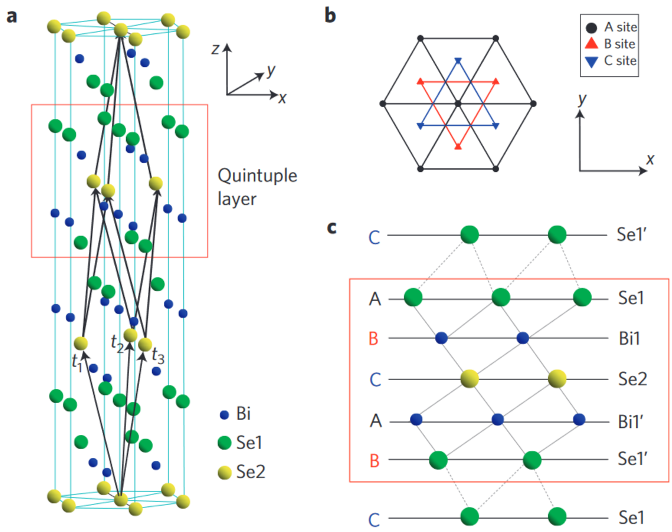

Fig. 6.3: a) Crystal structure of Bi_2Se_3. The red square shows one quintuple layer (QL) consisting of 5 atomic layers. The three primitive lattice vectors are denoted as $t_{1,2,3}$. b) shows the cross section from the crystal structure in the xy-plane. A cross section in the yz-plane is shown in c) Again the red box marks the atoms contained in one quintuple layer. Figure from [122].

The topological nature of the band structure in Bi_2Se_3 is manifested by the band inversion of two p-orbitals from Bi and Se with different parity, located close to the Fermi level. The authors in reference [122] show that this inversion is a result of strong spin-orbit coupling in Bi_2Se_3 and find the Fermi velocity of the surface states $v_F \sim 5.0 \times 10^5\,\mathrm{ms}^{-1}$. The surface states of the 3D topological insulator form a 2D metal, which is "half of an ordinary metal" [126],and which shows spin up and down states at every point of the Fermi surface. The spins in the surface state of a 3D topological insulator are not degenerate and due to TRS the spin at momentum $-k$ needs to be opposite of the spin at momentum $+k$. The spin is oriented perpendicular to the momentum and rotating with k around the Fermi surface. The edge states are again called helical edge states because they form a helical spin structure, which is described by the *spin momentum locking*, see Figure 6.2 (b). This property leads to a Berry phase of 0 or π acquired by an electron which circles around the Fermi surface due to the TRS. In the case of the Dirac point the spin is rotated by 2π leading to a Berry phase of π [126].

The high spin-orbit coupling of Bi_2Se_3 makes it a key material for spintronic applications. ST-FMR experiments have shown a spin-Hall angle between 2.0 and 3.5, which is a factor of 25 higher than the spin Hall angle in Pt [146]. Optical experiments have similarly shown THz radiation generated by spin-to-charge conversion via the inverse Rashba Edelstein effcet in Co/Bi_2Se_3 heterostructures, with a similar efficiency to a Pt/Co heterostructure [147, 148]. Besides spin-to-charge conversion mechanisms ultrafast photocurrents at the surface of Bi_2Se_3 and interfaces with other materials were shown to generate THz radiation [149, 150, 151, 152]. The interface properties, especially the band bending was found to play a decisive role for the strength of THz generation.

6.2 Sample set

We investigated two different Bi_2Se_3 thin film samples with varying thickness, both grown on a glass substrate. The Bi_2Se_3 wedge varies from 6 to 70 nm, where one of them is left without cover and the second is covered with a 3 nm Al layer to prevent surface oxidation, see Figure 6.4. The samples were fabricated by Kiryl A. Niherysh in the Department of Micotechnology and Nanoscience of the Chalmers University of Technology in Sweden with the technique described in reference [153]. Both samples

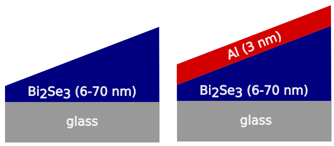

Fig. 6.4: Investigated sample systems with varying thickness of Bi_2Se_3.

have a size of 25 x 75 mm. The thickness variation over the 75 mm is non-linear and the thickness gradient varies linearly along the wedge. Figure 6.5 a) shows the thickness of Bi_2Se_3 versus the position on the sample from 5 mm to 70 nm, which can be fitted by a power law and results in a linear relationship between the gradient and the thickness of the sample, see Figure 6.5 b).

The thickness dependent reflectance and the transmittance in Bi_2Se_3/Al were measured using laser light with a wavelength of 800 nm and a vertical and horizontal polarization in the reflection geometry under an incidence angle of 45°. The results are shown in Figure 6.6 a) and show an exponential decrease for the transmittance

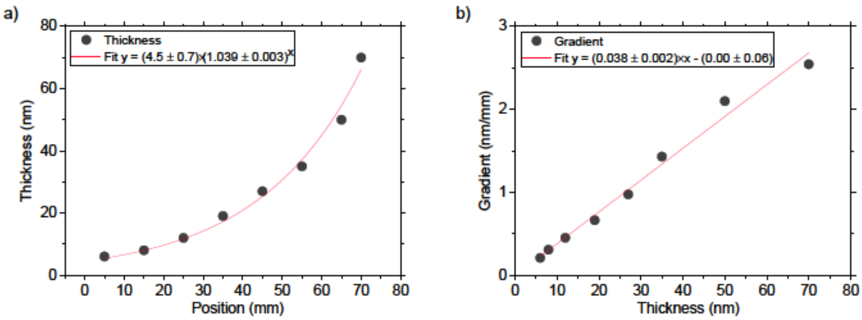

Fig. 6.5: a) Thickness of Bi_2Se_3 measured with an atomic force microscope versus the position on the sample in mm, which can be fitted by a power law. b) The gradient vs. the thickness of the sample obtained from the derivative of the fit in a).

(shown in green) with growing wedge thickness. The reflectance (shown in blue) shows an increase up to a wedge thickness of approximately 32 nm. Above 32 nm the reflectance is decreasing with the thickness. From the amount of reflected light R and transmitted light T we calculate the absorption A of the laser light in the Bi_2Se_3 wedge versus the thickness, taking into account that $A + R + T = 1$. The result is shown in Figure 6.6 b). Especially the reflectance in a) shows a dependence on the polarization of the incoming light, which transfers also to the absorption, and leads to a stronger absorption for p-polarized light. For most of the wedge (10-35 nm) the absorption changes are small; for p-polarized light between 0.03 and 0.035 and for s-polarized light between 0.02 and 0.03. Stronger changes are observed at thicknesses below 10 nm and above 35 nm, where the absorption increases with the Bi_2Se_3 wedge thickness.

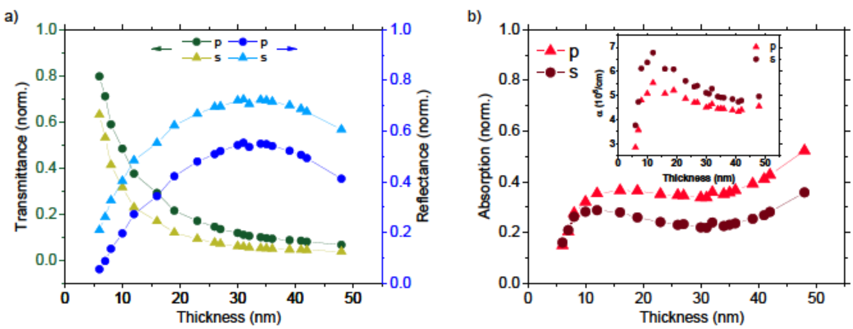

Fig. 6.6: a) Thickness dependent reflectance and transmittance of a 800 nm laser pulse for Bi_2Se_3/Al and b) the resulting thickness dependent absorption in the case of s- and p-polarized laser light. The inset shows the corresponding absorption coefficient α.

We extract the absorption coefficient α with the help of the Lambert-Beer law $I =$

$I_0(1-R)\exp(-\alpha d)$, where I_0 is the initial intensity of the light, R is the reflectance, I is the intensity of the transmitted light and d is the thickness of the wedge. The result is depicted in the inset in Figure 6.6 b). It shows clearly that the light absorption is changing over the sample thickness. At larger thicknesses the absorption coefficient agrees well with reported values for the bulk in literature, e.g., $4.76 \cdot 10^5 \mathrm{cm}^{-1}$ in reference [154] using a very similar setup configuration or $2 \cdot 10^5 \mathrm{cm}^{-1}$ from reference [155]. The authors in reference [154] show a strong increase of the absorption coefficient when the thickness is decreasing in Bi_2Se_3. However, this is not observed in our samples. Below 12 nm of thickness we observe a strong decrease of the absorption coefficient.

The surface of the Bi_2Se_3 wedge without any capping is exposed to air and likely to be oxidized. Literature shows that leaving Bi_2Se_3 exposed to air leads to a degradation of the surface and the formation of BiO_x at the surface layer [156, 157]. Covering the sample with an Al layer can prevent the oxidation of the surface and maintain the transport properties of the TI surface as shown in reference [158]. In reference [156] and [157] the thickness of the oxide layer was found to be 2-3 nm after one week of air exposure of the Bi_2Se_3 sample. We investigated the surface of a Bi_2Se_3 wedge fabricated with the same parameters as the ones shown in this investigation using Raman spectroscopy, which shows that a BiO layer is formed at the surface of the sample after exposure to air for several weeks, see Figure 6.7 b). The peak at $250\,\mathrm{cm}^{-1}$ is not present in the Raman spectra in a), taken after the fabrication and show the E_g^2 and A_{1g}^2 peak at $131\,\mathrm{cm}^{-1}$ and $175\,\mathrm{cm}^{-1}$ [159, 160]. The oxidation of the Bi_2Se_3 surface has several consequences. First, it will lead to a reduced effective thickness of the Bi_2Se_3 wedge as the surface will be covered with a few nm of BiO. Additionally, we expect the surface state to shift down in energy into the occupied states, as was observed in reference [161]. Despite the surface degradation, the distinctive surface state properties were shown to be conserved [161]. Furthermore, with the surface oxidation, the authors in references [162, 163] observed the formation of a 2D-electron gas (2DEG) at the surface of Bi_2Se_3.

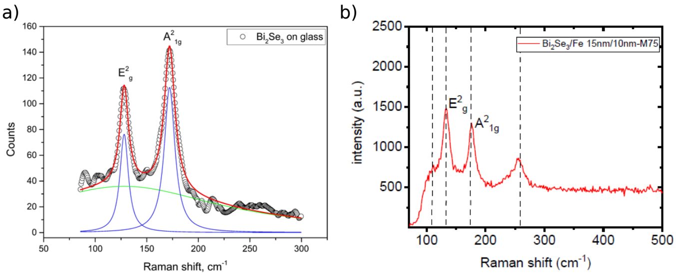

Fig. 6.7: a) Raman spectrum of Bi_2Se_3 without capping at 10 nm thickness. Visible are the E_g^2 and A_{1g}^2 peak at $131\,\mathrm{cm}^{-1}$ and $175\,\mathrm{cm}^{-1}$. b) Raman spectrum of Bi_2Se_3/Fe at 10 nm thickness showing the E_g^2 and A_{1g}^2 peak and an additional peak at $250\,\mathrm{cm}^{-1}$ originating from the formation BiO at the surface.

6.3 Thickness dependent THz emission in Bi_2Se_3

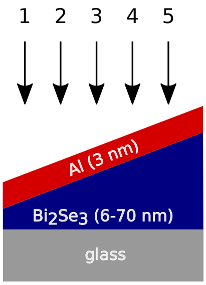

Fig. 6.8: Schematic illustration of the thickness dependent measurements for a varying thickness of Bi_2Se_3.

This section presents a study on the thickness-dependent THz emission from the Bi_2Se_3-based THz emitters with variable Bi_2Se_3 thickness presented above. The samples were mounted on a vertical translation stage, which moved the sample along its long axis, such that the pump beam position on the sample is shifted along the direction of the thickness gradient, see schematic illustration in Figure 6.8. The measurements were performed in the reflection geometry shown in Figure 3.1 b) with a laser power of 240 mW, resulting in a fluence of $2.7\,\mu\mathrm{J/cm}^2$ impinging on the sample and no magnetic field applied. For both Bi_2Se_3 bilayers THz transients were measured over the full thickness range under varying pump beam polarization. We have tested the excitation with s- and p-, as well as left- and right circularly polarized light.

Figure 6.9 compiles the thickness-dependent THz investigation for the Bi_2Se_3 wedge without capping for a thickness from 5 nm to 66 nm. The graph in a) shows the THz transients obtained under excitation with a p-polarized pump beam. The transients are offset for better visibility and show that the THz amplitude is changing with the Bi_2Se_3 wedge thickness. The full sets of transients obtained under s- and circularly polarized light can be found in the appendix in Figure B.1.

Figure 6.9 b) depicts the maximum THz transient amplitudes A^{THz} as a function of Bi_2Se_3 wedge thickness for all measured excitation polarizations. A^{THz} varies with the thickness, independent of the pump beam polarization. At small thicknesses up to approximately 15 nm the THz transient amplitudes are strongly increasing. Between 15 nm and 30 nm the amplitudes saturate and show a dip around 41 nm. At the larger thicknesses the amplitude shows a linear increase with the thickness.

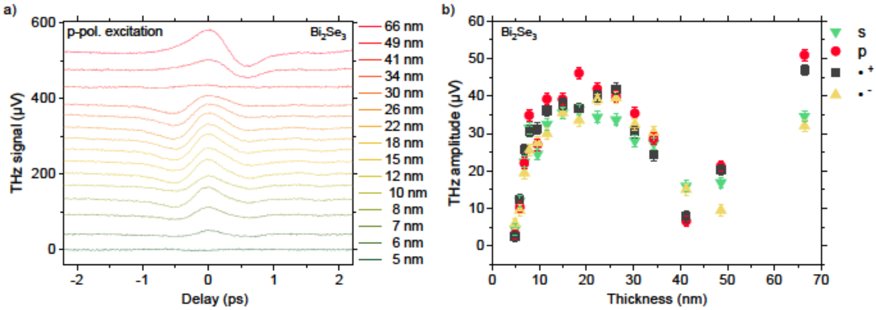

Fig. 6.9: a) Thickness dependent THz transients from Bi_2Se_3 without capping obtained by the illumination with p-polarized light. b) THz transient peak amplitudes from Bi_2Se_3 without capping for an excitation with a s-, p-, left- and right circular polarized pump beam at different thicknesses of Bi_2Se_3.

At the same conditions, the thickness-dependent THz transients were measured for the Bi_2Se_3/Al bilayer. The full set of transients for all excitation polarizations are again shown in the appendix in Figure B.2.

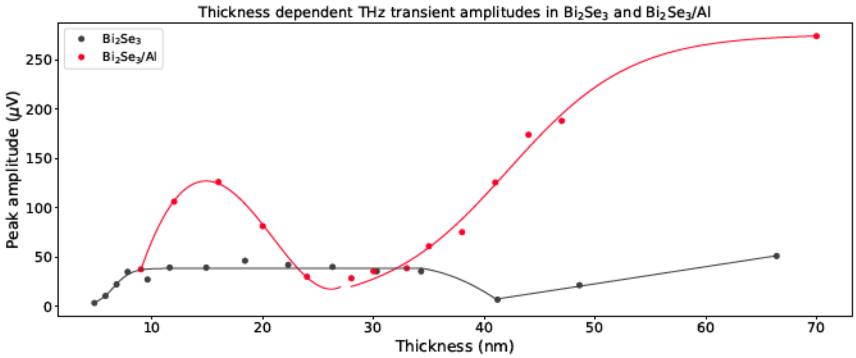

Fig. 6.10: Maximal THz peak amplitudes for Bi_2Se_3 without capping (grey) and Bi_2Se_3/Al (red) versus the thickness of the Bi_2Se_3 layer using a p-polarized excitation beam. The lines are a guide for the eye and computed for small and large thickness separately.

To make a comparison between the samples we plot both thickness dependencies for p-polarized excitation in Figure 6.10. One can recognize the overall qualitatively similar trend in both of the systems. The THz transient amplitudes show a strong increase at small thicknesses (<15 nm). In the case of Bi_2Se_3 without capping, the amplitudes show a saturation at approximately 40 μV from around 10 nm upwards and remain at the same level until the thickness reaches 35 nm. In contrast, the amplitudes of Bi_2Se_3/Al increase much higher and show an amplitude of 130 μV at a thickness of 16 nm, which is approximately 3.3 times higher with respect to Bi_2Se_3 without capping. After this peak, the amplitudes in Bi_2Se_3/Al decrease until they reach the same level as the amplitudes of the uncapped sample. We rule out that the increase and decrease of the THz transient amplitude in Bi_2Se_3/Al is created by a stronger absorption of the pump pulse because the thickness-dependent absorption in Bi_2Se_3/Al, shown in Figure 6.6 b), presents a change in absorption below 8% absolute in the range from 10 to 30 nm. We consequently ascribe the changes of the THz transient amplitudes to a change in the strength of the underlying THz generation mechanisms.

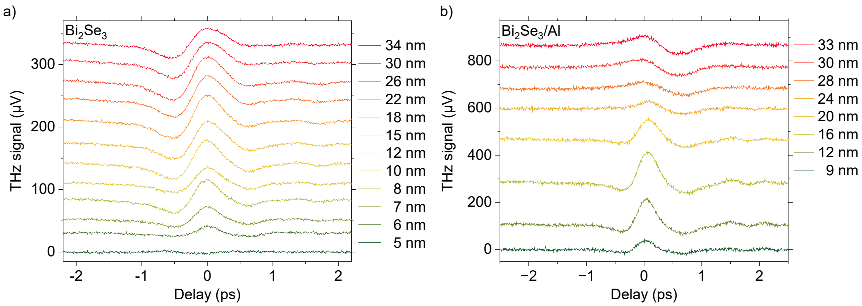

Fig. 6.11: Comparison of the thickness dependent THz transients for a) Bi_2Se_3 without capping and b) Bi_2Se_3/Al in the thickness range from 5 nm to 35 nm under the excitation with p-polarized light.

Figure 6.11 shows the THz transients at varying thicknesses up to 34 nm for Bi_2Se_3 without capping in a) and Bi_2Se_3/Al in b). For a better visibility, the transients are offset in y. An interesting feature of the THz transient shape is observed when comparing the transients at different thicknesses for both samples. With increasing thickness the THz transients in Bi_2Se_3/Al are changing the shape from a single peak to a bipolar shape. The change occurs between 20 and 24 nm of Bi_2Se_3 thickness, see Figure 6.11 b). In contrast to this, the THz transient shape in Bi_2Se_3 without capping remains the same between 5 and 34 nm thickness of Bi_2Se_3, as can be seen in a). Figure 6.12 a) shows the THz transients in Bi_2Se_3/Al at a thickness of 16 nm and 28 nm, corresponding to the highest and lowest amplitude transients of the measured set shown in 6.11 b). It is clearly visible that the two transients show distinct shapes, suggesting a difference in the underlying THz generation mechanism. Figure 6.12 b) shows the power spectra of the transients shown in a) and the corresponding 3 dB-cutoffs at 0.78 THz for 28 nm and 1.31 THz for 16 nm.

In contrast to the increased amplitudes in Bi_2Se_3/Al at 16 nm, the THz transient amplitudes at Bi_2Se_3 thicknesses between 25 nm and 32 nm are very similar in both wedges, see Figure 6.10. This suggests that the THz mechanism leading to the high amplitudes in Bi_2Se_3/Al is either decreasing in strength when the thickness is increasing or that several THz generation mechanisms from the top and bottom interface are contributing to the measured signal. With the increasing thickness of Bi_2Se_3 we loose the sensitivity to the interface between the glass substrate and Bi_2Se_3. The penetration depth of the 800 nm laser beam is around 16-20 nm in Bi_2Se_3/Al (see Figure 6.6 b), which coincides with the thickness, at which the THz amplitude starts to decrease in Bi_2Se_3/Al. We expect both samples to show the same THz strength from the bottom interface between Bi_2Se_3 and glass as there was no difference in the fabrication technique. This suggests that the signals from both Bi_2Se_3 interfaces are interfering constructively and adding up to a higher THz transient amplitude.

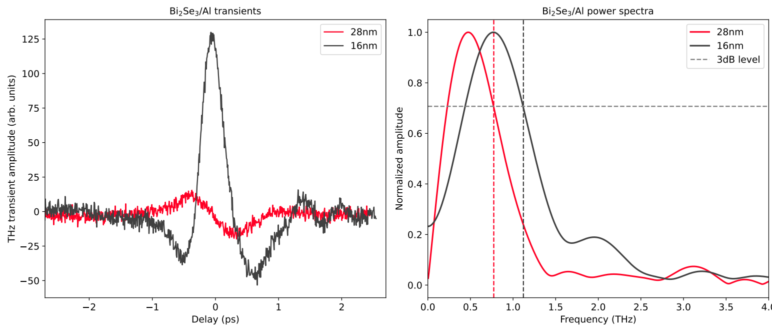

Fig. 6.12: a) Comparison of the THz transients in Bi_2Se_3/Al at a thickness of 16 nm and 28 nm. b) Normalized FFT spectra of THz transients shown in a). The grey dashed line marks the 3 dB-level and the vertical dashed line, the corresponding frequency 3 dB-cutoffs at 0.78 THz for 28 nm thickness and 1.31 THz for 16 nm thickness.

Comparing also the THz transient amplitudes at the thicker part of the wedge with amplitudes up to 70 nm one notes that in both samples the THz transient peak amplitude $A^{\mathrm{THz,\,max}}$ increases with increasing thickness of the Bi_2Se_3 wedge. However, it is clearly visible that the increase is much stronger in the sample capped with 3 nm of Al. The dip in THz transient amplitude observed for Bi_2Se_3 without capping at 41 nm thickness is observed around 26 nm Al and is much broader. Additionally the amplitude decrease is less in Bi_2Se_3/Al with a minimal peak amplitude of 35 μV compared to 6 μV in Bi_2Se_3 without capping. At 50 nm (70 nm) thickness the amplitude is approximately 9 times (5 times) higher in Bi_2Se_3/Al. For thicknesses above ~50 nm we observe a saturation of the THz transient amplitudes in Bi_2Se_3/Al. This shows that even at increased thickness of Bi_2Se_3 the Al layer has a strong influence on the THz emission.

With increasing thickness from 40 nm to 50 nm the absorption shows an increase by 33% (as shown in Figure 6.6 b)). The increase of $A^{\mathrm{THz,\,max}}$ is 50% in Bi_2Se_3/Al and

200% in Bi_2Se_3 without capping layer. This shows that the increase in $A^{\mathrm{THz,\,max}}$ is not solely due to an increase in absorption, but an increase in strength of the THz generation mechanism.
Figure 6.13 a) compares THz transients from both samples at a thickness of approximately 70 nm. Although the shape of the transients is different, the power spectra in b) show a very similar maximum frequency of 0.36 THz (Al-capped wedge) and 0.38 THz (non-capped wedge) and a 3 dB cut-off at 0.60 THz for Bi_2Se_3/Al and 0.65 THz for Bi_2Se_3 without capping.

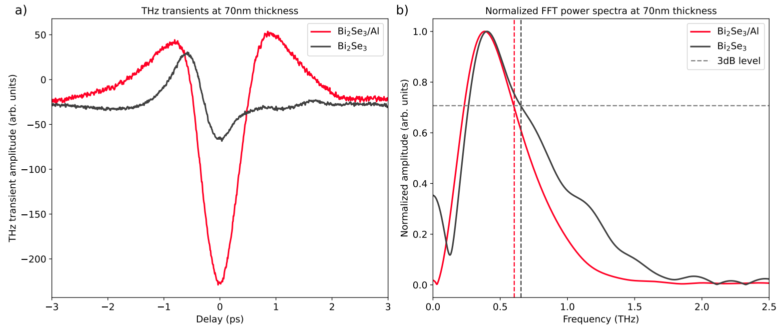

Fig. 6.13: a) Comparison of the generated THz transient in Bi_2Se_3 without capping and Bi_2Se_3/Al at ~70 nm thickness and the corresponding normalized power spectra of the transients in b).

The fact that the amplitudes A^{THz} are enhanced in the Al capped Bi_2Se_3 wedge shows that the interface has a strong influence on the THz generation mechanism and the effect at the thinner part of the wedge is likely to be a surface/interface effect. However, the comparison of the two Bi_2Se_3 bilayer shows that the increase in A^{THz} is not the same at all the measured Bi_2Se_3 thicknesses. This indicates that it is likely to find more than one THz generation mechanism in Bi_2Se_3 bilayers over the thickness range of 5 to 70 nm. The following part will show the investigations of excitation with circularly polarized light and an azimuthal angle dependence and compare the results from both wedges.

6.3.1 Excitation with circularly polarized light (<35 nm)

In the next part, we will discuss the THz transients generated from Bi_2Se_3 wedges under the excitation with circularly polarized light. Figure 6.14 a) shows the THz transients generated in Bi_2Se_3/Al with circularly polarized light σ^+ and σ^- at 15 nm thickness. The transients show a clear difference in amplitude of the first negative peak, resulting from the reversed helicity.
From the measured THz transients, we extract a THz component that depends solely on the helicity of the pump beam and is a consequence of pure (helicity-dependent) HD

excitation. We made two considerations for this. First, every THz signal $S(\sigma^+)$ and

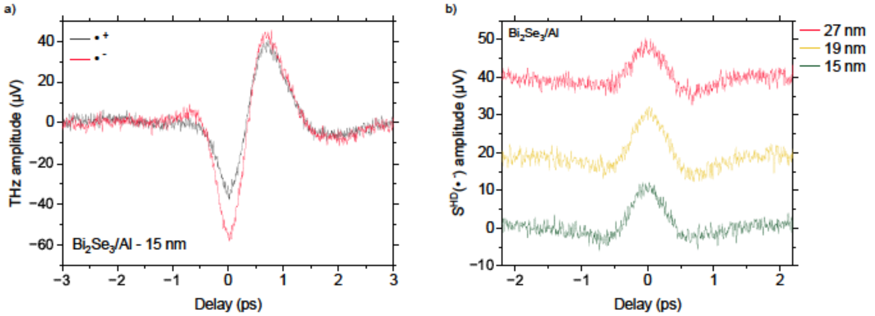

Fig. 6.14: a) Measured THz transients at a thickness of 15 nm in Bi_2Se_3/Al under excitation with left σ^+ and right σ^- circularly polarized light. b) Extracted HD components $S^{\mathrm{HD}}(\sigma^-)$ in Bi_2Se_3/Al at thicknesses 15, 19 and 27 nm. The transients are offset in y for a better visibility.

$S(\sigma^-)$ obtained under the excitation with left- or right-circularly polarized pump beam consists of a helicity-dependent component S^{HD} and a helicity-independent component S^{HI}:

$$S(\sigma^-) = S^{\mathrm{HI}} + S^{\mathrm{HD}}(\sigma^-) \tag{6.7}$$
$$S(\sigma^+) = S^{\mathrm{HI}} + S^{\mathrm{HD}}(\sigma^+)\,. \tag{6.8}$$

Second, we assume that S^{HD} is antisymmetric under the reversal of the helicity, which is expressed via $S^{\mathrm{HD}}(\sigma^-) = -S^{\mathrm{HD}}(\sigma^+)$. To extract S^{HI} and S^{HD} we therfore measure first $S(\sigma^-)$ and $S(\sigma^+)$ and then we extract S^{HI} via $S^{\mathrm{HI}} = (S(\sigma^-) + S(\sigma^+))/2$, which follows from the two assumptions made above. The HD components are then retrieved using

$$S^{\mathrm{HD}}(\sigma^-) = \frac{S(\sigma^-) - S(\sigma^+)}{2} \tag{6.9}$$
$$S^{\mathrm{HD}}(\sigma^+) = \frac{S(\sigma^+) - S(\sigma^-)}{2}\,. \tag{6.10}$$

The extracted HD THz transients $S^{\mathrm{HD}}(\sigma^-)$ are shown in Figure 6.14 b) for three thicknesses. From these HD signals we extract the peak amplitudes, shown in 6.15 a) for all measured THz transients. We assumed the HD component to be mirrored under the reversal of the helicity and consequently the amplitudes of the HD components extracted from $S(\sigma^+)$ show the same absolute values (not shown). The peak amplitudes of S^{HD} in Bi_2Se_3 without capping are below 4 μV, but a clear HD signal is observed for Bi_2Se_3/Al. The maximal absolute HD amplitude in Bi_2Se_3/Al is found at 15 nm thickness with 11 μV and is consequently four times higher with respect to the uncapped Bi_2Se_3 wedge. In contrast to the THz transients obtained under p-polarized

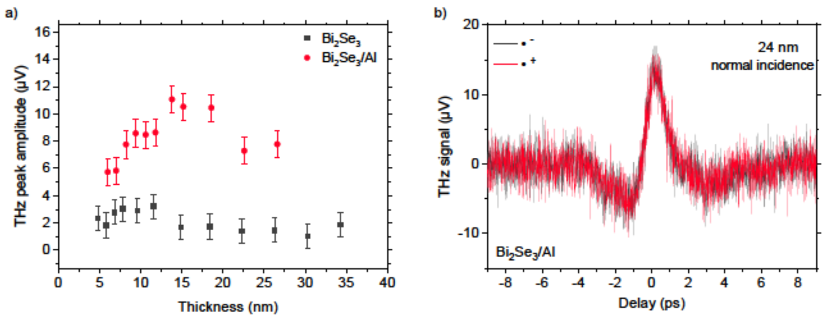

Fig. 6.15: a) Helicity dependent absolute peak amplitudes for the Bi_2Se_3 sample systems extracted from the transients generated with opposite helicity. b) THz transients obtained under excitation with circularly polarized light in the transmission geometry, hence an incidence angle of approximately 5° at 24 nm thickness of Bi_2Se_3 in Bi_2Se_3/Al.

excitation we observe no difference in shape for the HD component at 15 nm and 27 nm under the excitation with circularly polarized light, see Figure 6.14 b). This suggests that there is no change in the dominating THz generation effect for helicity-dependent THz generation with increasing thickness of Bi_2Se_3.
Comparing the HD THz signal in the reflection geometry with an incidence angle of 45° with the one obtained in the transmission geometry, where the incidence angle was approximately 5°, displayed in Figure 6.15 b), reveals that the HD component is vanishing under almost normal incidence. We note that the transmission and reflection geometry might not be exactly comparable and the vanishing of the HD component could be caused by different effects. Nevertheless, it suggests that S^{HD} is sensitive to the incidence angle of the light. In the surface state of Bi_2Se_3 the spin momentum locking leads to an in-plane spin arrangement, as shown in 6.2 b). With an incidence angle of 45° the angular momentum of the light has a component in the plane of the Bi_2Se_3 surface and can couple to the surface electron spins. This suggests the involvement of surface electrons in the generation of S^{HD}.

6.3.2 Circularly polarized excitation (>20 nm)

This section compiles results that were obtained using a circularly polarized pump beam. Figure 6.16 compiles the thickness-dependent THz transients of Bi_2Se_3 without capping in a) and Bi_2Se_3/Al in b) in the thickness range between 21 nm to 70 nm. The excitation with left or right circularly polarized light is shown by the light and dark curves, respectively. The curves at different thicknesses are offset for better visibility and following the curves from top to bottom (thin to thick) an increase of the amplitude difference between the transients with opposite helicity can be noted. Both the amplitude and the difference between $S(\sigma^+)$ and $S(\sigma^-)$ are higher in the case of Bi_2Se_3/Al.

Using again Equation 6.8 we extract $S^{\mathrm{HD}}(\sigma^+)$ and $S^{\mathrm{HD}}(\sigma^-)$ the THz component depending solely on the helicity of the pump beam. Figure 6.17 a) presents S^{HD} for both

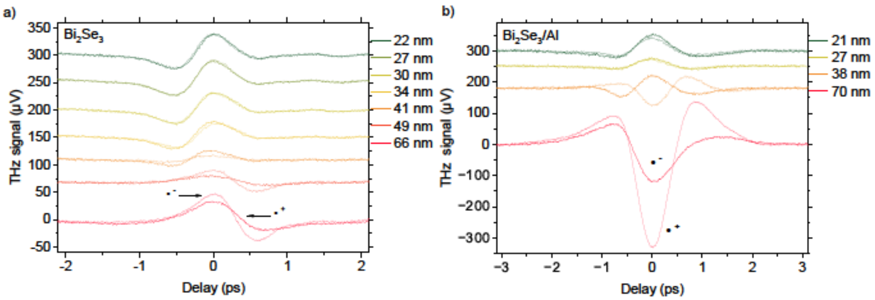

Fig. 6.16: THz transients in Bi_2Se_3 without capping a) and Bi_2Se_3/Al b) at thicknesses between 34 nm and 66 nm for an excitation with right circular polarized light (dark color) and left circular polarized light (light color). The transients at different thicknesses are offset for better visibility.

helicities in Bi_2Se_3/Al and Bi_2Se_3 without capping at a thickness of approximately 70 nm. The transients for Bi_2Se_3 without capping are offset for better visibility and show an amplitude A^{HD} of $\pm 20\,\mu$V. In Bi_2Se_3/Al the amplitude reaches a value of $110\,\mu$V and is consequently 5.5 times higher.

Besides the different amplitudes also the shape of the extracted $S^{\mathrm{HD}}(\sigma^+)$ THz transients is different for the two samples. The transients in the Bi_2Se_3 wedge without a capping layer show a single peak, while the transients for the Al-capped Bi_2Se_3 wedge are bipolar.

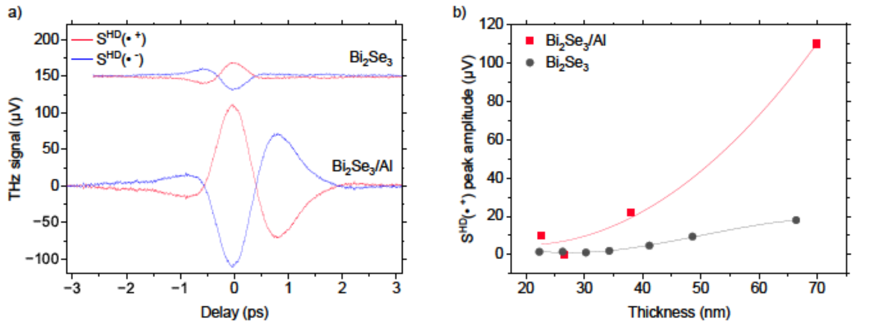

Fig. 6.17: a) Comparison of the extracted pure helicity dependent components $S^{\mathrm{HD}}(\sigma^+)$ and $S^{\mathrm{HD}}(\sigma^-)$ in Bi_2Se_3 without capping (67 nm) and Bi_2Se_3/Al (70 nm). The transients for Bi_2Se_3 without capping are offset for better visibility. b) shows the peak amplitudes of $S^{\mathrm{HD}}(\sigma^+)$ in Bi_2Se_3 without capping (grey) and Bi_2Se_3/Al (red) versus the thickness of Bi_2Se_3. The lines serve as a guide for the eye.

In both samples the helicity dependent signal is growing with the thickness of the

Bi_2Se_3 wedge, as can be seen in Figure 6.17 b), where the thickness-dependence of the peak amplitudes is shown for both bilayers. The increase is observed starting from 30-35 nm and is much stronger in Bi_2Se_3/Al.

6.3.3 Azimuthal angle dependence

In order to understand the underlying symmetries of the emitted THz generation, Bi_2Se_3/Al was mounted on a rotation stage and rotated around its azimuthal angle. Three thickness positions were chosen to evaluate the azimuthal angle dependence in Bi_2Se_3/Al. The first one at approximately 9 nm thickness, where the THz transient amplitudes of the two sample systems are similar under the excitation with p-polarized light (as shown in Figure 6.10). The second position is around a thickness of 15 nm, where the amplitude of the Bi_2Se_3/Al sample is three times higher with respect to the Bi_2Se_3 sample without capping and the third position was chosen to be at 41 nm thickness. The detection axis of the PCA detector is set along the vertical direction, consequently detecting the E_x component of emitted THz radiation.
The azimuthal angle dependence of the peak amplitudes under linearly and circularly polarized excitation is shown in Figure 6.18 a) for a thickness of 9 nm and a thickness of 15 nm in b). Independent of the light polarization used to excite the sample, two

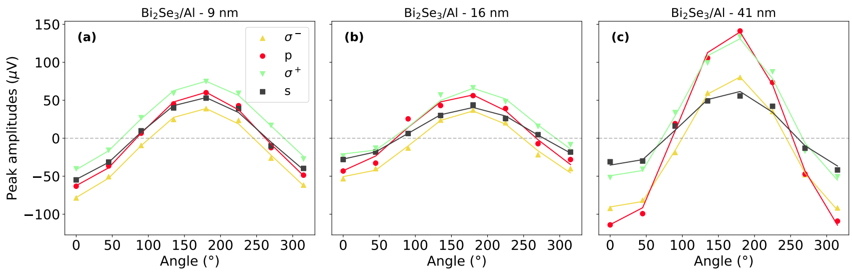

Fig. 6.18: Peak amplitudes of the THz signal at different azimuthal angles in Bi_2Se_3/Al obtained under illumination with p- (red dots), s- (green triangles), σ^-- (yellow triangles) and σ^+-polarized light (grey squares) at a sample thickness of 9 nm in a), 15 nm in b) and 41 nm in c).

orientations with the maximal THz amplitude are observed. These positions are at an angle of 0° or 180°, coinciding with the long axis of the sample in the detection direction of the THz detector. The long axis of the Bi_2Se_3 wedges is the axis over which the thickness is changing, and therefore, the thickness gradient is either aligned parallel or anti-parallel to the detection direction. This illustrates that there is an asymmetry in the plane of the Bi_2Se_3 wedge, leading to non-canceling current contributions with and against the gradient direction of the sample. It was shown in Figure 6.5 that the thickness gradient varies over the wedge thickness and is small at the thinner part of

the wedge. In case of a contribution from the thickness gradient, we expect this effect to be much more pronounced at the thicker part of the wedge.
Same as for the small thickness regime we show the azimuthal angle dependence of THz transient amplitudes obtained at 41 nm thickness of Bi_2Se_3 in Figure 6.18 c). We observe the exact same trend as for the smaller thicknesses, with the maximal THz transients amplitude along the axis of varying Bi_2Se_3 thickness. The axis with the maximal THz peak amplitude is independent of the polarization of the exciting laser pulse and suggests the thickness gradient to play a major role in the THz generation in Bi_2Se_3 wedged layers.
As shown in the previous section a clear contribution of a helicity dependent signal is observed at the larger Bi_2Se_3 thicknesses as the THz transients show different maximal amplitudes for an excitation with opposite helicity. The azimuthal angle dependence reveals that the THz transients are mirrored by performing two operations as illustrated in 6.19 a) and b) as follows: starting from the grey curve in a) obtained at 45° azimuthal angle with σ^- polarized light, first a rotation of the sample by 180° around its azimuth to 225° and second a reversal of the helicity of the excitation beam to σ^+ is mirroring the THz transients. The same is observed for the THz transients with σ^- polarized excitation at 45° azimuthal angle, shown in b).

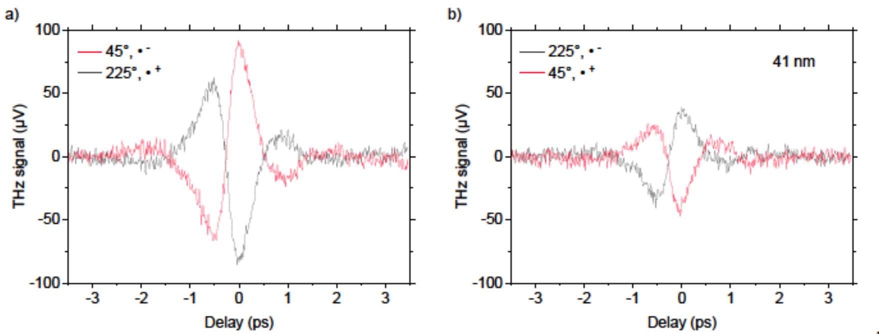

Fig. 6.19: THz transients in Bi_2Se_3/Al at a thickness of 41 nm measured in the reflection geometry for a) an azimuthal angle of 45° (σ^-) and 225° (σ^+) and the reversed case in b) with an azimuthal angle of 45° (σ^+) and 225° (σ^-) .

We again extract S^{HD} and S^{HI} using equation 6.8 and the results for the thickness of 41 nm are shown in a polar plot in Figure 6.20 b). The trend for S^{HI} agress with the one obtained for the linear excitation shown in Figure 6.18 c) and shows a 2-fold symmetry with the maxima at 0° and 180°. Additionally the THz transients of S^{HI} and the ones obtained by s- or p-polarized are the identical, as shown in the appendix Figure B.4. In contrast, the HD component S^{HD} demonstrates no amplitude variation under the rotation of the azimuthal angle. In Figure 6.20 a) we show the results for S^{HD} and S^{HI} at a thickness of 15 nm. We observe the exact same trend at the thickness of 15 nm with the 2-fold symmetry for the S^{HI} and independence of the

azimuthal angle for S^{HD} as for the thickness of 41 nm.
Due to the inversion symmetry of the bulk we expect S^{HD} to originate from the surface of Bi_2Se_3. The independence of the azimuthal angle of the HD component agrees with the thesis of excitations of the surface state electrons. Due to the spin-momentum locking the spins are oriented in a circular arrangement, see Figure 6.2 b) and a rotation around the azimuthal angle should not change the HD component, as the angular momentum of the light is always aligned to one of the electron spins.
From the polar plot in 6.20 it is clearly visible that the HI amplitude at 0° is smaller with respect to the amplitude at 180°, by approximately 13 μV. From the thickness dependence of the THz peak amplitudes one can estimate that a shift of the amplitudes by 13 μV could be caused by a shift of the laser spot on the sample by $\sim$2 mm during the rotation around its azimuth. This yields a Bi_2Se_3 thickness change of approximately 1.4 nm and could consequently explain the difference for the two reversed configurations. The HD component displays no dependence on the azimuthal angle and remains constant for all investigated angles. The thickness dependence of the HD dependent transients shows only a small signal for Bi_2Se_3/Al and no big difference in the amplitude is expected for a shift of the laser spot on the sample.

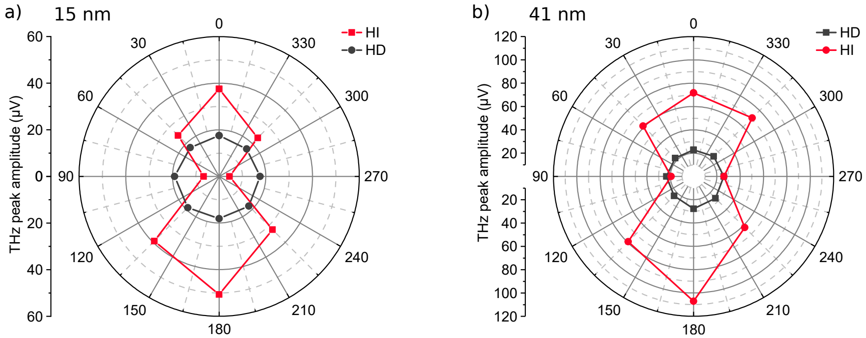

Fig. 6.20: Azimuthal angle dependence of the $S^{\mathrm{HD}}(\sigma^+)$ and S^{HI} in Bi_2Se_3/Al at a wedge thickness of a) 15 nm and b) 41 nm in polar coordinates obtained from the excitation with circularly polarized light of opposite helicities.

6.3.4 THz component E_y & out-of-plane contributions

Until now the detection system was sensitive only to the E_x THz component. To measure also the E_y THz component the sensitive axis of the PCA detector was set to the horizontal direction and the THz transients measured in the reflection geometry. Figure 6.21 shows the THz transients for Bi_2Se_3 without capping under the excitation with left- and right-circularly polarized light in a) and s- and p-polarized light in b), which are indicated by the light and dark curves. Changing the helicity of the circularly polarized pump beam results in a different amplitude of the THz tran-

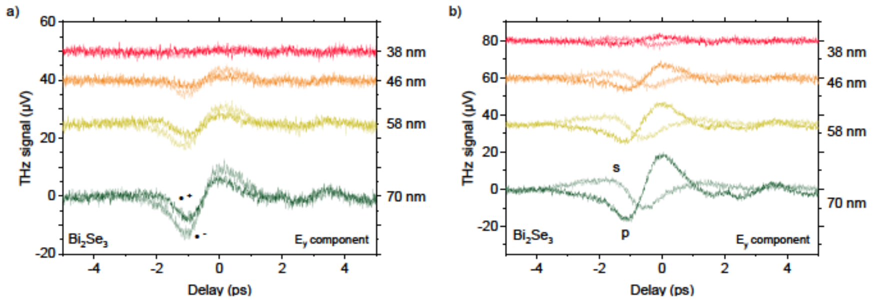

Fig. 6.21: a) Thickness dependent THz transients of the E_y component in Bi_2Se_3 without capping under the excitation with circularly polarized light. The darker curves represent the THz transients obtained under excitation with right circularly polarized light and the lighter ones are obtained from a left circularly polarized excitation. For a better visibility the curves are offset in y. b) shows the E_y THz component under the excitation with linearly polarized light with the darker curves representing a p-polarized excitation and the lighter ones a s-polarized excitation.

sient. This difference is growing with the thickness of the sample, as observed for the E_x component. A difference in the amplitudes is also observed in Figure 6.21 b), when the polarization is changed from s to p, which is also growing with the thickness of Bi_2Se_3. In contrast to the circularly polarized excitation, changing the polarization of the pump pulse from s-polarized to p-polarized the transient shows a completely different THz transient profile with an inverted peak amplitude.

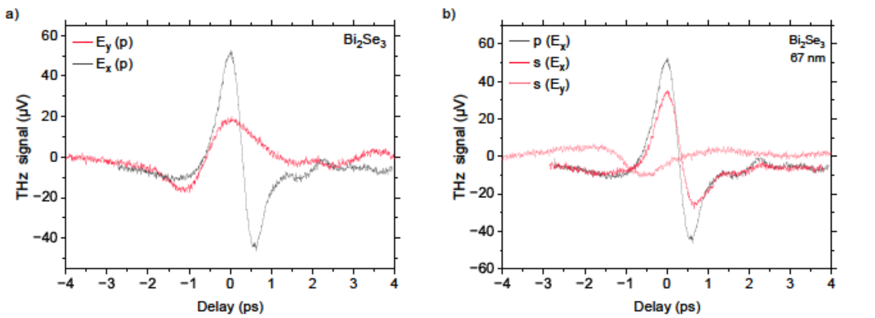

Fig. 6.22: a) Comparison of E_x and E_y THz transients under p-polarized excitation in Bi_2Se_3 without capping at 67 nm thickness. b) Comparison of E_x and E_y THz transients obtained under s-polarized excitation in Bi_2Se_3 without capping at 67 nm. Additionally we show the E_x THz transient under p-polarized excitation.

Figure 6.22 a) compares the E_x and E_y-THz transients obtained under p-polarized excitation in Bi_2Se_3 without capping at 67 nm thickness. The amplitude $A^{THz,\ max}$ is 2.5 times higher for E_x with respect to the E_y component. Because of the incidence angle of 45° and the rotation of the sensitive axis of the PCA in the horizontal direction, the

E_y component contains a contribution from in-plane as well as out-of-plane currents, see Figure 6.23. The contribution from the out-of-plane component is smaller by a factor 1/2 because of the dipole is oriented normal the surface and consequently 45° to the detection axis.

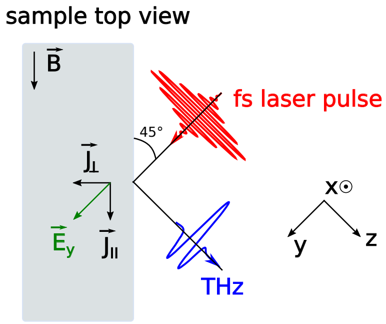

Fig. 6.23: Schematic illustration of projections of in-plane $\vec{J}_{\|}$ and out-of-plane current contribution $\vec{J}_{\perp}$ contributing to the E_y THz component.

Figure 6.22 b) shows the E_x THz component (previous section) of Bi_2Se_3 without capping at 67 nm, presenting also a change in the $A^{\mathrm{THz,\,max}}$ by a factor 1.5, when the polarization is changed from s-(red) to p-polarized (grey). Even though the amplitude is changing the THz transients shape remains the same when changing the polarization direction. For a comparison we show the THz transient obtained under s-polarized excitation (pink), which demonstrates the change in shape for the E_x component. We attribute this change of the shape to the out-of-plane current contribution.

Another way to investigate the current that is flowing normal to the surface of the sample is to apply a magnetic field in the horizontal direction. Due to the Lorentz force the electrons will be deflected in the vertical direction and can be measured with the PCA sensitive axis set in the vertical direction (E_x). Reversing the magnetic field direction will lead to the charges flowing in the opposite direction and consequently yield a reversed polarity of the THz transient.
Figure 6.24 a) shows the THz transients measured with a static magnetic field of ± 85 kA/m. Depending on the direction of the magnetic field the THz transient amplitude is increasing or decreasing, indicating that a component normal to the surface is present in this sample system. Assuming that the field dependent component $S(\pm B)$ is mirrored under magnetic field reversal $S(+B) = -S(-B)$ one can extract the field dependent component S^{FD} using the same assumptions as previously for the S^{HD} and S^{HI} components (equation 6.8).
Figure 6.24 b) shows the amplitude of the field dependent component under the ro-

tation of the linear polarization direction of the pump beam for Bi_2Se_3/Al (red dots) and uncapped Bi_2Se_3 (grey squares). With the rotation of the waveplate no significant variations in the THz transient amplitudes are observed. However, clearly visible is the difference in the amplitudes between the two Bi_2Se_3 wedges. While the amplitudes for the Bi_2Se_3 wedge without capping show an amplitude of approximately 3 μV and are almost negligible the amplitudes for the Bi_2Se_3/Al wedge are approximately 7 μV and consequently higher by a factor of 2.

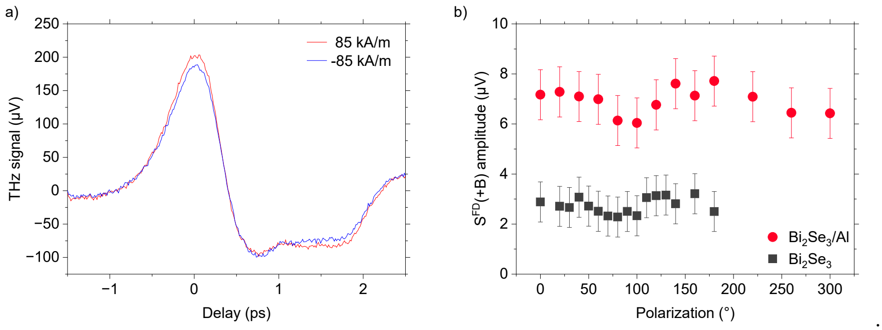

Fig. 6.24: a) THz transients measured in Bi_2Se_3/Al at a thickness of 70 nm for a reversed static magnetic field in the horizontal direction. b) Peak amplitudes of the field dependent component S^{FD} in Bi_2Se_3 without capping and Bi_2Se_3/Al as a function of the linear polarization direction of the pump beam.

6.4 Discussion

We have seen in the previous sections that the capping layer of 3 nm of Al has a strong influence on the THz emission from Bi_2Se_3. At specific thicknesses the THz transient amplitude in Bi_2Se_3/Al is strongly enhanced with respect to the Bi_2Se_3 wedge without capping. In quest of the underlying THz generation mechanisms one has to understand the differences of the two sample systems and the characteristic features of the observed THz radiation. Here, we will summarize and discuss our observations from the measurements shown above.

We have seen clear signatures that the THz generation mechanism is an interface/surface effect because of the influence of the Al layer. Our study shows that at a thickness of 16 nm the THz transient amplitudes in Bi_2Se_3/Al are 3.3 times higher with respect to the Bi_2Se_3 wedge without capping. Above 16 nm the THz amplitude in Bi_2Se_3/Al is decreasing, such that at ~24 nm both samples show similar THz transient amplitudes. Additionally, we observed a change in the THz transient shape for Bi_2Se_3/Al as a function of thickness between 20 and 24 nm under p-polarized excitation, as shown in Figure 6.11, which is not present in the Bi_2Se_3 wedge without capping. At 24 nm thickness, both amplitude and transient shape are similar for both Bi_2Se_3 bilayers. This suggests either the presence of an additional THz generation mechanism in Bi_2Se_3/Al, that vanishes when the thickness is above 24 nm or an effect that is much more pronounced in Bi_2Se_3/Al with respect to the non-capped Bi_2Se_3 wedge. It is very likely that we detect THz signals originating from different physical mechanisms as Bi_2Se_3 shows a variety of THz generation mechanisms. We have listed the most important in table 6.25.

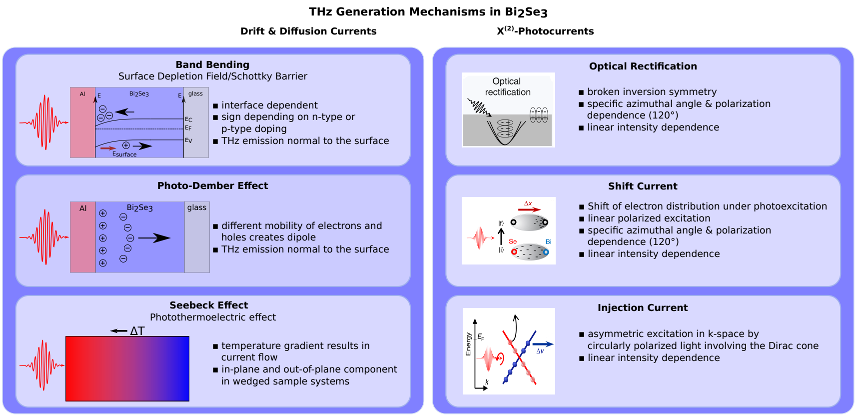

Fig. 6.25: THz generation mechanisms and signatures expected in Bi_2Se_3. Images are partly taken from references [164, 149].

The Raman spectra in Figure 6.7 showed that the surface of the Bi_2Se_3 sample without capping is oxidized. The oxidation of the first layers of Bi_2Se_3 leads to a formation of BiO and reduces the effective thickness of Bi_2Se_3. The influence of air exposure on freshly cleaved Bi_2Se_3 crystals was investigated previously by different studies and showed that it leads to the formation of a band bending at the surface that extends up to 20 nm into the bulk [163, 165]. The surface state was shown to shift down in energy into the occupied states with its distinctive properties unchanged [166, 161]. The Al capping layer has a thickness of 3 nm and we expect the Al layer to be completely oxidized. During the fabrication process of the wedges Bi_2Se_3 was exposed to air for a short time before the Al layer was deposited. We consequently expect also the interface in Bi_2Se_3/Al to be oxidized. A study by Hamh et al. [151] revealed that the band bending at an Bi_2Se_3/Al_2O_3 interface is 4x stronger compared to a Bi_2Se_3/air interface. The increase in strength of the band bending is comparable to the increased THz amplitude in the Bi_2Se_3/Al wedge with respect to the wedge without capping at 16 nm thickness. This suggests that the band bending at the interface may play a major role in the Bi_2Se_3 bilayers in the smaller thickness part of the wedge.
From the absorption coefficient in Figure 6.6 b) we see that the penetration depth of the laser at 10-25 nm is between 16 and 20 nm. With increasing thickness we consequently lose the sensitivity to the interface with the glass substrate. Similar as

for the top surface, studies of the band structure of Bi_2Se_3 interfaced with SiO_2 have shown that a band bending can be formed at the interface and the surface state at the interface was found to shift upward in energy [167, 168]. This implies that the expected band bending at the two interfaces of the Bi_2Se_3 bilayer is expected to be in opposite direction and the generated THz signals should consequently add up to an enhanced THz signal, see Figure 6.26. Therefore, each THz transient measured at a thickness step contains a contribution from the glass/Bi_2Se_3 interface $S^{\mathrm{THz,bottom}}$ and a contribution from the Bi_2Se_3/air, Bi_2Se_3/Al interface $S^{\mathrm{THz,top}}$, respectively. We see that the THz signal is strongly increasing at the small thicknesses, which we ascribe to the build up of the band bending at both interfaces. Once the Bi_2Se_3 layer reaches

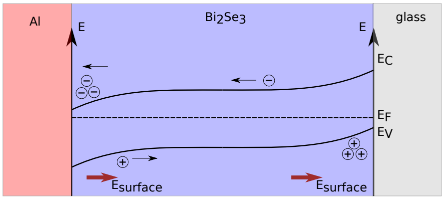

Fig. 6.26: Schematic illustration of the band bending at the top and bottom interface in Bi_2Se_3/Al. The downward band bending at the Al interface and the upward band bending at the SiO_2 yield a surface electric field in the same direction and consequently enhance the THz generation.

a thickness, where the band bending is fully developed, we do not expect a change in the THz transient amplitude $A^{\mathrm{THz,top}}$. However, the THz transient amplitude $A^{\mathrm{THz,bottom}}$, is decreasing with the thickness, because less light of the pump beam is able to penetrate into the Bi_2Se_3 and more and more of the THz signal is absorbed in the Bi_2Se_3 layer. We expect the behavior of $A^{\mathrm{THz,bottom}}$ as a function of the thickness to be the same in both Bi_2Se_3 bilayers. Interestingly, we observe that the start of the decrease in THz transient amplitude, which should be solely governed by the decrease in $A^{\mathrm{THz,bottom}}$ is occuring at different thicknesses for the uncapped Bi_2Se_3 bilayer and Bi_2Se_3/Al. This indicates that the build up of band bending and the resulting THz signal with increasing Bi_2Se_3 thickness occurs differently in the bilayers. We ascribe the change of THz transient shape in Bi_2Se_3/Al to the vanishing THz signal $S^{\mathrm{THz,bottom}}$. The minimal THz amplitude in the Bi_2Se_3 wedge without capping is $6\,\mu$V at 41 nm and smaller with respect to the Bi_2Se_3/Al wedge, where we observe the minimal THz transient amplitude at 26 nm with $28\,\mu$V. This agrees with the fact that no change in the THz transient shape is observed in the case of Bi_2Se_3 without capping as the signal is much smaller. The different position of the "dip" in THz transient amplitude for both samples can be attributed to the fact that the surface of the uncapped wedge is oxidized and the effective thickness of Bi_2Se_3 is smaller.

This implies that the build up of the band bending at the top and bottom interface is slower and the THz amplitude starts to decrease at larger thicknesses.

The main contributions of currents that are generated due to the surface depletion field are flowing normal to the surface or interface. In the measurement configuration the sensitive axis of the PCA detector was set in the vertical direction to measure the E_x component of the THz transient and no signal of out-of-plane currents is expected in this geometry. A rotation of the detection axis to the horizontal direction allowed to measure the E_y THz component, which is a combination of THz signals originated from in-plane and out-of-plane currents, see Figure 6.23. The measurements revealed that the amplitude of E_y in Bi_2Se_3/Al is stronger by a factor of two with respect to the Bi_2Se_3 without capping, which agrees with the observations made for the E_x-component and the influence of the band bending on THz generation. The amplitudes measured for E_x are higher with respect to E_y, but we expect the in-plane and out-of-plane signals to be of equal size in Bi_2Se_3 without capping. Because of the geometrical alignment of the generating dipole to the detection axis, the signal from the out-of-plane component will be smaller by a a factor of 2, as explained above. Both components, E_x and E_y, reveal a change in the THz transient amplitude, when the pump pulse polarization is changed from s to p. However, the E_y component showed a completely different transient shape for both polarization directions. We attribute this change to the presence of a signal from out-of-plane current contributions. A future investigation could show the disentanglement the $\vec{J}_\|$ and $\vec{J}_\perp$ component and investigate the dependence on the linear polarization axis by measuring a full rotation and a dependence on the azimuthal angle. Possible scenarios for a polarization dependent current could be optical rectification at the surface region or the shift current mechanism.

The THz generation mechanism for Bi_2Se_3 with small thicknesses was previously associated with the shift current mechanism, and a study by Wang et al. [147] presents a thickness dependence of THz amplitudes with a very similar trend to the one observed in this thesis. In the work by Wang et al. the Bi_2Se_3 layer was deposited on an Al_2O_3 substrate and capped by a SiO_2 layer to prevent surface oxidation. The shift current mechanism is based on a spatial shift of the electron distribution upon the photoexcitation between the initial and the excited state. In Bi_2Se_3 this was found to occur along the Bi-Se bonds, which hence manifests in a threefold symmetry [149]. The azimuthal angle dependence revealed a two-fold symmetry at 9, 15 and 41 nm thickness and one can conclude from this dependence that, even though the shift current mechanism might be present in this sample, it is not the dominating mechanism of THz generation in Bi_2Se_3/Al. Because the thickness gradient is below 1 nm/mm below 30 nm of Bi_2Se_3 thickness we rule out that the thickness gradient is playing a role for these part of the wedges. Nevertheless, also structural properties of Bi_2Se_3 are changing with the thickness. First, the grain size is smaller at the thinner part of the wedge and increases with the thickness (see Figure B.5 in the apendix). A smaller grain size will lead to higher electron scattering and shows an additional asymmetry along the wedge thickness, which could favor the electron flow along this direction. Second, thickness-dependent Raman spectra show a shift of the peak positions with increasing thickness. The position of the peak shifts to lower wavenumbers until a thickness of approximately 30 nm. Similar behavior was also found in reference [169] for the A^2_{1g} peak in Bi_2Se_3 and was ascribed to a change in the van der Waals forces between the layers as this mode refers to the out-of-plane vibrational modes. In our samples not only a change in the A^2_{1g} peak but additionally a red shift in the E^2_g is observed. The E^2_g peak refers to the in-plane mode and could indicate a change in the lattice parameters. These observations show that the varying thickness has a strong influence on the structural parameters of Bi_2Se_3 up to a thickness of ∼30 nm, even though the actual thickness gradient is small. We ascribe the in-plane asymmetry observed in the azimuthal angle dependence to a gradient in the physical properties of Bi_2Se_3.

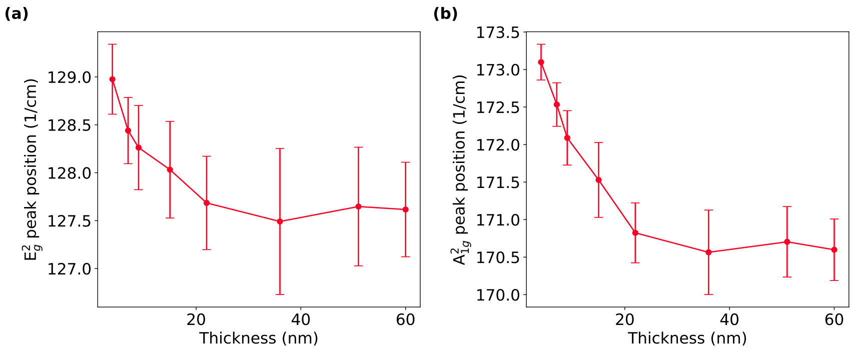

Fig. 6.27: Position of the E^2_g a) and A^2_{1g} Raman peak b) versus the thickness of Bi_2Se_3 in Bi_2Se_3/Al. Measurement performed by Kiryl A. Niherysh in the Department of Micotechnology and Nanoscience of the Chalmers University of Technology in Sweden.

At larger thicknesses of 70 nm, the increase of the amplitude in Bi_2Se_3/Al with respect to the Bi_2Se_3 wedge without capping is further enhanced and the amplitudes are 5x higher in Bi_2Se_3/Al. Although we expect that most of the excitations occur between the bulk bands, we can clearly see that the surface protection has an influence on the THz generation mechanism. The mechanism of THz generation shows a growth in strength with the thickness of the sample. As noted previously the increase in THz transient amplitude is not solely governed by an increase in absorption as the amplitude increase is stronger with respect to the increase in absorption.

In addition to the thickness of the Bi_2Se_3 wedge also the thickness gradient is increasing at the thicker part of the sample with values up to 2.6 nm/mm. The azimuthal angle dependence revealed a 2-fold symmetry with maxima at 0° and 180°, where the gradient was aligned in the vertical and parallel to the detection direction. This suggest that the thickness gradient may have a major influence on the THz generation mechanism in Bi_2Se_3 wedges. At the thicker part of the Bi_2Se_3, also the thickness gradient is larger and the contribution from the thickness gradient should be more pronounced. However, the azimuthal angle dependence shows this signature similarly at small thicknesses of approximately 9 nm, where the thickness gradient is only 0.3 nm/mm. The thickness gradient was found to play a decisive role for the generation of THz radiation in materials with good thermoelectric properties like Cd_3As_2 [170] and Bi_2Te_3 [171]. The efficiency of the conversion from heat to electricity is described by the figure of merit $ZT = S^2\sigma T/\kappa$, with the Seebeck coefficient S, the electrical conductivity σ, the temperature T and the thermal conductivity κ [172]. Literature shows a range of ZT values for the three materials Bi_2Se_3, Bi_2Te_3 and Cd_2As_3. The figure of merit in Bi_2Te_3 is larger with respect to the other two materials with $\sim$0.4 [98] but pristine Bi_2Se_3 and Cd_2As_3 show a comparable value for the figure of merit of approximately 0.1 [173, 147, 174, 175]. We consequently expect very similar efficiency of generation of currents by temperature gradients in Bi_2Se_3 as for Cd_2As_3.

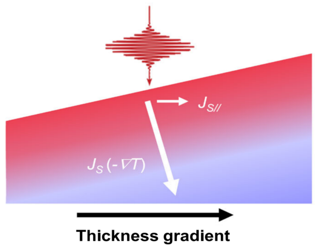

Fig. 6.28: Schematic illustration of the in-plane and out-of-plane currents generated under optical excitation of a sample with a thickness gradient. Taken from [170].

Until a Bi_2Se_3 thickness of 30 nm the gradient remains below 1 nm/mm and is consequently negligible. Above 30 nm the thickness gradient increases from 1 nm/mm up to 2.6 nm/mm and it becomes more likely to observe an influence of the thickness gradient on the THz generation process. The thickness gradient in reference [170] in Cd_3As_2 was 5 nm/mm and consequently by a factor of two higher than the largest thickness gradient in the Bi_2Se_3 wedges investigated in this thesis. Furthermore, the laser fluence used to excite Cd_3As_2 was between 0.2 - 0.8 mJ/cm^2 from a regenerative amplifier. The investigations of the Bi_2Se_3 wedges shown here are using a laser beam directly from the oscillator without any amplification stage and the laser fluence is much lower with 2.7 μJ/cm^2. We have used a two-temperature model (TTM) to investigate the temperature increase under fs-laser excication in Bi_2Se_3, see section B.5,

which shows that the temperature increases up to 100 K above room temperature in our experiments. This temperature increase is much lower compared to several hundreds of Kelvin that are expected in the Cd_3As_2 investigations. The principle of THz generation originating from temperature gradient due to a thickness gradient is shown in Figure 6.28. It shows two current contributions, one flowing normal to the surface and one in the surface plane. This agrees with the azimuthal angle dependence, where the maximum THz amplitude was observed along the THz gradient direction.
A comparison of THz generation of Bi_2Se_3 bilayers with constant thickness and wedged layers could help to understand the role of the thickness gradient in THz generation from Bi_2Se_3 bilayers. The anisotropy of the azimuthal dependence observed was ascribed to a measurement inaccuracy and a relative movement of the focused beam in the sample during the sample rotation. However, reports from Hamh et al. show that an inclined crystal plane is able to account for this anisotropy, which might be present also in the wedged Bi_2Se_3 sample systems [150]. Further x-ray diffraction experiments would be needed to investigate the inclination of the crystal planes with respect to each other and to exclude this possibility.

A clear signature of helicity dependent photocurrents is observed in both of the samples. From the measurement of the THz transients under the excitation with circularly polarized light with opposite helicity we obtain the pure S^{HD} and S^{HI} THz contributions. The S^{HD} is detected at thinner part of the Bi_2Se_3 wedges, where a maximum is observed around a thickness of 15 nm, as well as at the thicker part of the sample, where it shows an increase in amplitude with the thickness of Bi_2Se_3. The helicity dependent THz transient amplitudes in Bi_2Se_3/Al are higher by a factor of 4 with respect to the Bi_2Se_3 wedge without capping and we have shown that the helicity dependent signal vanishes under an almost normal incidence angle in the transmission geometry. In contrast to the HI component, which shows a 2-fold symmetry under rotation of the sample around its azimuth (as shown in Figure 6.20), the HD component is independent of the azimuthal angle orientation of the sample. At thicknesses above 35 nm our study shows an increase of the S^{HD} amplitudes with increasing thickness. In the experiment we have used a photon enerhy of 1.55 eV. The band gap of Bi_2Se_3 is approximately 300 meV and with the photon energy of 1.55 eV, intra band transitions from surface to bulk bands, bulk to surface bands and between different surface states occur, as shown in Figure 6.29. Due to the bulk inversion symmetry, no contribution to the helicity dependent THz signal is expected from transitions between the Bi_2Se_3 bulk states. We expect the helicity dependent photocurrents to originate at the surface/interface, which is supported by the higher THz transient amplitude in Bi_2Se_3/Al. We suggest two possible scenarios, which are based on the coupling of the angular momentum of circularly polarized light to the spin angular momentum of the electrons and yield a current flow with opposite direction depending on the light

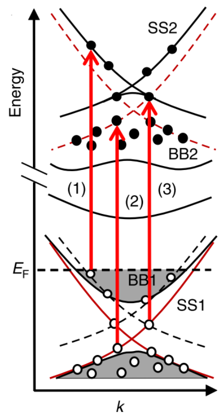

Fig. 6.29: Illustration of the bandstructure in Bi_2Se_3, where SS1 and SS1 are the first and second surface state and BB1 and BB2 stand for the bulk bands. The red arrows indicate the transitions under the optical excitation from surface to surface state, surface to bulk and bulk to surface state. Taken from [149].

helicity. The first effect is the asymmetric depopulation of the Dirac cone under the excitation with circularly polarized light [176, 177, 149], named circular photogalvanic effect (CPGE) and/or injection current. In the Dirac cone of Bi_2Se_3 surface states, the spin orientation is locked perpendicular to their momentum. As the circularly polarized light couples to the electrons with a spin orientation parallel to the angular momentum of the light, this results in a perpendicular dc current. The second effect is the Rashba-Edelstein effect, which is due to a Rashba-type spin-splitting at the interface. Several studies reveal the presence of a 2DEG with Rashba-type spin splitting at Bi_2Se_3 interfaces caused by the oxidation of the surface of Bi_2Se_3 [163, 166, 161] or adsorption of various atoms [178, 179], as well as the interaction of the two surface states at different surfaces in the very small thickness regime below 6 nm [123, 165]. The interaction of the two surface states opens a gap in the density of states and leads to the creation of the Rashba splitting. It was shown that this splitting can be controlled by the band bending at the surface.

In our case, the helicity dependent THz signal is observed from 5 to 25 nm thickness for Bi_2Se_3/Al, where the gap opening was found to vanish. We consequently do not expect the interaction of the Dirac cones from the different surfaces to play a role in the helicity dependent THz signals. However, we do not rule out other effects that could lead to a Rashba splitting. Both scenarios are supported by the observations made that S^{HD} is clearly visible at an angle of incidence of 45°, but vanishes in the transmission geometry and the fact that it is independent of the azimuthal angle orientation of the sample. We note again that the reflection and transmission geometry might not be exactly comparable and also other factors could lead to the vanishing of the signal.

The study by King et al.[165] showed that the Rashba-splitting can be controlled by the band bending at the surface through the adsorption of different atoms on the surface. The difference in the amplitudes of S^{HD} between the Bi_2Se_3 wedge without capping and Bi_2Se_3/Al by a factor of 4.5 could be explained by a different strength of the Rashba splitting. In experiments performed in a very similar geometry to the reflection geometry shown in Figure 3.1 b) showed no helicity dependent photocurrent [149]. In the study the Bi_2Se_3 showed a constant thickness of approximately 0.3 mm. The authors point out several reasons for the negligible HD component including a higher matrix element for excitations from bulk to bulk bands, however more important the cancellation of currents considering only excitations from the Dirac cone. This suggest that the thickness gradient could play a role for a helicity-dependent THz generation by introducing an additional asymmetry. This would agree with the fact, that the amplitude of $S^{\mathrm{HD}}$is growing with the thickness gradient in Bi_2Se_3.

In conclusion we have shown the influence of 3 nm Al layer on a Bi_2Se_3 wedge with a thickness ranging from 5 to 70 nm. We showed that the additional Al layer enhances the THz emission signal at approximately 16 nm by a factor 4 and at around 70 nm by a factor 5. We therefore locate the THz generation mechanism at the surface of Bi_2Se_3 and found that at thicknesses below 40 nm in the Bi_2Se_3 without capping and below 26 nm in Bi_2Se_3/Al two THz contributions originated from the top and bottom surface of Bi_2Se_3 are present. We ascribe the THz generation mechanism to the band bending at the interface of Bi_2Se_3, which is stronger in the case of Bi_2Se_3/Al. We have found in-plane currents flowing along the direction of the thickness gradient, which most likely to be caused by structural gradients in the thinner part of the sample and thickness gradient at the thicker part of the wedges, where the highest gradient is located. We showed the presence of a helicity-dependent THz signal, not only for thicknesses below 15 nm, but also at thicknesses above 30 nm, which we ascribe to contributions from the Dirac cone and Rashba splitting at the surface. However a detailed study and of band structure and THz generation in samples with and without gradient is needed for clarification.

Chapter 7

Conclusion and outlook

The primary objective of this thesis was to investigate, analyze, and understand the fundamental principles of spin current generation and spin-to-charge current conversion at the ultrafast timescale. Our research not only contributes to the advancement of ultrafast spintronic devices, but also has practical implications for the performance enhancement of THz spintronic emitters. This thesis was divided into three parts, each focusing on a specific material set. Through a comprehensive study of these sample sets, we were able to identify key factors that determine the THz transient amplitude and, consequently, the efficiency of spin-to-charge conversion.

In the first part, we focused on an FM/NM heterostructure and showed the fundamental mechanism and properties of THz radiation from spintronic emitters, where the generation mechanism is the inverse spin Hall effect. We chose the FM material to be a $Ni_{80}Fe_{20}$ alloy capped with 2 nm of Pt and Pd, exhibiting high spin-orbit coupling. The polarity of the THz generation is dependent on the alignment of the magnetic field with respect to the sample structure. Both rotating the sample by 180° in the horizontal plane and changing the direction of the magnetic field are able to invert the THz polarity. Not only the polarity but also the amplitude can be tuned by the magnetic field. We show that the THz transient amplitude follows the magnetic field of the ferromagnetic material. The investigations of samples with different NM layer materials showed that spin-orbit coupling is a decisive parameter that enhances the efficiency of spin-to-charge conversion and leads to a higher THz transient amplitude.

In the second part of this thesis, the ferromagnetic layer in the heterostructures is set as CFMS Heusler alloy. The CFMS Heusler alloy is a half metal, which is favorable in spin transport experiments as it is expected to show a 100% spin polarization at the Fermi level. The nonmagnetic layers Pt and Ta were chosen for their high spin-orbit coupling and compared with Al and Cr. We demonstrate that the THz generation mechanism is the inverse spin Hall effect, as the THz transient amplitude and polarity are tunable by the magnetic field direction and amplitude. The efficiency of spin-to-charge conversion, hence the spin Hall angle, is expected to scale with the spin-orbit

coupling of the material. Interestingly, a 3x lower amplitude in the case of Ta and a two orders of magnitude higher amplitude, as expected in the case of Al, were observed. Additional investigations using XRR, XANES, and XMCD to investigate the oxidation of the samples and the interfaces revealed that the thickness of the NM layer, as well as the FM/NM interface, plays a decisive role in the THz generation mechanism. We observed that the Ta layer is oxidized, substantially reducing its effective thickness and consequently reducing the generated THz transient amplitude. The XCMD results revealed interdiffusion of Al atoms into the CFMS layer and we consequently attribute the increased THz transient amplitude to interfacial skew scattering.
The investigations demonstrate the importance of material choice and properties of interface and layer structure on the efficiency of THz generation via spin-to-charge conversion. We showed that a high spin-orbit coupling dominates the efficiency of THz generation via the inverse spin Hall effect in FM/NM heterostructures. On the contrary we found the oxidation of the layers to have a negative impact on the THz generation process. However, we found interdiffusion at the FM/NM interface to be beneficial due to interfacial skew scattering. A dedicated study of interface effects on THz generation could gain further understanding of the interface properties and the interplay of inverse spin Hall effect and additional skew scattering at the interface. Tuning the amount of interdiffusion and thickness of the diffusion layer are interesting parameters for future investigations.

In the third part of this thesis, we investigated a topological insulator Bi_2Se_3 as a sample system, with a varying thickness from 5 to 70 nm. We compared the THz radiation generated in two different samples, where has been left without any surface protection layer, and the other has been capped with 3 nm of Al. Literature shows various effects occurring in the Bi_2Se_3 that generate THz radiation. We ascribed the THz mechanism to an interface and surface effect, as we observed a strong increase of the THz transient amplitude in Bi_2Se_3/Al with respect to the Bi_2Se_3 wedge without capping at specific thicknesses. Due to the strength of the increase, we suggest the band bending to play a key role in the THz generation mechanism. Interestingly, we found an in-plane asymmetry in both samples, present over the entire thickness range. The maximal amplitudes are found along the axis of the thickness gradient. The change in thickness and thickness gradient also leads to a gradient in structural properties of Bi_2Se_3, for example, the grain size. We suggest changes in the structural properties play a significant role in the thinner part of the wedge because we observe strong changes of lattice parameters until a thickness of approximately 30 nm, which agrees with the thickness, where the THz amplitude decreases in both samples. At the thicker part, where the gradient grows, we expect the thickness gradient become of importance in the generation of THz radiation. In addition, the thick part of the sample (>35 nm) also showed strong helicity-dependent signals, which we ascribe to the presence of a Rashba-splitting or excitation from the Dirac cone. Our study shows the importance of a careful analysis of the interface for THz investigations from Bi_2Se_3. Band structure investigations using ARPES are helpful in understanding the surface configurations. To exclude and confirm entanglements of effects with the thickness gradient, an investigation of a constant-thickness Bi_2Se_3 sample could be insightful. The investigations show that Bi_2Se_3 has a great potential to be used as a THz emitter and is very versatile in the originating current generation mechanisms. By tuning the interfaces and sample geometry, different strength and polarization in THz generation can be achieved. These findings show that various key factors impact the generation of THz radiation and can be tuned in many different ways. It shows the possibility of building THz sources with distinct properties but demonstrates the importance of controlling the sample characteristics carefully.

Appendices

Appendix A

THz Generation in Heusler alloy/heavy metal bilayers

A.1 Ferromagnetic resonance in CFMS/NM bilayers

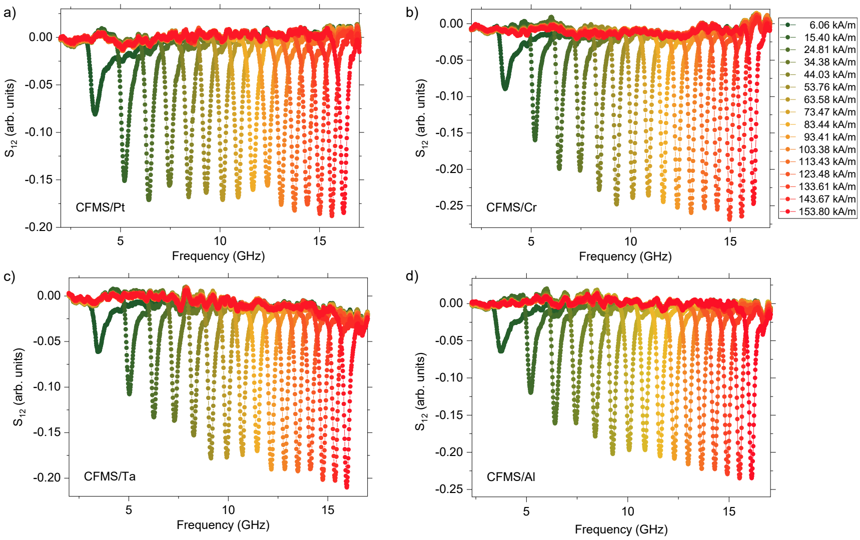

Fig. A.1: Frequency sweeps up to 17 GHz of the absorption of the rf signal after transmission of the CPW waveguide, characterized by the S_{12} parameter, at various static magnetic field steps ranging from 6 kA/m to 150 kA/m for a) CFMS/Pt, b) CFMS/Cr, c) CFMS/Ta and d) CFMS/Al.

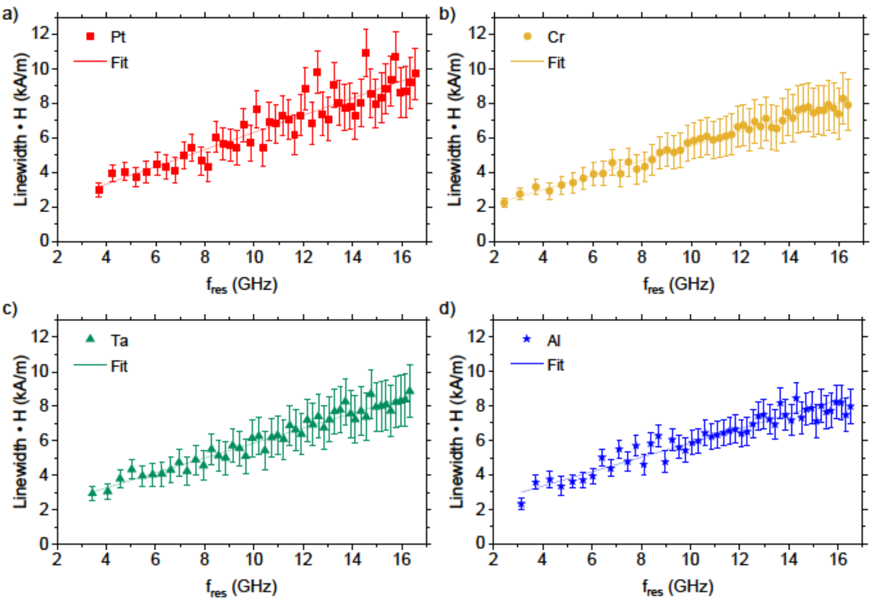

Fig. A.2: Frequency sweeps up to 17 GHz of the absorption of the rf signal after transmission of the CPW waveguide, characterized by the S_{12} parameter, at various static magnetic field steps ranging from 6 kA/m to 150 kA/m for a) CFMS/Pt, b) CFMS/Cr, c) CFMS/Ta and d) CFMS/Al.

A.2 XRR of CFMS/NM bilayers

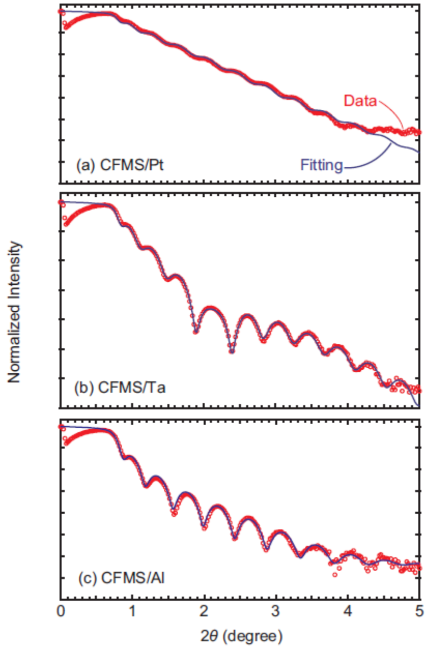

Fig. A.3: XRR results (red) and fits (blue) for (a) CFMS/Pt, (b)CFMS/Ta-TaO, and (c) CFMS/Al-AlO layer systems. The fit were done with the software GlobalFit by Rigaku Corp [180, 181]. Measurements were performed in the group of Koki Takanashi (Institute for Materials Research, Tohoku University, Sendai, Japan)

Appendix B

THz generation in topological insulator Bi_2Se_3

B.1 Thickness dependent THz transients Bi_2Se_3

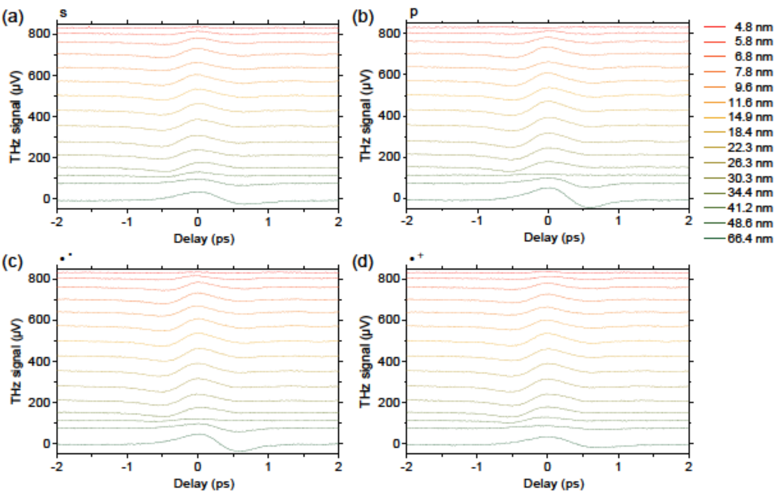

Fig. B.1: Thickness dependent THz transients for a pristine Bi_2Se_3 sample in the range between 4 and 67 nm. THz transients shown are generated by a (a) s-polarized (b) p-polarized (c) left circular polarized and (d) right circular polarized pump beam.

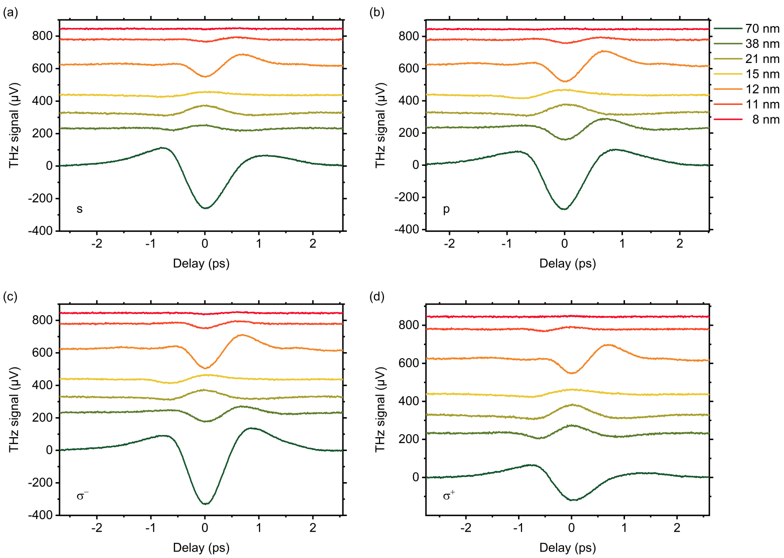

Fig. B.2: Thickness dependent THz transients for a Bi_2Se_3/Al sample in the range between 8 and 70 nm. THz transients shown are generated by a (a) s-polarized (b) p-polarized (c) left circular polarized and (d) right circular polarized pump beam.

B.2 Circularly polarized excitation Bi_2Se_3

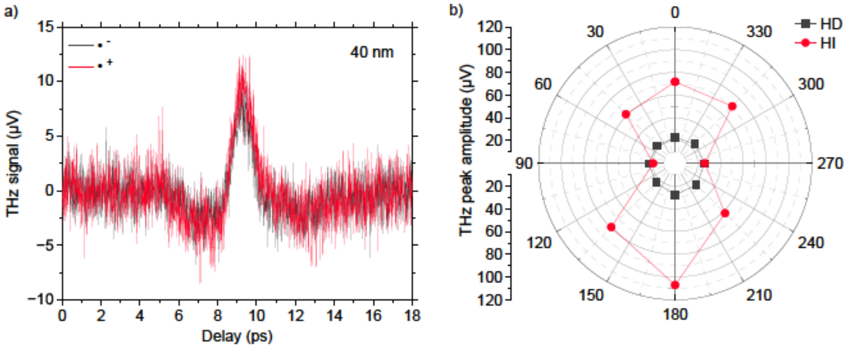

Fig. B.3: a) THz transients obtained under excitation with circular polarized light in the transmission geometry, hence an incidence angle of approximately 5° at 40 nm thickness of Bi_2Se_3 in the pristine sample. b) THz peak amplitudes of the extracted HD and HI component at 41 nm thickness in Bi_2Se_3/Al under the rotation of the sample around its azimuth. The lines are only a guide for the eye.

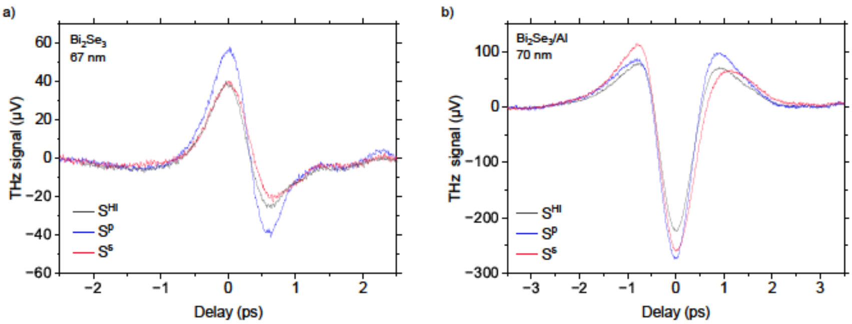

Fig. B.4: Comparison of THz transients obtained under excitation with p-polarized light (blue), s-polarized light (red) and extracted S^{HI} component from the excitation with circularly polarized light (grey) for Bi_2Se_3 without capping at 67 nm in a) and Bi_2Se_3/Al at 70 nm in b).

B.3 Grain size of Bi_2Se_3 from AFM measurements

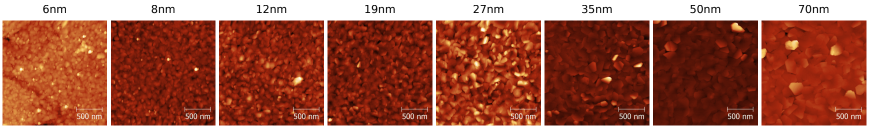

Fig. B.5: AFM images of Bi_2Se_3 at different thickness positions showing the difference in the grain size. Measurement performed by Kiryl A. Niherysh in the Department of Micotechnology and Nanoscience of the Chalmers University of Technology in Sweden.

B.4 Refractive index and extinction coefficient in Bi_2Se_3

From the absorption and reflectivity data we calculate the extinction coefficient $k = \frac{\alpha\lambda}{4\pi}$ and the refractive index via the Fresnel equations [182]:

$$R_s = |\frac{n_i cos(\theta_i) - n_t cos(\theta_t)}{n_i cos(\theta_i) - n_t cos(\theta_t)}|^2 \tag{B.1}$$

$$R_p = |\frac{n_i cos(\theta_t) - n_t cos(\theta_i)}{n_i cos(\theta_t) - n_t cos(\theta_i)}|^2 \ , \tag{B.2}$$

with n_i and θ_i being the refractive index of air and the incidence angle and n_t and θ_t the refractive index of Bi_2Se_3 and the refraction angle. Because the measurement was done under an incidence angle of 45° we perform an iterative method to calculate the thickness dependent refractive index of the Bi_2Se_3 wedge.

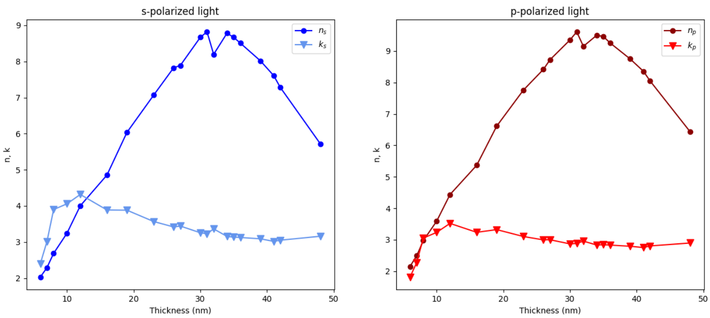

Fig. B.6: Thickness dependent refractive index n and extinction coefficient k of Bi_2Se_3 for the illumination with s-polarized light in a) and p-polarized light in b).

ρ	$7510\,\mathrm{kg/m^3}$
k_el	$0.4\,\mathrm{W/(m{\cdot}K)}$
C_{el}	$10\,\mathrm{J/(m^3K^2)}{\cdot}T_e$
C_L	$200\,\mathrm{J/(kg{\cdot}K)}$
Θ_{Debye}	$180\,\mathrm{K}$
G_{el-L}	$1.4{\cdot}10^{16}\,\mathrm{J/(m^3Ks)}$

Table B.1: Literature values for the TTM simulation from reference [183].

B.5 Temperature rise under fs-excitation in Bi_2Se_3

In the following we would like to evaluate on the temperature rise in the Bi_2Se_3 wedges under the absorption process of the fs-laser pulse. Under the absorption process the electron temperature rises on a very short femtosecond timescale above several hundreds of Kelvin [21, 31] leading to a temperature gradient from the center of the laser illuminated area outwards. This temperature gradient was found to be the important driving force of currents under the excitation with short laser pulses, as demonstrated in chapter 2.3.2. In an isotropic material all of the current contributions would cancel out as the electrons are flowing into all directions. Due to additional asymmetries, e.g., the sample surface, non-cancelling current contributions remain and can be detected as THz radiation.

We have used the Two-Temperature Model (TTM), describing the temperatures of the electronic system T_e and the phonon temperature T_L, by two independent but coupled differential equations [183]:

$$C_\mathrm{e}\frac{\mathrm{d}}{\mathrm{d}t}T_\mathrm{e} = \frac{(1-R)\cdot F\cdot I(t)\cdot\exp(-z/d)}{d} - U_\text{e-ph}(T_\mathrm{e},T_\mathrm{L}) \tag{B.3}$$

$$C_\mathrm{L}\frac{\mathrm{d}}{\mathrm{d}t}T_\mathrm{L} = -C_\mathrm{L}D\frac{\mathrm{d}}{\mathrm{d}z^2}T_\mathrm{L} + U_\text{e-ph}(T_\mathrm{e},T_\mathrm{L})\ , \tag{B.4}$$

where the coupling between the two equations is given by the term $U_\text{e-ph}(T_\mathrm{e},T_\mathrm{L})$. The parameters C_e and C_L are the heat capacity of the electron system and the lattice, respectively, where C_e can be written as $C_\mathrm{e} = \gamma_\mathrm{e}T_\mathrm{e}$ using the electron specific heat coefficient γ_e. The first term on the right side of the first equation describes the increase of temperature due to the absorption of the laser pulse, with the fluence F and the intensity profile $I(t)$. R is the reflectivity of the sample, d the penetration depth and $\exp(-z/d)$ describes the thickness dependent absorption by the Lambert-Beer law. In the second equation D is thermal diffusion coefficient. To solve the TTM we use the N-temperature model solver NTMpy from the Ultrafast Dynamics in Condensed Matter group at Stockholm University and at the Ca' Foscari University of Venice [184]. Figure B.7 a) shows the temporal evolution of the two subsystem temperatures T_e and T_L. The laser pulse impinges on the sample at $t = 0\,\mathrm{s}$ and the electron temperature starts to increase as shown in red up to approximately 400 K at a thickness of 16 nm, which is consequently 100 K above room temperature. The inset shows a magnification of the lattice temperature increase, which increases by less then 0.5 K. In b) we show the maximal reached electron temperature T_e over the Bi_2Se_3 wedge. Up to 20 nm the T_e rises up to 380-400 K, while above 30 nm the increase is only half up to 340 K. For the simulation we take into account the complex refractive index shown in Figure B.6 and the thickness of the Bi_2Se_3 wedge. Additionally we take some values from literature, which are summarized in table B.1. The laser pulse energy in our experiment was 2.7 μJ/cm^2, which is not able to increase the temperature of the electron system more than 100 K above the initial temperature.

(a)

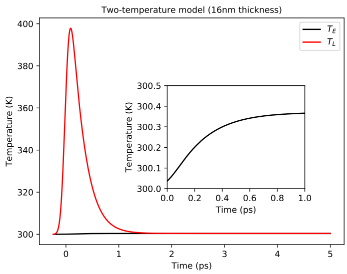

(b)

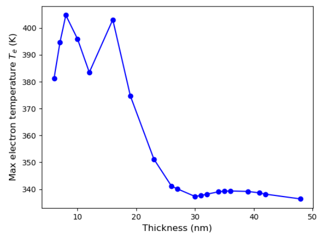

Fig. B.7: Simulation electron temperature and lattice temperature with the two-temperature model (2TM) using the code from NTM reference [184]. a) Time-dependent electron T_e and lattice temperature T_L under the absorption of the fs-laser pulse. The inset shows the increase of the lattice temperature. b) Thickness-dependent maximal electron temperature from the simulation shown in a).

Bibliography

[1] Priti J. Rajput, Sheetal U. Bhandari, and Girish Wadhwa. “A Review on—Spintronics an Emerging Technology”. In: *Silicon* 14.15 (2022), pp. 9195–9210. ISSN: 1876-9918. DOI: 10.1007/s12633-021-01643-x.

[2] Atsufumi Hirohata et al. “Review on spintronics: Principles and device applications”. In: *Journal of Magnetism and Magnetic Materials* 509 (2020), p. 166711. ISSN: 0304-8853. DOI: https://doi.org/10.1016/j.jmmm.2020.166711.

[3] G. Binasch et al. “Enhanced magnetoresistance in layered magnetic structures with antiferromagnetic interlayer exchange”. In: *Physical Review B* 39.7 (1989). PRB, pp. 4828–4830. DOI: 10.1103/PhysRevB.39.4828.

[4] M. N. Baibich et al. “Giant Magnetoresistance of (001)Fe/(001)Cr Magnetic Superlattices”. In: *Physical Review Letters* 61.21 (1988). PRL, pp. 2472–2475. DOI: 10.1103/PhysRevLett.61.2472.

[5] B. Dieny et al. “Opportunities and challenges for spintronics in the microelectronics industry”. In: *Nature Electronics* 3.8 (2020), pp. 446–459. ISSN: 2520-1131. DOI: 10.1038/s41928-020-0461-5.

[6] D. Apalkov, B. Dieny, and J. M. Slaughter. “Magnetoresistive Random Access Memory”. In: *Proceedings of the IEEE* 104.10 (2016), pp. 1796–1830. ISSN: 1558-2256. DOI: 10.1109/JPROC.2016.2590142.

[7] A. V. Chumak et al. “Magnon spintronics”. In: *Nature Physics* 11.6 (2015), pp. 453–461. ISSN: 1745-2481. DOI: 10.1038/nphys3347.

[8] Everspin Technologies Inc. Web Page.

[9] D. C. Worledge. “Spin-Transfer-Torque MRAM: the Next Revolution in Memory”. In: *2022 IEEE International Memory Workshop (IMW)*, pp. 1–4. ISBN: 2573-7503. DOI: 10.1109/IMW52921.2022.9779288.

[10] Luqiao Liu et al. “Spin-Torque Switching with the Giant Spin Hall Effect of Tantalum”. In: *Science* 336.6081 (2012), pp. 555–558. DOI: doi:10.1126/science.1218197.

[11] J. E. Hirsch. “Spin Hall Effect”. In: *Physical Review Letters* 83.9 (1999). PRL, pp. 1834–1837. DOI: 10.1103/PhysRevLett.83.1834.

[12] A. Hoffmann. "Spin Hall Effects in Metals". In: *IEEE Transactions on Magnetics* 49.10 (2013), pp. 5172–5193. ISSN: 1941-0069. DOI: 10.1109/TMAG.2013.2262947.

[13] S. D. Ganichev et al. "Spin-galvanic effect". In: *Nature* 417.6885 (2002), pp. 153–156. ISSN: 1476-4687. DOI: 10.1038/417153a.

[14] J. C. Rojas Sánchez et al. "Spin-to-charge conversion using Rashba coupling at the interface between non-magnetic materials". In: *Nature Communications* 4.1 (2013), p. 2944. ISSN: 2041-1723. DOI: 10.1038/ncomms3944.

[15] E. Y. Vedmedenko et al. "The 2020 magnetism roadmap". In: *Journal of Physics D: Applied Physics* 53.45 (2020), p. 453001. ISSN: 0022-3727. DOI: 10.1088/1361-6463/ab9d98.

[16] Atsufumi Hirohata et al. "Roadmap for Emerging Magnetic Materials for Spintronic Device Applications". In: *Magnetics, IEEE Transactions on* PP (2015), pp. 1–1. DOI: 10.1109/TMAG.2015.2457393.

[17] Ethan C. Ahn. "2D materials for spintronic devices". In: *npj 2D Materials and Applications* 4.1 (2020), p. 17. ISSN: 2397-7132. DOI: 10.1038/s41699-020-0152-0.

[18] Mengyun He, Huimin Sun, and Qing Lin He. "Topological insulator: Spintronics and quantum computations". In: *Frontiers of Physics* 14.4 (2019), p. 43401. ISSN: 2095-0470. DOI: 10.1007/s11467-019-0893-4.

[19] Qing Lin He et al. "Topological spintronics and magnetoelectronics". In: *Nature Materials* 21.1 (2022), pp. 15–23. ISSN: 1476-4660. DOI: 10.1038/s41563-021-01138-5.

[20] National Institute of Information Technology and Communications. Web Page.

[21] E. Beaurepaire et al. "Ultrafast Spin Dynamics in Ferromagnetic Nickel". In: *Physical Review Letters* 76.22 (1996). PRL, pp. 4250–4253. DOI: 10.1103/PhysRevLett.76.4250.

[22] Jakob Walowski and Markus Münzenberg. "Perspective: Ultrafast magnetism and THz spintronics". In: *Journal of Applied Physics* 120.14 (2016), p. 140901. DOI: 10.1063/1.4958846.

[23] T. Kampfrath et al. "Terahertz spin current pulses controlled by magnetic heterostructures". In: *Nature Nanotechnology* 8.4 (2013), pp. 256–260. ISSN: 1748-3395. DOI: 10.1038/nnano.2013.43.

[24] Tom S. Seifert et al. "Femtosecond formation dynamics of the spin Seebeck effect revealed by terahertz spectroscopy". In: *Nature Communications* 9.1 (2018), p. 2899. ISSN: 2041-1723. DOI: 10.1038/s41467-018-05135-2.

[25] Erik Bründermann, Heinz-Wilhelm Hübers, and Maurice F. Kimmitt. “Terahertz Techniques”. In: *Terahertz Techniques*. Berlin, Heidelberg: Springer Berlin Heidelberg, 2012. ISBN: 978-3-642-02592-1. DOI: `10.1007/978-3-642-02592-1_1`.

[26] T. Seifert et al. “Efficient metallic spintronic emitters of ultrabroadband terahertz radiation”. In: *Nature Photonics* 10 (2016), p. 483. DOI: `10.1038/nphoton.2016.91https://www.nature.com/articles/nphoton.2016.91#supplementary-information`.

[27] Philip F. Taday, Michael Pepper, and Donald D. Arnone. “Selected Applications of Terahertz Pulses in Medicine and Industry”. In: *Applied Sciences* 12.12 (2022), p. 6169. ISSN: 2076-3417.

[28] Benjamin Balke et al. “Properties of the quaternary half-metal-type Heusler alloy $Co_2Mn_{1-x}Fe_xSi$”. In: *Physical Review B* 74.10 (2006). PRB, p. 104405. DOI: `10.1103/PhysRevB.74.104405`.

[29] Braj Bhusan Singh et al. *High spin mixing conductance and spin interface transparency at Co2Fe0.4Mn0.6Si Heusler alloy and Pt interface*. Electronic Article. Nov. 2019.

[30] Jiahao Han and Luqiao Liu. “Topological insulators for efficient spin–orbit torques”. In: *APL Materials* 9.6 (2021). ISSN: 2166-532X. DOI: `10.1063/5.0048619`.

[31] Joachim Stoehr and Hans Christoph Siegmann. “Magnetism : from fundamentals to nanoscale dynamics”. In: (2006). ISSN: 3540302832 9783540302834.

[32] Mathias Getzlaff. *Fundamentals of magnetism*. 2010. ISBN: 9783540311508.

[33] C. M. Schneider and J. Kirschner. “Chapter 9 - Magnetism at Surfaces and in Ultrathin Films”. In: *Handbook of Surface Science*. Ed. by K. Horn and M. Scheffler. Vol. 2. North-Holland, 2000, pp. 511–668. ISBN: 15734331. DOI: `https://doi.org/10.1016/S1573-4331(00)80013-X`.

[34] Frances Hellman et al. “Interface-induced phenomena in magnetism”. In: *Reviews of Modern Physics* 89.2 (2017). RMP, p. 025006. DOI: `10.1103/RevModPhys.89.025006`.

[35] Stephen Blundell. *Magnetism in condensed matter*. Includes bibliographical references and index. Oxford ; New York : Oxford University Press, 2001., 2001.

[36] Daniel E. Buergler. “Memristive Phenomena - From Fundamental Physics to Neuromorphic Computing”. In: *IFF Springschool*. Ed. by Matthias Wuttig Rainer Waser. Vol. 113. Forschungszentrum Jülich GmbH.

[37] K. V. Shanavas, Z. S. Popović, and S. Satpathy. "Theoretical model for Rashba spin-orbit interaction in *d* electrons". In: *Physical Review B* 90.16 (2014). PRB, p. 165108. DOI: 10.1103/PhysRevB.90.165108.

[38] Frank Skillman Sherwood Herman. *Atomic structure calculations*. Englewood Cliffs, N.J.: Prentice-Hall, 1963.

[39] N. F. Mott. "The Electrical Conductivity of Transition Metals". In: *Proceedings of the Royal Society of London Series A* 153 (1936), pp. 699–717. ISSN: 0080-46301364-5021. DOI: 10.1098/rspa.1936.0031.

[40] Xiaoguang Zhang and William Butler. "Theory of Giant Magnetoresistance and Tunneling Magnetoresistance". In: 2016, pp. 3–69. ISBN: 978-94-007-6891-8. DOI: 10.1007/978-94-007-6892-5_2.

[41] Jack Bass and William P. Pratt. "Spin-diffusion lengths in metals and alloys, and spin-flipping at metal/metal interfaces: an experimentalist's critical review". In: *Journal of Physics: Condensed Matter* 19.18 (2007), p. 183201. ISSN: 0953-8984 1361-648X. DOI: 10.1088/0953-8984/19/18/183201.

[42] Saburo Takahashi. "Physical Principles of Spin Pumping". In: *Handbook of Spintronics*. Ed. by Yongbing Xu, David D. Awschalom, and Junsaku Nitta. Dordrecht: Springer Netherlands, 2016, pp. 1445–1480. ISBN: 978-94-007-6892-5. DOI: 10.1007/978-94-007-6892-5_51.

[43] K. Ando et al. "Inverse spin-Hall effect induced by spin pumping in metallic system". In: *Journal of Applied Physics* 109.10 (2011), p. 103913. DOI: 10.1063/1.3587173.

[44] T. L. Gilbert. "A phenomenological theory of damping in ferromagnetic materials". In: *IEEE Transactions on Magnetics* 40.6 (2004), pp. 3443–3449. ISSN: 1941-0069. DOI: 10.1109/TMAG.2004.836740.

[45] Charles Kittel. "On the Theory of Ferromagnetic Resonance Absorption". In: *Physical Review* 73.2 (1948). PR, pp. 155–161. DOI: 10.1103/PhysRev.73.155.

[46] K. Carva, M. Battiato, and P. M. Oppeneer. "Ab Initio Investigation of the Elliott-Yafet Electron-Phonon Mechanism in Laser-Induced Ultrafast Demagnetization". In: *Physical Review Letters* 107.20 (2011). PRL, p. 207201. DOI: 10.1103/PhysRevLett.107.207201.

[47] B. Koopmans et al. "Explaining the paradoxical diversity of ultrafast laser-induced demagnetization". In: *Nature Materials* 9.3 (2010), pp. 259–265. ISSN: 1476-4660. DOI: 10.1038/nmat2593.

[48] A. B. Schmidt et al. "Ultrafast Magnon Generation in an Fe Film on Cu(100)". In: *Physical Review Letters* 105.19 (2010). PRL, p. 197401. DOI: 10.1103/PhysRevLett.105.197401.

[49] C. Dornes et al. "The ultrafast Einstein–de Haas effect". In: *Nature* 565.7738 (2019), pp. 209–212. ISSN: 1476-4687. DOI: 10.1038/s41586-018-0822-7.

[50] M. Battiato, K. Carva, and P. M. Oppeneer. "Superdiffusive Spin Transport as a Mechanism of Ultrafast Demagnetization". In: *Physical Review Letters* 105.2 (2010). PRL, p. 027203. DOI: 10.1103/PhysRevLett.105.027203.

[51] Emrah Turgut et al. "Controlling the Competition between Optically Induced Ultrafast Spin-Flip Scattering and Spin Transport in Magnetic Multilayers". In: *Physical Review Letters* 110.19 (2013). PRL, p. 197201. DOI: 10.1103/PhysRevLett.110.197201.

[52] G. Malinowski et al. "Control of speed and efficiency of ultrafast demagnetization by direct transfer of spin angular momentum". In: *Nature Physics* 4.11 (2008), pp. 855–858. ISSN: 1745-2481. DOI: 10.1038/nphys1092.

[53] Dennis Rudolf et al. "Ultrafast magnetization enhancement in metallic multilayers driven by superdiffusive spin current". In: *Nature Communications* 3.1 (2012), p. 1037. ISSN: 2041-1723. DOI: 10.1038/ncomms2029.

[54] V. P. Zhukov, E. V. Chulkov, and P. M. Echenique. "Lifetimes and inelastic mean free path of low-energy excited electrons in Fe, Ni, Pt, and Au: Ab initio GW + T calculations". In: *Physical Review B* 73.12 (2006). PRB, p. 125105. DOI: 10.1103/PhysRevB.73.125105.

[55] Ralf Metzler and Joseph Klafter. "The random walk's guide to anomalous diffusion: a fractional dynamics approach". In: *Physics Reports* 339.1 (2000), pp. 1–77. ISSN: 0370-1573. DOI: https://doi.org/10.1016/S0370-1573(00)00070-3.

[56] A. Fognini et al. "Laser-induced ultrafast spin current pulses: a thermodynamic approach". In: *Journal of Physics: Condensed Matter* 29.21 (2017), p. 214002. ISSN: 0953-8984 1361-648X. DOI: 10.1088/1361-648x/aa6a76.

[57] Gerrit E. W. Bauer, Eiji Saitoh, and Bart J. van Wees. "Spin caloritronics". In: *Nature Materials* 11.5 (2012), pp. 391–399. ISSN: 1476-4660. DOI: 10.1038/nmat3301.

[58] E. H. Hall. "On a New Action of the Magnet on Electric Currents". In: *American Journal of Mathematics* 2.3 (1879), pp. 287–292. ISSN: 00029327, 10806377. DOI: 10.2307/2369245.

[59] E. H. Hall. "XVIII. On the "Rotational Coefficient" in nickel and cobalt". In: *The London, Edinburgh, and Dublin Philosophical Magazine and Journal of Science* 12.74 (1881), pp. 157–172. ISSN: 1941-5982. DOI: 10.1080/14786448108627086.

[60] C. Hurd. *The Hall Effect in Metals and Alloys*. Springer US, 2012. ISBN: 9781475704655.

[61] Robert Karplus and J. M. Luttinger. “Hall Effect in Ferromagnetics”. In: *Physical Review* 95.5 (1954). PR, pp. 1154–1160. DOI: 10.1103/PhysRev.95.1154.

[62] J. Smit. “The spontaneous hall effect in ferromagnetics II”. In: *Physica* 24.1 (1958), pp. 39–51. ISSN: 0031-8914. DOI: https://doi.org/10.1016/S0031-8914(58)93541-9.

[63] L. Berger. “Side-Jump Mechanism for the Hall Effect of Ferromagnets”. In: *Physical Review B* 2.11 (1970). PRB, pp. 4559–4566. DOI: 10.1103/PhysRevB.2.4559.

[64] M. Dyakonov and V. I. PereŒ. “Possibility of Orienting Electron Spins with Current”. In.

[65] M. I. Dyakonov and V. I. Perel. “Current-induced spin orientation of electrons in semiconductors”. In: *Physics Letters A* 35.6 (1971), pp. 459–460. ISSN: 0375-9601. DOI: https://doi.org/10.1016/0375-9601(71)90196-4.

[66] Yuichiro Kato et al. “Observation of the Spin Hall Effect in Semiconductors”. In: *Science (New York, N.Y.)* 306 (2004), pp. 1910–3. DOI: 10.1126/science.1105514.

[67] J. Wunderlich et al. “Experimental Observation of the Spin-Hall Effect in a Two-Dimensional Spin-Orbit Coupled Semiconductor System”. In: *Physical Review Letters* 94.4 (2005). PRL, p. 047204. DOI: 10.1103/PhysRevLett.94.047204.

[68] M. I. Dyakonov. “Magnetoresistance due to Edge Spin Accumulation”. In: *Physical Review Letters* 99.12 (2007). PRL, p. 126601. DOI: 10.1103/PhysRevLett.99.126601.

[69] Naoto Nagaosa et al. “Anomalous Hall effect”. In: *Reviews of Modern Physics* 82.2 (2010). RMP, pp. 1539–1592. DOI: 10.1103/RevModPhys.82.1539.

[70] Di Xiao, Ming-Che Chang, and Qian Niu. “Berry phase effects on electronic properties”. In: *Reviews of Modern Physics* 82.3 (2010). RMP, pp. 1959–2007. DOI: 10.1103/RevModPhys.82.1959.

[71] Shuichi Murakami. “Intrinsic Spin Hall Effect”. In: *Advances in Solid State Physics*. Ed. by B. Kramer. Berlin, Heidelberg: Springer Berlin Heidelberg, 2006, pp. 197–209. ISBN: 978-3-540-32430-0. DOI: 10.1007/11423256_16.

[72] T. Jungwirth, Qian Niu, and A. H. MacDonald. “Anomalous Hall Effect in Ferromagnetic Semiconductors”. In: *Physical Review Letters* 88.20 (2002). PRL, p. 207208. DOI: 10.1103/PhysRevLett.88.207208.

[73] H. Kontani et al. “Giant Orbital Hall Effect in Transition Metals: Origin of Large Spin and Anomalous Hall Effects”. In: *Physical Review Letters* 102.1 (2009). PRL, p. 016601. DOI: 10.1103/PhysRevLett.102.016601.

[74] G. Y. Guo et al. “Intrinsic Spin Hall Effect in Platinum: First-Principles Calculations”. In: *Physical Review Letters* 100.9 (2008). PRL, p. 096401. DOI: 10.1103/PhysRevLett.100.096401.

[75] N.F. Mott et al. *The Theory of Atomic Collisions*. Clarendon Press, 1965. ISBN: 9780198512424.

[76] Noah Sherman. “Coulomb Scattering of Relativistic Electrons by Point Nuclei”. In: *Physical Review* 103.6 (1956). PR, pp. 1601–1607. DOI: 10.1103/PhysRev.103.1601.

[77] Martin Gradhand et al. “Extrinsic Spin Hall Effect from First Principles”. In: *Physical Review Letters* 104.18 (2010). PRL, p. 186403. DOI: 10.1103/PhysRevLett.104.186403.

[78] Oliver Gueckstock et al. “Terahertz Spin-to-Charge Conversion by Interfacial Skew Scattering in Metallic Bilayers”. In: *Advanced Materials* n/a.n/a (2021), p. 2006281. ISSN: 0935-9648. DOI: https://doi.org/10.1002/adma.202006281.

[79] Zhen Zhang and Jr. Yates John T. “Band Bending in Semiconductors: Chemical and Physical Consequences at Surfaces and Interfaces”. In: *Chemical Reviews* 112.10 (2012), pp. 5520–5551. ISSN: 0009-2665. DOI: 10.1021/cr3000626.

[80] Xiao-Guang He, De-Gang Zhao, and De-Sheng Jiang. “Formation of two-dimensional electron gas at AlGaN/GaN heterostructure and the derivation of its sheet density expression*”. In: *Chinese Physics B* 24.6 (2015), p. 067301. ISSN: 1674-1056. DOI: 10.1088/1674-1056/24/6/067301.

[81] V. M. Edelstein. “Spin polarization of conduction electrons induced by electric current in two-dimensional asymmetric electron systems”. In: *Solid State Communications* 73.3 (1990), pp. 233–235. ISSN: 0038-1098. DOI: https://doi.org/10.1016/0038-1098(90)90963-C.

[82] Jairo Sinova et al. “Spin Hall effects”. In: *Reviews of Modern Physics* 87.4 (2015). RMP, pp. 1213–1260. DOI: 10.1103/RevModPhys.87.1213.

[83] Emmanuel I. Rashba and Sheka. “Symmetry of Energy Bands in Crystals of Wurtzite Type II. Symmetry of Bands with Spin-Orbit Interaction Included”. In.

[84] Aurelien Manchon. “Chapter 2 - Rashba spin–orbit coupling in two-dimensional systems”. In: *Spintronic 2D Materials*. Ed. by Wenqing Liu and Yongbing Xu. Elsevier, 2020, pp. 25–64. ISBN: 978-0-08-102154-5. DOI: https://doi.org/10.1016/B978-0-08-102154-5.00002-3.

[85] Yoshihiko Kamo et al. "Highly efficient photoconductive antennas using optimum low-temperature-grown GaAs layers and Si substrates". In: *Japanese Journal of Applied Physics* 53.3 (2014), p. 032201. ISSN: 0021-4922 1347-4065. DOI: 10.7567/jjap.53.032201.

[86] R. Adam et al. "Fabrication and subpicosecond optical response of low-temperature-grown GaAs freestanding photoconductive devices". In: *Applied Physics Letters* 81.18 (2002), pp. 3485–3487. DOI: 10.1063/1.1518159.

[87] Orhan Yalcin. *Ferromagnetic Resonance Theory and Applications*. Rijeka, Croatia: InTech, 2013. ISBN: 978-953-51-1186-3. DOI: 10.5772/50583.

[88] Oguz Yildirim. "Effect of microstructure on the magnetic properties of transition metal implanted TiO2 films". Thesis. 2016.

[89] Petr Marcon and K. Ostanina. "Overview of Methods for Magnetic Susceptibility Measurement". In: *Progress in Electromagnetics Research Symposium* (2012).

[90] K.H.J. Buschow and F.R. de Boer. *Physics of Magnetism and Magnetic Materials*. Springer US, 2007. ISBN: 9780306484087.

[91] Robert, Stephens, and Irving H. Malitson. "Index of refraction of magnesium oxide". In: *Journal of research of the National Bureau of Standards* 49 (1952), p. 249.

[92] A. Amudhavalli, R. Rajeswarapalanichamy, and K. Iyakutti. "Half metallic ferromagnetism in Ni based half Heusler alloys". In: *Computational Materials Science* 148 (2018), pp. 87–103. ISSN: 0927-0256. DOI: https://doi.org/10.1016/j.commatsci.2018.02.026.

[93] Takahide Kubota et al. "Half-metallicity and Gilbert damping constant in $Co_2Fe_xMn_{1-x}Si$ Heusler alloys depending on the film composition". In: *Applied Physics Letters* 94.12 (2009), p. 122504. DOI: 10.1063/1.3105982.

[94] Ajaya K. Nayak et al. "Design of compensated ferrimagnetic Heusler alloys for giant tunable exchange bias". In: *Nature Materials* 14.7 (2015), pp. 679–684. ISSN: 1476-4660. DOI: 10.1038/nmat4248.

[95] Y. Oner et al. "Superconductivity in the Heusler alloy Pd2YbPb". In: *Journal of Alloys and Compounds* 429.1 (2007), pp. 64–71. ISSN: 0925-8388. DOI: https://doi.org/10.1016/j.jallcom.2006.04.027.

[96] B. Venkateswarlu et al. "Magnetic and anomalous electronic transport properties of the quaternary Heusler alloys $Co_2Ti_xFe1 - xGe$". In: *Journal of Magnetism and Magnetic Materials* 407 (2016), pp. 142–147. ISSN: 0304-8853. DOI: https://doi.org/10.1016/j.jmmm.2016.01.059.

[97] S. J. Ahmed, C. Boyer, and M. Niewczas. "Magnetic and structural properties of Co_2MnSi based Heusler compound". In: *Journal of Alloys and Compounds* 781 (2019), pp. 216–225. ISSN: 0925-8388. DOI: `https://doi.org/10.1016/j.jallcom.2018.12.018`.

[98] Wei Han, YoshiChika Otani, and Sadamichi Maekawa. "Quantum materials for spin and charge conversion". In: *npj Quantum Materials* 3.1 (2018), p. 27. ISSN: 2397-4648. DOI: `10.1038/s41535-018-0100-9`.

[99] Shoji Ishida et al. "Search for Half-Metallic Compounds in Co2MnZ (Z=IIIb, IVb, Vb Element)". In: *Journal of the Physical Society of Japan* 64.6 (1995), pp. 2152–2157. ISSN: 0031-9015. DOI: `10.1143/JPSJ.64.2152`.

[100] Ming Zhang et al. "Is Heusler compound Co2CrAl a half-metallic ferromagnet: Electronic band structure, and transport properties". In: *Journal of Magnetism and Magnetic Materials* (2004), pp. 130–135. DOI: `10.1016/j.jmmm.2003.10.017`.

[101] N. D. Telling et al. "Interfacial structure and half-metallic ferromagnetism in Co_2MnSi-based magnetic tunnel junctions". In: *Physical Review B* 74.22 (2006). PRB, p. 224439. DOI: `10.1103/PhysRevB.74.224439`.

[102] I. Galanakis, P. H. Dederichs, and N. Papanikolaou. "Slater-Pauling behavior and origin of the half-metallicity of the full-Heusler alloys". In: *Physical Review B* 66.17 (2002). PRB, p. 174429. DOI: `10.1103/PhysRevB.66.174429`.

[103] Tanja Graf, Claudia Felser, and Stuart S. P. Parkin. "Simple rules for the understanding of Heusler compounds". In: *Progress in Solid State Chemistry* 39.1 (2011), pp. 1–50. ISSN: 0079-6786. DOI: `https://doi.org/10.1016/j.progsolidstchem.2011.02.001`.

[104] Braj Bhusan Singh et al. "High spin mixing conductance and spin interface transparency at the interface of a Co2Fe0.4Mn0.6Si Heusler alloy and Pt". In: *NPG Asia Materials* 13.1 (2021), p. 9. ISSN: 1884-4057. DOI: `10.1038/s41427-020-00268-7`.

[105] P. J. Hasnip, J. H. Smith, and V. K. Lazarov. "Ab initio studies of disorder in the full Heusler alloy Co2FexMn1-xSi". In: *Journal of Applied Physics* 113.17 (2013), 17B106. DOI: `10.1063/1.4801745`.

[106] Luis Flacke et al. "High spin-wave propagation length consistent with low damping in a metallic ferromagnet". In: *Applied Physics Letters* 115.12 (2019), p. 122402. DOI: `10.1063/1.5102132`.

[107] Takahide Kubota et al. “Current perpendicular-to-plane giant magnetoresistance using an $L1_2$ Ag_3Mg spacer and $Co_2Fe_{0.4}Mn_{0.6}Si$ Heusler alloy electrodes: Spacer thickness and annealing temperature dependence”. In: *Physical Review Materials* 1.4 (2017). PRMATERIALS, p. 044402. DOI: 10.1103/PhysRevMaterials.1.044402.

[108] T. Tanaka et al. “Intrinsic spin Hall effect and orbital Hall effect in 4d and 5d transition metals”. In: *Physical Review B* 77.16 (2008). PRB, p. 165117. DOI: 10.1103/PhysRevB.77.165117.

[109] H. Wang et al. “Scaling of Spin Hall Angle in 3d, 4d, and 5d Metals from Y3Fe5O12/Metal Spin Pumping”. In: *Physical Review Letters* 112 (2014), p. 197201. DOI: 10.1103/PhysRevLett.112.197201.

[110] Sangita S. Kalarickal et al. “Ferromagnetic resonance linewidth in metallic thin films: Comparison of measurement methods”. In: *Journal of Applied Physics* 99.9 (2006), p. 093909. DOI: 10.1063/1.2197087.

[111] Santanu Pan et al. “Ultrafast demagnetization mechanism in half-metallic Heusler alloy thin films controlled by the Fermi level”. In: *Physical Review B* 101.22 (2020). PRB, p. 224412. DOI: 10.1103/PhysRevB.101.224412.

[112] S. O. Valenzuela and M. Tinkham. “Direct electronic measurement of the spin Hall effect”. In: *Nature* 442.7099 (2006), pp. 176–179. ISSN: 1476-4687. DOI: 10.1038/nature04937.

[113] Chunhui Du et al. “Systematic variation of spin-orbit coupling with d-orbital filling: Large inverse spin Hall effect in 3d transition metals”. In: *Physical Review B* 90.14 (2014). PRB, p. 140407. DOI: 10.1103/PhysRevB.90.140407.

[114] Sang-Il Kim et al. “Dependence of inverse-spin Hall effect and spin-rectified voltage on tantalum thickness in Ta/CoFeB bilayer structure”. In: *Applied Physics Letters* 106.3 (2015), p. 032409. DOI: 10.1063/1.4906487.

[115] Jun Liu et al. “Correlation between the spin Hall angle and the structural phases of early 5d transition metals”. In: *Applied Physics Letters* 107.23 (2015), p. 232408. DOI: 10.1063/1.4937452.

[116] T. S. Seifert et al. “Terahertz spectroscopy for all-optical spintronic characterization of the spin-Hall-effect metals Pt, W and Cu80Ir20”. In: *Journal of Physics D: Applied Physics* 51.36 (2018), p. 364003. ISSN: 0022-3727 1361-6463. DOI: 10.1088/1361-6463/aad536.

[117] Torsten Kachel. “The PM3 beamline at BESSY II”. In: *Journal of large-scale research facilities JLSRF* 2 (2016), A48. DOI: 10.17815/jlsrf-2-73.

[118] Torsten Kachel, Frank Eggenstein, and Rolf Follath. “A soft X-ray plane-grating monochromator optimized for elliptical dipole radiation from modern sources”. In: *Journal of Synchrotron Radiation* 22 (2015), pp. 1301–1305. DOI: 10.1107/S1600577515010826.

[119] Radu Abrudan et al. “ALICE—An advanced reflectometer for static and dynamic experiments in magnetism at synchrotron radiation facilities”. In: *Review of Scientific Instruments* 86 (2015), p. 063902. DOI: 10.1063/1.4921716.

[120] Radu Abrudan and Florin Radu. “ALICE: A diffractometer/reflectometer for soft X-ray resonant magnetic scattering at BESSY II”. In: *Journal of large-scale research facilities JLSRF* 2 (2016), A69. DOI: 10.17815/jlsrf-2-83.

[121] Shingo Kaneta-Takada et al. “Enhancement of the Spin Hall Angle by Interdiffusion of Atoms in CoFeAl0.5Si0.5/n-Ge Heterostructures”. In: *Physical Review Applied* 14.2 (2020). PRAPPLIED, p. 024096. DOI: 10.1103/PhysRevApplied.14.024096.

[122] Haijun Zhang et al. “Topological insulators in Bi2Se3, Bi2Te3 and Sb2Te3 with a single Dirac cone on the surface”. In: *Nature Physics* 5.6 (2009), pp. 438–442. ISSN: 1745-2481. DOI: 10.1038/nphys1270.

[123] Yi Zhang et al. “Crossover of the three-dimensional topological insulator Bi2Se3 to the two-dimensional limit”. In: *Nature Physics* 6.8 (2010), pp. 584–588. ISSN: 1745-2481. DOI: 10.1038/nphys1689.

[124] C. L. Kane. “Chapter 1 - Topological Band Theory and the $_2$ Invariant”. In: *Contemporary Concepts of Condensed Matter Science*. Ed. by Marcel Franz and Laurens Molenkamp. Vol. 6. Elsevier, 2013, pp. 3–34. ISBN: 1572-0934. DOI: https://doi.org/10.1016/B978-0-444-63314-9.00001-9.

[125] D. J. Thouless et al. “Quantized Hall Conductance in a Two-Dimensional Periodic Potential”. In: *Physical Review Letters* 49.6 (1982). PRL, pp. 405–408. DOI: 10.1103/PhysRevLett.49.405.

[126] M. Z. Hasan and C. L. Kane. “Colloquium: Topological insulators”. In: *Reviews of Modern Physics* 82.4 (2010). RMP, pp. 3045–3067. DOI: 10.1103/RevModPhys.82.3045.

[127] Walter Kohn. “Theory of the Insulating State”. In: *Physical Review* 133.1A (1964). PR, A171–A181. DOI: 10.1103/PhysRev.133.A171.

[128] Charles L. Kane and Eugene J. Mele. “A New Spin on the Insulating State”. In: *Science* 314.5806 (2006), pp. 1692–1693. DOI: doi:10.1126/science.1136573.

[129] K. v Klitzing, G. Dorda, and M. Pepper. “New Method for High-Accuracy Determination of the Fine-Structure Constant Based on Quantized Hall Resistance”. In: *Physical Review Letters* 45.6 (1980). PRL, pp. 494–497. DOI: 10.1103/PhysRevLett.45.494.

[130] R. B. Laughlin. "Quantized Hall conductivity in two dimensions". In: *Physical Review B* 23.10 (1981). PRB, pp. 5632–5633. DOI: 10.1103/PhysRevB.23.5632.

[131] Kang L. Wang, Murong Lang, and Xufeng Kou. "Spintronics of Topological Insulators". In: *Handbook of Spintronics*. Ed. by Yongbing Xu, David D. Awschalom, and Junsaku Nitta. Dordrecht: Springer Netherlands, 2016, pp. 431–462. ISBN: 978-94-007-6892-5. DOI: 10.1007/978-94-007-6892-5_56.

[132] H. Ibach H.; Lüth. *Festkörperphysik. Eine Einführung in die Grundlagen. Zweite, überarb. u. erw. Auflage. Berlin etc., Springer-Verlag 1988. XII, 344 S., 230 Abb., 16 Tabellen, DM 59,—. ISBN 3-540-19087-2 (Springer-Lehrbuch)*. Vol. 70. Zeitschrift Angewandte Mathematik und Mechanik. 1990. ISBN: 0044-2267. DOI: 10.1002/zamm.19900700319.

[133] Xiao-Liang Qi and Shou-Cheng Zhang. "Topological insulators and superconductors". In: *Reviews of Modern Physics* 83.4 (2011). RMP, pp. 1057–1110. DOI: 10.1103/RevModPhys.83.1057.

[134] C. L. Kane and E. J. Mele. "Quantum Spin Hall Effect in Graphene". In: *Physical Review Letters* 95.22 (2005). PRL, p. 226801. DOI: 10.1103/PhysRevLett.95.226801.

[135] B. Andrei Bernevig, Taylor L. Hughes, and Shou-Cheng Zhang. "Quantum Spin Hall Effect and Topological Phase Transition in HgTe Quantum Wells". In: *Science* 314.5806 (2006), pp. 1757–1761. DOI: doi:10.1126/science.1133734.

[136] Markus König et al. "Quantum Spin Hall Insulator State in HgTe Quantum Wells". In: *Science* 318.5851 (2007), pp. 766–770. DOI: doi:10.1126/science.1148047.

[137] C. H. Li et al. "Electrical Detection of the Helical Spin Texture in a p-type Topological Insulator Sb2Te3". In: *Scientific Reports* 6.1 (2016), p. 29533. ISSN: 2045-2322. DOI: 10.1038/srep29533.

[138] Liang Fu and C. L. Kane. "Topological insulators with inversion symmetry". In: *Physical Review B* 76.4 (2007). PRB, p. 045302. DOI: 10.1103/PhysRevB.76.045302.

[139] J. E. Moore and L. Balents. "Topological invariants of time-reversal-invariant band structures". In: *Physical Review B* 75.12 (2007). PRB, p. 121306. DOI: 10.1103/PhysRevB.75.121306.

[140] Rahul Roy. "Z_2 classification of quantum spin Hall systems: An approach using time-reversal invariance". In: *Physical Review B* 79.19 (2009). PRB, p. 195321. DOI: 10.1103/PhysRevB.79.195321.

[141] D. Hsieh et al. "A topological Dirac insulator in a quantum spin Hall phase". In: *Nature* 452.7190 (2008), pp. 970–974. ISSN: 1476-4687. DOI: 10.1038/nature06843.

[142] Yiman Xia et al. "Electrons on the surface of Bi2Se3 form a topologically-ordered two dimensional gas with a non-trivial Berry's phase". In: (2008).

[143] Y. Xia et al. "Observation of a large-gap topological-insulator class with a single Dirac cone on the surface". In: *Nature Physics* 5.6 (2009), pp. 398–402. ISSN: 1745-2481. DOI: 10.1038/nphys1274.

[144] Chao-Xing Liu et al. "Model Hamiltonian for topological insulators". In: *Physical Review B* 82.4 (2010). PRB, p. 045122. DOI: 10.1103/PhysRevB.82.045122.

[145] Fakun K. Wang, Sijie J. Yang, and Tianyou Y. Zhai. "2D Bi2Se3 materials for optoelectronics". In: *iScience* 24.11 (2021), p. 103291. ISSN: 2589-0042. DOI: https://doi.org/10.1016/j.isci.2021.103291.

[146] A. R. Mellnik et al. "Spin-transfer torque generated by a topological insulator". In: *Nature* 511.7510 (2014), pp. 449–451. ISSN: 1476-4687. DOI: 10.1038/nature13534.

[147] Xinbo Wang et al. "Ultrafast Spin-to-Charge Conversion at the Surface of Topological Insulator Thin Films". In: *Advanced Materials* 30.52 (2018), p. 1802356. ISSN: 0935-9648. DOI: https://doi.org/10.1002/adma.201802356.

[148] Hanbum Park et al. "Enhanced Spin-to-Charge Conversion Efficiency in Ultrathin Bi2Se3 Observed by Spintronic Terahertz Spectroscopy". In: *ACS Applied Materials and Interfaces* 13.19 (2021), pp. 23153–23160. ISSN: 1944-8244. DOI: 10.1021/acsami.1c03168.

[149] Lukas Braun et al. "Ultrafast photocurrents at the surface of the three-dimensional topological insulator Bi2Se3". In: *Nature Communications* 7.1 (2016), p. 13259. ISSN: 2041-1723. DOI: 10.1038/ncomms13259.

[150] Sun Young Hamh et al. "Anisotropic Terahertz Emission from Bi2Se3 Thin Films with Inclined Crystal Planes". In: *Nanoscale research letters* 10.1 (2015), pp. 489–489. ISSN: 1931-7573 1556-276X. DOI: 10.1186/s11671-015-1190-y.

[151] S. Y. Hamh et al. "Surface and interface states of Bi2Se3 thin films investigated by optical second-harmonic generation and terahertz emission". In: *Applied Physics Letters* 108.5 (2016), p. 051609. DOI: 10.1063/1.4941420.

[152] Li-Guo Zhu et al. "Effect of Surface States on Terahertz Emission from the Bi2Se3 Surface". In: *Scientific Reports* 5.1 (2015), p. 10308. ISSN: 2045-2322. DOI: 10.1038/srep10308.

[153] Matteo Salvato et al. "Stoichiometric Bi2Se3 topological insulator ultra-thin films obtained through a new fabrication process for optoelectronic applications". In: *Nanoscale* 12.23 (2020), pp. 12405–12415. ISSN: 2040-3364. DOI: 10.1039/D0NR02725A.

[154] Yuri D. Glinka et al. "Ultrafast carrier dynamics in thin-films of the topological insulator Bi2Se3". In: *Applied Physics Letters* 103.15 (2013), p. 151903. DOI: 10.1063/1.4824821.

[155] J. A. Sobota et al. "Ultrafast Optical Excitation of a Persistent Surface-State Population in the Topological Insulator Bi_2Se_3". In: *Physical Review Letters* 108.11 (2012). PRL, p. 117403. DOI: 10.1103/PhysRevLett.108.117403.

[156] Avery J. Green et al. "Surface oxidation of the topological insulator Bi2Se3". In: *Journal of Vacuum Science & Technology A* 34.6 (2016), p. 061403. DOI: 10.1116/1.4964637.

[157] Desheng Kong et al. "Rapid Surface Oxidation as a Source of Surface Degradation Factor for Bi2Se3". In: *ACS Nano* 5.6 (2011), pp. 4698–4703. ISSN: 1936-0851. DOI: 10.1021/nn200556h.

[158] Murong Lang et al. "Revelation of Topological Surface States in Bi2Se3 Thin Films by In Situ Al Passivation". In: *ACS Nano* 6.1 (2012), pp. 295–302. ISSN: 1936-0851. DOI: 10.1021/nn204239d.

[159] Jiaxin Zhang et al. "Fabrication of Graphene/Bi2Se3/Graphene heterostructure without the surface oxidation of Bi2Se3". In.

[160] Bushra Irfan and Ratnamala Chatterjee. "Characterization and synthesis of Bi 2 Se 3 topological insulator thin film using thermal evaporation". In: *Advanced Materials Letters* 2016 (2016), pp. 100–150. DOI: 10.5185/amlett.2016.6208.

[161] Chaoyu Chen et al. "Robustness of topological order and formation of quantum well states in topological insulators exposed to ambient environment". In: *Proceedings of the National Academy of Sciences of the United States of America* 109.10 (2012), pp. 3694–3698. ISSN: 1091-6490 0027-8424. DOI: 10.1073/pnas.1115555109.

[162] Jiali Yang et al. "Robust Topological States in Bi2Se3 against Surface Oxidation". In: *The Journal of Physical Chemistry C* 124.11 (2020), pp. 6253–6259. ISSN: 1932-7447. DOI: 10.1021/acs.jpcc.0c00458.

[163] Hadj M. Benia et al. "Reactive Chemical Doping of the Bi_2Se_3 Topological Insulator". In: *Physical Review Letters* 107.17 (2011). PRL, p. 177602. DOI: 10.1103/PhysRevLett.107.177602.

[164] Jacob Pettine et al. "Ultrafast terahertz emission from emerging symmetry-broken materials". In: *Light: Science & Applications* 12.1 (2023), p. 133. ISSN: 2047-7538. DOI: 10.1038/s41377-023-01163-w.

[165] P. D. C. King et al. "Large Tunable Rashba Spin Splitting of a Two-Dimensional Electron Gas in Bi_2Se_3". In: *Physical Review Letters* 107.9 (2011). PRL, p. 096802. DOI: 10.1103/PhysRevLett.107.096802.

[166] Marco Bianchi et al. "Coexistence of the topological state and a two-dimensional electron gas on the surface of Bi2Se3". In: *Nature Communications* 1.1 (2010), p. 128. ISSN: 2041-1723. DOI: 10.1038/ncomms1131.

[167] I. S. S. de Oliveira, W. L. Scopel, and R. H. Miwa. "An ab initio investigation of Bi2Se3 topological insulator deposited on amorphous SiO2". In: *Journal of Physics: Condensed Matter* 29.4 (2017), p. 045302. ISSN: 0953-8984. DOI: 10.1088/1361-648X/29/4/045302.

[168] Louis Veyrat et al. "Band Bending Inversion in Bi2Se3 Nanostructures". In: *Nano Letters* 15.11 (2015), pp. 7503–7507. ISSN: 1530-6984. DOI: 10.1021/acs.nanolett.5b03124.

[169] Jun Zhang et al. "Raman Spectroscopy of Few-Quintuple Layer Topological Insulator Bi2Se3 Nanoplatelets". In: *Nano Letters* 11.6 (2011), pp. 2407–2414. ISSN: 1530-6984. DOI: 10.1021/nl200773n.

[170] Wei Lu et al. "Ultrafast photothermoelectric effect in Dirac semimetallic Cd3As2 revealed by terahertz emission". In: *Nature Communications* 13.1 (2022), p. 1623. ISSN: 2041-1723. DOI: 10.1038/s41467-022-29168-w.

[171] Kouhei Takahashi et al. "Terahertz Radiation via Ultrafast Manipulation of Thermoelectric Conversion in Thermoelectric Thin Films". In: *Advanced Optical Materials* 2.5 (2014), pp. 428–434. ISSN: 2195-1071. DOI: https://doi.org/10.1002/adom.201400009.

[172] Gaurav Gupta et al. "Carrier transport in Bi2Se3 topological insulator slab". In: *Physica E: Low-dimensional Systems and Nanostructures* 74 (2015), pp. 10–19. ISSN: 1386-9477. DOI: https://doi.org/10.1016/j.physe.2015.06.003.

[173] Qingyun Zhang and Udo Schwingenschlögl. "Rashba effect and enriched spin-valley coupling in GaX/MX_2 (M = Mo, W; X = S, Se, Te) heterostructures". In: *Physical Review B* 97.15 (2018). PRB, p. 155415. DOI: 10.1103/PhysRevB.97.155415.

[174] A. M. Adam et al. "Thermoelectric properties of Te doped bulk Bi2Se3 system". In: *Materials Research Express* 5.3 (2018), p. 035514. ISSN: 2053-1591. DOI: 10.1088/2053-1591/aab5e8.

[175] Donguk Kim, Chanuk Yang, and Yun Daniel Park. "Towards More Accurate Determination of the Thermoelectric Properties of Bi2Se3 Epifilms by Suspension via Nanomachining Techniques". In: *Sensors* 22.20 (2022), p. 8042. ISSN: 1424-8220.

[176] Christoph Kastl et al. “Ultrafast helicity control of surface currents in topological insulators with near-unity fidelity”. In: *Nature Communications* 6.1 (2015), p. 6617. ISSN: 2041-1723. DOI: 10.1038/ncomms7617.

[177] J. W. McIver et al. “Control over topological insulator photocurrents with light polarization”. In: *Nature Nanotechnology* 7.2 (2012), pp. 96–100. ISSN: 1748-3395. DOI: 10.1038/nnano.2011.214.

[178] Marco Bianchi et al. “Simultaneous Quantization of Bulk Conduction and Valence States through Adsorption of Nonmagnetic Impurities on Bi_2Se_3”. In: *Physical Review Letters* 107.8 (2011). PRL, p. 086802. DOI: 10.1103/PhysRevLett.107.086802.

[179] T. Valla et al. “Photoemission Spectroscopy of Magnetic and Nonmagnetic Impurities on the Surface of the Bi_2Se_3 Topological Insulator”. In: *Physical Review Letters* 108.11 (2012). PRL, p. 117601. DOI: 10.1103/PhysRevLett.108.117601.

[180] L. G. Parratt. “Surface Studies of Solids by Total Reflection of X-Rays”. In: *Physical Review* 95.2 (1954). PR, pp. 359–369. DOI: 10.1103/PhysRev.95.359.

[181] S. K. Sinha et al. “X-ray and neutron scattering from rough surfaces”. In: *Physical Review B* 38.4 (1988). PRB, pp. 2297–2311. DOI: 10.1103/PhysRevB.38.2297.

[182] Max Born and Emil Wolf. *Principles of Optics: Electromagnetic Theory of Propagation, Interference and Diffraction of Light*. 7th ed. Cambridge: Cambridge University Press, 1999. DOI: DOI:10.1017/CBO9781139644181.

[183] Yi-Ping Lai et al. “Temperature-dependent carrier–phonon coupling in topological insulator Bi2Se3”. In: *Applied Physics Letters* 105 (2014), p. 232110. DOI: 10.1063/1.4904009.

[184] Lukas Alber Bonetti et al. “NTMpy: An open source package for solving coupled parabolic differential equations in the framework of the three-temperature model”. In: *Computer Physics Communications* 265 (2021), p. 107990. ISSN: 0010-4655. DOI: https://doi.org/10.1016/j.cpc.2021.107990.

Publications and conference contributions

Articles

A1 https://journals.aps.org/prresearch/abstract/10.1103/ PhysRevResearch.3.043025 "Generation of terahertz transients from $Co_2Fe_{0.4}Mn_{0.6}Si$-Heusler-alloy/normal-metal nanobilayers excited by femtosecond optical pulses"
S. Heidtfeld, R. Adam, T. Kubota, K. Takanashi, D. Cao, C. Schmitz-Antoniak, D.E. Bürgler, F. Wang, C. Greb, G. Chen, I. Komissarov, H. Hardtdegen, M. Mikulics, R. Sobolewski, S. Suga, and C.M. Schneider
Phys. Rev. Research, **3(4)**, 043025(2021)

A2 https://doi.org/10.1016/j.jmmm.2021.168791"Generation of terahertz transients from
$Co_2Fe_{0.4}Mn_{0.6}Si$ Heusler alloy/heavy-metal bilayers"
S. Heidtfeld, R. Adam, T. Kubota, K. Takanashi, D. Cao, C. Schmitz-Antoniak, D.E. Bürgler, F. Wang, C. Greb, G. Chen, I. Komissarov, H. Hardtdegen, M. Mikulics, R. Sobolewski, S. Suga, and C.M. Schneider
Journal of Magnetism and Magnetic Materials, **547(18)**, 168791(2022)

Conference contributions (related to this work)

Talk "Generation of Terahertz Transients from $Co_2Fe_{0.4}Mn_{0.6}Si$(CFMS) Heusler alloy/ Normal-Metal (NM) Bilayers"
S. Heidtfeld, R. Adam, T. Kubota, K. Takanashi, D. Cao, C. Schmitz-Antoniak, D.E. Bürgler, F. Wang, C. Greb, G. Chen, I. Komissarov, H. Hardtdegen, M. Mikulics, R. Sobolewski, S. Suga, and C.M. Schneider
Physics of Magnetism, Poznan, Poland (2021)

Talk "Generation of Terahertz Transients from $Co_2Fe_{0.4}Mn_{0.6}Si$(CFMS) Heusler alloy/ Normal-Metal (NM) Bilayers"
S. Heidtfeld, R. Adam, T. Kubota, K. Takanashi, D. Cao, C. Schmitz-Antoniak, D.E. Bürgler, F. Wang, C. Greb, G. Chen, I. Komissarov, H. Hardtdegen, M.

Mikulics, R. Sobolewski, S. Suga, and C.M. Schneider
IRMMW-THz 2021, Chengdu, China (2021)

Acknowledgments

The accomplishment of this project owes much to the assistance of numerous people. I wish to extend my gratitude to these individuals by acknowledging their contributions with the following words. First of all, I want to thank my supervisor **Prof. Dr. Claus M. Schneider** for the opportunity to join the PGI-Institute and pursuing this Ph.D. journey. I am thankful for your guidance and continous support through these years.

I want to thank **Prof. Dr. Markus Münzenberg** for accepting the role of the second referee in the disputation.

I truly enjoyed the work in the laser group of **Dr. Roman Adam** and want to express my gratitude for his support with his experience, all the fruitful discussions and helpful suggestions. Thank you for always having an open door and your encouraging words in difficult moments.

I want to thank **PD Dr. Daniel E. Bürgler** for helpful and educative discussions, that have helped me a lot.

The exchange with **Prof. Dr. Roman Sobolewski** and **Dr. Ivan Komissarov** and their group members about the results and THz spectroscopy was always interesting and openend up for new ideas. Thank you!

I want to thank **Dr. Ivan Komissarov**, **Dr. Kiryl A. Niherish**, **Prof. Dr. Shigemasa Suga**, **Dr. Koki Takanashi**, **Dr. Takahide Kubota** and **Thomas Jansen** for providing the investigated sample systems.

My gratitude also goes to **Hilde Hartdegen**, **Martin Mikulics** and **Carolin Schmitz-Antoniak** for providing me with additional Raman and XMCD measurements.

Setting up the optical experiments in the lab would not have been possible without the great technical support of **Thomas Jansen**, **Heinz Pfeiffer**, **Norbert Schnitzler** and **Arndt Bremen**.

I will never forget all the fun working in the laser lab with all the members of my group **Christian Greb**, **Fanzghou Wang**, **Dr. Derang Cao**, **Dr. Seung-gi Gang** and **Dr. Umut Parlak**. Thank you so much for sharing knowledge and experience with me, even though you drove me crazy sometimes by stealing optics or screwdrivers.

Christian Greb and **Dr. Bharti Parashar**, we have spent all the good and bad times together at PGI-6 and you have become true friends. Your positive vibes always motivated me to keep going.

I want to thank also all the other members of PGI-6 that I have met during this time. I am grateful for the friendly atmosphere and interesting coffee-round discussions.
Last but not least I want to thank my friends and family. I want to thank my mother **Christine Heidtfeld** and my sister **Nadine Heidtfeld** for alway believing in me and supporting me through these years.
A special thank you also to my partner, **Philipp Soßong**. I am grateful for all your love and holding up my house of cards.

Curriculum vitae

Personal Information

Name	Sarah Heidtfeld
Date of birth	14.09.1989
Place of birth	Hagen, Germany
Nationality	german

Experience

since 07/2022	**Photonics Engineer** at VitreaLab GmbH, Vienna, Austria
09/2017 - 05/2021	**Doctoral Researcher**, PGI-6, Forschungszentrum Jülich, Germany
2015 - 2016	**Research Assistant**, Technische Universität Dortmund, Germany
2013 - 2014	**Student Assistant**, Technische Universität Dortmund, Germany

Education

09/2017 - 2025	**Ph.D. project**, PGI-6, Forschungszentrum Jülich, Germany Thesis title: *Investigation of spin current generated THz transients in materials with high spin-orbit coupling*
09/2013 - 05/2021	**Master of Science**, Physics, Technische Universität Dortmund, Germany Thesis Title: *Ultraschnelle Spindynamik in Indiumphosphid*
10/2010 - 09/2013	**Bachelor of Science**, Physics, Technische Universität Dortmund, Germany Thesis Title: *Ordnungs-Unordnungs-Phasenübergang in dotierten Tetrahydrofuran Clathrathydraten*

Band / Volume 289
Biodegradation and microbial upcycling of plastics
J. de Witt (2025), XVI, 259 pp
ISBN: 978-3-95806-804-9

Band / Volume 290
Practical Methods for Efficient Analytical Control in Superconducting Qubits
B. Li (2025), 202 pp
ISBN: 978-3-95806-807-0

Band / Volume 291
Ab initio investigation of topological magnetism in two-dimensional van der Waals heterostructures
N. Abuawwad (2025), xviii, 135 pp
ISBN: 978-3-95806-808-7

Band / Volume 292
Tolerance engineering of Pseudomonas for the efficient conversion and production of aldehydes
T. Lechtenberg (2025), XVI, 185 pp
ISBN: 978-3-95806-817-9

Band / Volume 293
Exploring the process window for production of itaconic, 2-hydroxyparaconic, and itatartaric acid with engineered *Ustilago* strains
P. Ernst (2025), x, 145 pp
ISBN: 978-3-95806-825-4

Band / Volume 294
Surface Plasmon Resonance Microscopy for the Characterization of Cell-Substrate Distances
J. Bednar (2025), xxiii, 187 pp
ISBN: 978-3-95806-830-8

Band / Volume 295
Microfluidic-MEA hybrid systems for electrophysiological recordings of neuronal co-cultures
J. Stevanović (2025), ix, 186 pp
ISBN: 978-3-95806-831-5

Band / Volume 296
Structural and Magnetic Properties of Biocompatible Iron Oxide Nanoparticles for Medical Applications
A. Nasser (2025), xii, 140 pp
ISBN: 978-3-95806-837-7

Band / Volume 297
Metabolic engineering of *Pseudomonas taiwanensis* for the improved production of styrene
J. Rönitz (2025), XII, 147 pp
ISBN: 978-3-95806-841-4

Band / Volume 298
Elucidation of anti-viral strategies in *Streptomyces*
B. U. Rackow (2025), xii, 148 pp
ISBN: 978-3-95806-842-1

Band / Volume 299
Ab initio investigations of spin-orbit functionalized graphene
D. Mazhjoo (2025), 163 pp
ISBN: 978-3-95806-847-6

Band / Volume 300
3D neural implants for* in vivo *applications
M. Jung (2025), xvi, 215 pp
ISBN: 978-3-95806-852-0

Band / Volume 301
Phonons in Magnetic Systems by means of Density- Functional Perturbation Theory
A. Neukirchen (2025), xviii, 195 pp
ISBN: 978-3-95806-853-7

Band / Volume 302
Optimal control and machine learning of quantum device dynamics
F. Preti (2025), iv, 211 pp
ISBN: 978-3-95806-856-8

Band / Volume 303
Development of a New, Miniaturized and Flexible Temperature Sensor
S. Hamacher (2025), XXII, 153 pp
ISBN: 978-3-95806-863-6

Band / Volume 304
Investigation of spin current generated THz transients in materials with high spin-orbit coupling
S. Heidtfeld (2026), viii, 112, v pp
ISBN: 978-3-95806-893-3

Weitere ***Schriften des Verlags im Forschungszentrum Jülich*** unter
http://wwwzb1.fz-juelich.de/verlagextern1/index.asp

Schlüsseltechnologien / Key Technologies
Band / Volume 304
ISBN 978-3-95806-893-3